Hydrothermal Synthesis of Nitrogen and Phosphorus co-doped Carbon Dots from Enset for an Interfacial Modification Layer of ZnO ETL in PTB7:$PC_{70}BM$ Bulk Heterojunction Polymer Solar Cell

Bisrat Nigusie Tafese

A Thesis Submitted to the Department of Materials Science and Engineering

School of Mechanical, Chemical, and Materials Engineering

Presented in Partial Fulfillment of the Requirement for the Degree of

Master of Science in Materials Science and Engineering

Office of Graduate Studies

Adama Science and Technology University

June 2022

Adama, Ethiopia

Hydrothermal Synthesis of Nitrogen and Phosphorus co-doped Carbon Dots from Enset for an Interfacial Modification Layer of ZnO ETL in PTB7:$PC_{70}BM$ Bulk Heterojunction Polymer Solar Cell

Bisrat Nigusie Tafese

Advisor: Fekadu Gochole (Ph.D.)

Co-advisor: Thothadri Ganesh (Ph.D.)

A Thesis Submitted to the Department of Materials Science and Engineering

School of Mechanical, Chemical, and Materials Engineering

Presented in Partial Fulfillment of the Requirement for the Degree of

Master of Science in Materials Science and Engineering

Office of Graduate Studies

Adama Science and Technology University

June 2022

Adama, Ethiopia

Declaration

I hereby declare that this Master Thesis entitled "**Hydrothermal Synthesis of Nitrogen and Phosphorus co-doped Carbon Dots from Enset for an Interfacial Modification Layer of ZnO ETL in PTB7:PC70BM Bulk Heterojunction Polymer Solar Cell**" is my original work. That is, it has not been submitted for the award of any academic degree, diploma or certificate in any other university. All sources of materials that are used for this thesis have been duly acknowledged through citation.

Name of student	Signature	Date

Approval Page of M.Sc. Thesis

I/we, the advisors of the thesis entitled the advisor(s) of this thesis, hereby certify that I/we have read the final draft of the thesis entitled "**Hydrothermal Synthesis of Nitrogen and Phosphorus co-doped Carbon Dots from Enset for an Interfacial Modification Layer of ZnO ETL in PTB7:PC70BM Bulk Heterojunction Polymer Solar Cell**" and developed by Bisrat Nigusie Tafese, hereby certify that the recommendation and suggestions made by the board of examiners are appropriately incorporated into the final version of the thesis.

Major Advisor	Signature	Date
Co-advisor	Signature	Date

We, the undersigned, members of the Board of Examiners of the thesis by Bisrat Nigusie Tafese, have read and evaluated the thesis entitled "**Hydrothermal Synthesis of Nitrogen and Phosphorus co-doped Carbon Dots from Enset for an Interfacial Modification Layer of ZnO ETL in PTB7:PC70BM Bulk Heterojunction Polymer Solar Cell**" and examined the candidate during open defense. This is, therefore, to certify that the thesis is accepted for partial fulfillment of the requirement of the degree of Master of Science in Materials Science and Engineering.

Chairperson	Signature	Date
Internal Examiner	Signature	Date
External Examiner	Signature	Date

Finally, approval and acceptance of the thesis is contingent upon submission of its final copy to the Office of Postgraduate Studies (OPGS) through the Department Graduate Council (DGC) and School Graduate Committee (SGC).

Department Head	Signature	Date
School Dean	Signature	Date
Office of Postgraduate Studies, Dean	Signature	Date

Acknowledgments

First and foremost, I thank the Lord God Almighty for giving me the strength and grace to complete this task. First and foremost, I'd like to thank my advisor, Dr. Fekadu Gochole, for his patience, guidance, and constructive criticism. His advice was invaluable throughout my thesis work. I'd like to thank my co-advisor, Dr. Thothadri Ganesh, for his valuable advice and insightful comments. I'd like to thank ASTU for this opportunity, as well as Dr. Gebisa Bekele and the Technical Staff of the Material Science and Engineering program, Mr. Demeke Tesfaye and Mr. Henok Mekonen, for their encouragement and support. I am eternally grateful to my parents for their love, prayers, support, guidance, and patience as they educated and prepared me for the future. I am grateful to Dr. Dinsefa Mensur, Dr. Newaymedihn Tegegn Aberra, Mr. Guta Amenu, Mr. Alemayehu Girma, and Mr. Wegene Lema, for their unending assistance. Last but not least, I'd like to thank my long-time classmates, relatives, and others who have helped me in some way.

Table of Contents

Acknowledgment……i
List of Tables iv
List of Figures v
List of Acronyms vii
Abstract viii
Chapter One 1
Introduction 1
1.1 Background 1
1.2 Statement of the problem 3
1.3 Objectives 4
1.3.1 General Objective 4
1.3.2 Specific Objectives 4
1.4 Significance of the Study 4
1.5 Scope of the Study 5
1.6 Operational Definitions 5
Chapter Two 6
Review of Related Literature 6
2.1 Overview of BHJ PSCs 6
2.2 Challenges, and Recent Achievements in BHJ PSC 10
2.2.1 Challenges in BHJ PSC 10
2.2.2 Recent Achievements in Device Performance and Stability 12
2.3 Interfacial Engineering 16
2.4 Carbon Dots (CDs) 23
2.4.1 Carbon Dots Synthesis Methods 23
2.4.2 Morphologies and Chemical Structures of CDs 24
2.4.3 Optical properties of CDs 25
2.4.4 Hetero-atom Doping and Its Effect on Opto-electronic Properties of CDs 27
2.4.3 Carbon Dots as Interfacial Modifier in PSCs 30

Chapter three 32
Methodology 32
3.1 Materials and Chemicals 32
3.2 Research Design 32
3.3 Experimental Procedure 33
3.3.1 Synthesis of N & P Co-doped CDs 33
3.3.2 ZnO ETL precursor solution preparation 34
3.3.3 MoO_3 HTL precursor solution preparation 35
3.3.4 Device Fabrication 35
3.3.5 Characterization 36
Chapter Four 37
Results and Discussions 37
4.1 Morphology, Composition, and Structure of the as-prepared CDs 37
4.1.1 XRD Analysis 37
4.1.2 FTIR Analysis 40
4.1.3 SEM Analysis of the CDs 43
4.2 Optical Properties of the CDs 44
4.2.1 UV-Vis absorption 45
4.2.2 Photoluminescence 47
4.2.3 Optical Transmission 52
4.3 Electrical and Electrochemical Properties of N & P-CDs 53
4.3.1 Cyclic Voltammetry Analysis 53
4.3.2 Flat band potential determination 55
4.3.3 Electrochemical Impedance Spectra (EIS)Analysis 56
4.4 Application of the CDs as Interface Modifier for ETL in i-PSC 58
5. Conclusions 62
6. Recommendations 63
Reference 64
Appendix A 75
Appendix B 76

List of Tables

Page

Table 2.1 Achievements in device performance and stability using material innovation, morphology control, and smart device architecture……..…14

Table 2.2 Summary of use of CDs as an interfacial modifier for ZnO ETL in OSCs……..31

Table 3.1 Research design: Variation of dopant precursor concentration ……..33

Table 4.1 Summary of the Crystallographic parameters of the as-prepared CDs obtained from XRD data ……..39

Table 4.2 Excitation wavelength and associated emission wavelength and stoke shift values for each CDs ……..51

Table 4.3 Summary of the Cyclic voltammetry results and the band gaps of the CDs ……...54

Table 4.4 EIS curve fitting parameters for ETL only devices with different ETL combinations…58

Table 4.5 Photovoltaic parameters of the ZnO, ZnO:as-prepared CDs based PTB7:$PC_{70}BM$ solar cell devices ……60

List of Figures

Page

Fig 1.1 Different energy sources for world energy consumption and trends in worldwide energy consumption from 1965 to 2035 ……..……...……...……..2

Fig 2.1 BHJ-PSCs schematic diagram ……..……..……..7

Fig 2.2 Device architecture of the **(a)** normal and **(b)** inverted BHJ PSCs. Band diagram for the **(c)** normal and **(d)** inverted BHJ PSCs based on PTB7:PC70BM ……..……..8

Fig 2.3 The four key processes converting solar energy into electrical energy using PSC upon illumination ….……..……..9

Fig 2.4 J-V characteristic curve schematic representation of PSC ……...…….....10

Fig 2.5 Factors to be considered for successful commercialization of PSCs …….....10

Fig 2.6 Schematic diagram of the factors limiting the stability of PSCs …..……..12

Fig 2.7 Schematic diagrams of some basic donor, acceptor, electron, and hole transporting layers ……..……....16

Fig 2.8 Materials used for interfacial modification in PSC **(a)** Thin layer of aluminum **(b)** Fullerene based self-assembled monolayer (C60-SAM) **(c)** Lithium Sulfonated Polystyrene **(d)** poly(ethyleneimine) (PEI) polymer nanolayer **(e)** Aminosilane as a Molecular Linker between the Electron-Transport Layer and Active Layer **(f)** $PC_{70}BM$ fullerene interlayer ….....22

Fig 3.1 Procedure for preparation of enset powder ……..……..…….33

Fig 3.2 Schematics for the synthesis of N & P co-doped CDs from enset powder ……..……....34

Fig 3.3 Schematic of steps involved in the fabrication of the PSC devices …….36

Fig 4.1 The XRD spectrum of enset powder, CDs without filtering, CDs after filtering, nitrogen-doped CDs, phosphorus-doped CDs, and nitrogen and phosphorus co-doped CDs …….……...……38

Fig 4.2 Fig 4.2 The FTIR spectra of **(a)** enset powder, **(b)** Undoped CDs, **(c)** nitrogen-doped CDs, **(d)** phosphorus-doped CDs, **(e)** nitrogen and phosphorus co-doped CDs, and **(f)** Proposed generalized structure of the as-prepared N- & P-CDs ….……..……..…….42

Fig 4.3 SEM Images of **(a)** undoped CDs, **(b)** nitrogen-doped CDs, **(c)** phosphorus-doped CDs, **(d)** nitrogen and phosphorus co-doped CDs, **(e)** Pristine ZnO, and **(f)** ZnO/N- & P-CDs bilayer ETL films. ……...……..44

Fig 4.4 UV-Vis Absorption spectra of **(a)** undoped CDs, **(b)** nitrogen-doped CDs, **(c)** phosphorus-doped CDs, **(d)** nitrogen and phosphorus co-doped CDs, along with their respective Tauc, and **(e)** UV-Vis Absorption spectra of the donor PTB7 without ETL and with different ETL combinations 46
Fig 4.5 Photoluminescence spectra of **(a)** Undoped CDs, **(b)** nitrogen-doped CDs, **(c)** phosphorus-doped CDs, **(d)** nitrogen and phosphorus co-doped CDs, **(e)** photograph of CDs solution in water under visible light **(left)**, and under 365 nm UV light **(right)**, and **(f)** The probable electron transitions of the CDs 50
Fig 4.6 PL spectra of PTB7 with different ETL combinations.....52
Fig 4.7 Transmission spectra of **(a)** the as-prepared CDs and **(b)** ZnO/CDs bilayer ETL 52
Fig 4.8 Cyclic voltammetry measurements of the CDs/ITO and bare ITO electrodes 54
Fig 4.9 Calculated bandgap of CDs from UV-Vis absorption data 55
Fig 4.10 Mott−Schottky plots of the as-prepared CDs under dark conditions with a three-electrode system in a 0.5 M NaCl solution (pH 6.5) 56
Fig 4.11 (a) Nyquist plot of the ZnO and ZnO: CDs bilayer ETL based devices (Inset: equivalent circuit model), and **(b)** Fitted curve using the equivalent circuit 57
Fig 4.12 (a) Device configuration of the inverted PSCs with the ZnO/N- & P-CDs bilayer ETL, and **(b)** the energy band diagram of the device **(c)** J-V characteristic curve of the fabricated devices with different ETLs 59
Fig 4.14 Performance reproducibility of devices with different interface modification layer.....61

List of Acronyms

A	Acceptor
AZO	Aluminum doped Zinc Oxide
BHJ	Bulk Hetero-Junction
CDs	Carbon Dots
D	Donor
EIS	Electrochemical impedance spectroscopy
ETL	Electron Transporting Layer
FF	Fill Factor
FREAS	Fused Ring Electron Acceptors
FT-IR	Fourier transform infrared
HOMO	Highest Occupied Molecular Orbital
HTL	Hole Transporting Layer
ITO	Indium Tin Oxide
J_{sc}	Short Circuit Current Density
LUMO	Lowest Unoccupied Molecular Orbital
NFAs	Non-fullerene Acceptors
$PC_{70}BM$	{6,6}-Phenyl-C70-butyric acid methyl ester
PCE	Power Conversion Efficiency
PL	Photoluminescence
PLQY	Photoluminescence Quantum Yield
PSC	Polymer Solar Cell
PTB7	Poly {{4,8-bis{(2-ethylhexyl)oxy}benzo{1,2-b:4,5-b'}dithiophene-2,6-diyl}{3-fluoro-2-{(2-ethylhexyl)carbonyl}thieno{3,4-b}thiophenediyl}}
PV	Photovoltaic
SEM	Scanning Electron Microscopy
V_{oc}	Open Circuit Voltage
UV-Vis	Ultraviolet-visible
WF	Work Function
XRD	X-ray Diffraction

Abstract

*The interface between the active layer and charge transporting layer is critical and plays an important role in performance improvement in polymer solar cells (PSCs). In this thesis, the focus is to improve the performance of inverted PTB7:$PC_{70}BM$-based polymer solar cells through interfacial modification between ZnO and the active layer. Zinc oxide (ZnO) is a common Electron Transport Layer (ETL) used in PSCs, but its use in highly efficient PSCs including those based on PTB7:$PC_{70}BM$, is limited due to numerous surface defects, mismatched energy bands with the photoactive layer, and incompatibility between the active layer and ZnO ETL. Herein, Nitrogen and Phosphorus co-doped Carbon Dots (N- & P- CDs) was synthesized from enset (Ensete ventricosum) as a main precursor, ethylenediamine as a nitrogen dopant precursor, and orthophosphoric acid as a phosphorus dopant precursor using hydrothermal synthesis method for interfacial modification in ETL for an inverted PTB7:$PC_{70}BM$ based PSC. The N & P-CDs films were characterized using XRD, FTIR, SEM, UV-Vis Absorption, PL, Transmittance, CV, and EIS. The synthesized N- & P- CDs show absorbance in UV range, and exhibited excitation wavelength-dependent photoluminescence, as well as down-shifting higher-energy UV light to lower-energy visible light, and emitted bright blue light when illuminated with a 365 nm lamp. The synthesized N- & P- CDs were employed as an interfacial modification layer for the ZnO ETL with device structure of Glass/ITO/ZnO/**N- & P- CDs**/$PC_{70}BM$:PTB7/MoO_3/Al, and show more than 31 % performance improvement compared to a device without interfacial modification layer. This is due to the improvement of charge extraction efficiency by smoothing ZnO surface defects and minimizing band mismatch between the active layer and ZnO using N- & P- CDs. The results indicate that the water-soluble N- & P- CDs developed in this study have the potential to be used in solution-processable large-area PSCs.*

Keyword: *interfacial modification, wavelength-dependent, inverted polymer solar cell, CDs, ETL*

Chapter One

Introduction

1.1 Background

Meeting the ever-increasing need for energy in every sector of life is one of the world's most pressing concerns in the twenty-first century (Hu et al., 2020). As seen in Fig. 1.1, conventional energy sources such as coal, oil, and natural gas still provide the majority of total energy produced worldwide, but they have significant drawbacks in terms of shortage and pollution. The combustion of fossil fuels releases CO_2, a greenhouse gas that contributes to global warming by diminishing the protective ozone layer, endangering humanity's very existence. Furthermore, the restricted availability of all of these energy sources forces scientists to look for non-conventional and renewable alternatives. (Demirbas, 2017; Manju & Sagar, 2017).

The energy crisis is particularly acute in Ethiopia, where only around half of the country's people have access to power for day-to-day operations such as food preparation and other duties. People in rural areas of the nation, where almost 80% of the population resides, rely on firewood (67% of energy supply), charcoal and animal dung (17%), and gas (14%), almost 98% non-renewable energy is used for food preparation and lighting, which shows that they lack a sustainable energy source (Getie, 2020). In a rural location where people live in a dispersed manner, access to renewable energy necessitates unique techniques to improve people's living conditions. Because the country is endowed with thirteen months (Ethiopian calendar) of sunshine and solar energy is one of the most abundant and clean energy sources, which is uniquely the greatest choice for granting access to power throughout the country as a whole, and in rural regions in particular.

Considering these issues, the use of environmentally clean and safe renewable energy sources has received great attention these days. As a result, the exponential increase in the cumulative installed capacity of renewable energy sources has been observed for at least the last two decades (Fig 1.1).

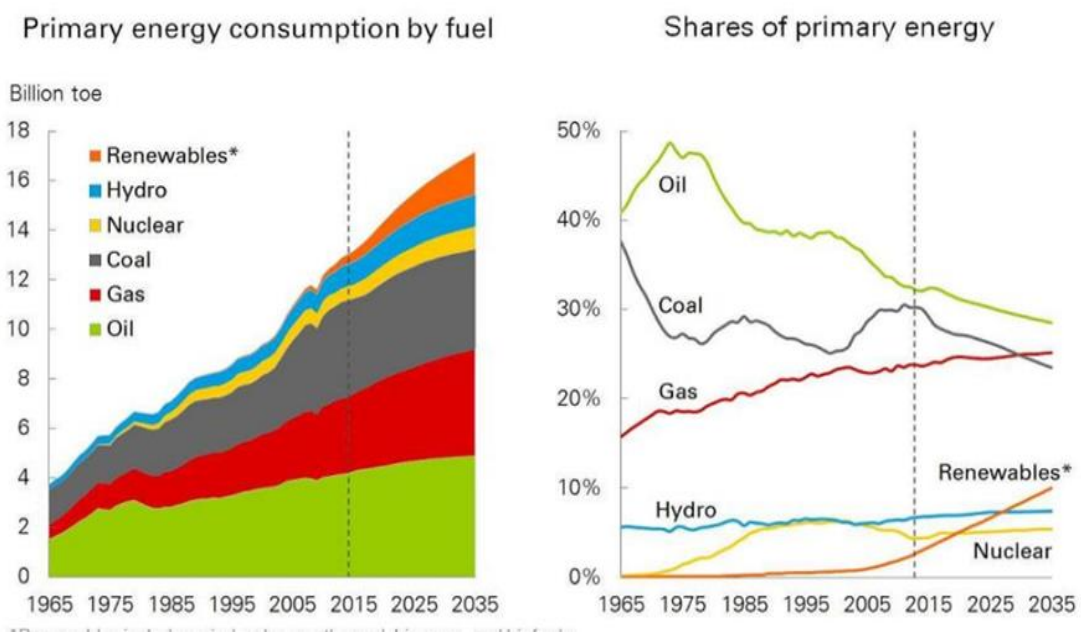

Fig 1.1 *Different energy sources for world energy consumption and trends in worldwide energy consumption from 1965 to 2035* (Arias et al., 2018)

Among several promising renewable energy sources such as geothermal, wind, solar, H_2 and biomass, etc., solar energy can be considered one of the most widely available and clean energy sources on earth. The abundant sun's energy, which is found in the form of light and heat can meet the energy demands of generations to come if captured and stored properly. Therefore, converting solar energy into electric energy using photovoltaic technology is a promising technique that can meet the growing requirement for sustainable energy. Among the PV technologies available, PSCs have received much attention in the scientific community due to their particular advantages of environmental friendliness, potentially low-cost materials and processes, lightweight, flexibility, and large-area manufacturing (Czolk et al., 2016; Hsieh et al., 2018; Li et al., 2019; Qiu et al., 2019; Song et al., 2018; Song et al., 2021; Sun et al., 2018; Traverse et al., 2017).

Due to the development of novel materials with improved photovoltaic properties (Lin et al., 2015; Yuan et al., 2019; Zhu et al., 2020), improved fabrication processes such as morphology control (Dai et al., 2020; Gurney et al., 2019; Nair & Kumar, 2016; Qiu et al., 2020), use of smart architectures (Ho et al., 2020; Lim et al., 2016; Rao et al., 2018), and interfacial engineering (Qin et al., 2020; Yin et al., 2017; Zafar et al., 2020; Zheng et al., 2019), PSCs based on conjugated polymers and fullerene composites have advanced rapidly in PCE in recent decades.

1.2 Statement of the problem

Interfacial engineering is a powerful tool to achieve high-performing PSCs devices. ZnO is one of the most extensively used interfacial materials as ETL in PSCs, owing to its promising electron extraction property, environmentally friendliness, easy processing steps required both for solution processing as well as sol-gel processing, and better optical transparency (Lin et al., 2016; R. Zhang et al., 2018).

However, surface defects formed in the interior and on the surface of the film during sol-gel processing, a mismatch between the conduction band energy level of ZnO and the LUMO level of acceptor materials in the active layer, and incompatibility between the organic materials (active layer) and the inorganic ZnO ETL all these limit its application for highly efficient PSCs (Lin et al., 2016; R. Zhang et al., 2018).

Many efforts have been made to facilitate efficient electron extraction and transport, as well as to modify the ZnO/BHJ interface to suppress trap-assisted recombination (Ling et al., 2019; Liu et al., 2016; Yiwen Wang et al., 2017; Wu et al., 2016; Xiang Xu et al., 2020). Different interfacial materials, such as self-assembled monolayers, water or alcohol-soluble polymers and polyelectrolytes, ionic liquids, and other several materials have been used to form a bilayer ETL in PSCs. However, these organic polymer modifiers have insulating properties and are not effectively utilizing the incoming incident light, consequently limiting the device's performance. Therefore, it is necessary to find new types of interface modifiers to replace conventional organic modifiers to achieve the desired device performance for i-PSCs.

Recently, interfacial modification layers based on CDs have attracted increasing research attention due to their fascinating properties, which include; wavelength-dependent luminescence emission (Gharat et al., 2019), good water-soluble processability (Fan et al., 2017), tunable optical and electronic properties (Abdelsalam et al., 2018; Ren et al., 2019; Yifan Wang et al., 2017), and photochemical stability (Datta et al., 2016), non-toxicity (Dong et al., 2014), environmental friendliness, low-cost and simple preparation using abundant precursors (Zhou et al., 2018), making them an ideal interface modification materials for highly efficient PSC devices.

However, there is minimal literature on the use of CDs as an interfacial modification layer in PSCs, and the CD synthesis precursors were chemicals, creating environmental and cost-related concerns for large-scale PSCs device fabrication. As a result, CDs made from ecologically benign, low-cost, and abundant bio sources will be critical. Moreover, there are no reports on the use of N & P co-doped CDs as an interfacial modification layer for PSCs. Therefore, the use of N & P co-doped CDs derived from bio sources, as an interfacial modification layer for ZnO ETL is proposed for the first time in this study, to the best of our knowledge.

1.3 Objectives

1.3.1 General Objective

The overall objective of this study is to synthesize N & P co-doped CDs using a hydrothermal method from locally available Enset (Ensete ventricosum) as the primary precursor, ethylenediamine as nitrogen source, and ortho-phosphoric acid as a phosphorus source, for interfacial modification layer of ZnO ETL in an i-PSC.

1.3.2 Specific Objectives

a) Synthesizing undoped CDs, N- doped CDs, P-doped CDs, and N & P co-doped CDs
b) Characterizing the above-synthesized CDs for structural, chemical functionalities, morphological, optical, and electrochemical properties using XRD, FT-IR, SEM, UV-Vis, PL, and EIS, respectively.
c) Preparing ZnO ETL and MoO_3 HTL solutions
d) Fabricating the inverted BHJ PSC with a device structure of Glass/ITO/ZnO/**N- & P-CDs**/ PTB7:$PC_{70}BM$/MoO_3/Al and ITO/ZnO/PTB7:$PC_{70}BM$/MoO_3/Al, and characterizing and analyzing the Current density versus Voltage (J–V) characteristics of the fabricated i-PSC devices

1.4 Significance of the Study

This research is extremely important in Ethiopia, where the country's energy crisis is particularly acute, with only about half of the population having access to power for day-to-day operations such as food preparation and other duties. Based on the facts, solar energy conversion research, particularly using environmentally viable, low-cost materials and simple fabrication techniques, is critical in Ethiopia.

People in the country's rural areas, where nearly 80% of the population lives, rely on firewood, charcoal, animal dung, and gas (Getie, 2020). Food preparation and lighting use roughly 98% nonrenewable energy, showing a lack of a long-term energy source. In a rural location where people are dispersed, access to renewable energy needs specialized strategies, such as the utilization of solar energy, to enhance people's living conditions. Solar energy is the best alternative for assuring power access throughout the country, particularly in rural locations, because Ethiopia has thirteen months of sunshine (according to the Ethiopian calendar) and is one of the most abundant and clean energy sources. Given the aforementioned problems, this research is crucial in laying the framework for supplying clean energy to our community through the use of ecologically benign, safe, and long-term solar energy.

1.5 Scope of the Study

The study is confined to the adjustment of ETL in i-PSC to meet the research objectives. The examination of N & P co-doped CDs as interfacial modification layer for ZnO ETL in i-PSC is restricted.

1.6 Operational Definitions

Carbon Dots (CDs): is a novel type of carbon nanomaterials made up of discrete, quasi-spherical carbon nanoparticles with diameters less than 10nm.

BHJ (Bulk Hetero-Junction): the active layer in polymer solar cell created by constructing interpenetrating networks of donor and acceptor materials

Power Conversion Efficiency (PCE): it is the ability of a solar cell to convert light into electricity, and is the ratio of incident light power to output electrical power

Short-circuit Current Density (J_{SC}): the maximum current that a photovoltaic cell can generate under short circuit conditions

Open-circuit voltage (V_{OC}): is the maximum voltage that a photovoltaic device can produce

Fill Factor (FF): is essentially a measure of the quality of the solar cell. It is calculated by comparing the maximum power to the theoretical power that would be output at both the open-circuit voltage and short circuit current together.

Chapter Two

Review of Related Literature

2.1 Overview of BHJ PSCs

Yu and co-workers created the Bulk Heterojunction (BHJ) structure in 1995 (Yu et al., 1995), which is the most frequently used and successful device structure in the PSC area, in which conjugated polymer and fullerene derivatives are mixed as the active layer. The BHJ forms two channels for transferring electrons and holes to the corresponding electrodes, as opposed to the planar architecture when the Acceptor (A) and Donor (D) materials were sequentially stacked on top of each other and could selectively touch the cathode and anode electrodes. Hence, the D and A domains are expected to form a bi-continuous network with nano-scale morphology for efficient charge transport and collection after exciton dissociation. Therefore, in the BHJ device architecture, a mixture of D and A molecules in the same or different solvents was used to form a bi-continual layer, which serves as the active layer of the device that absorbs light for exciton generation (Fig 2.1).

Due to the short diffusion length of excitons and the small donor-acceptor interface (bi-layer device), most of the generated excitons will recombine before reaching the D-A interface. Thus, getting a large number of charge carriers was the most difficult challenge in monolayer and bilayer architectures. The bi-continuous three-dimensional interpenetrating network of the BHJ design generates a greater D-A interface, which is necessary for effective exciton dissociation in the BHJ due to short exciton diffusion (Xia et al., 2019). When compared to the prior design, photo-generated excitons may dissociate into free holes and electrons more effectively, resulting in better charge separation for improved performance of the cell.

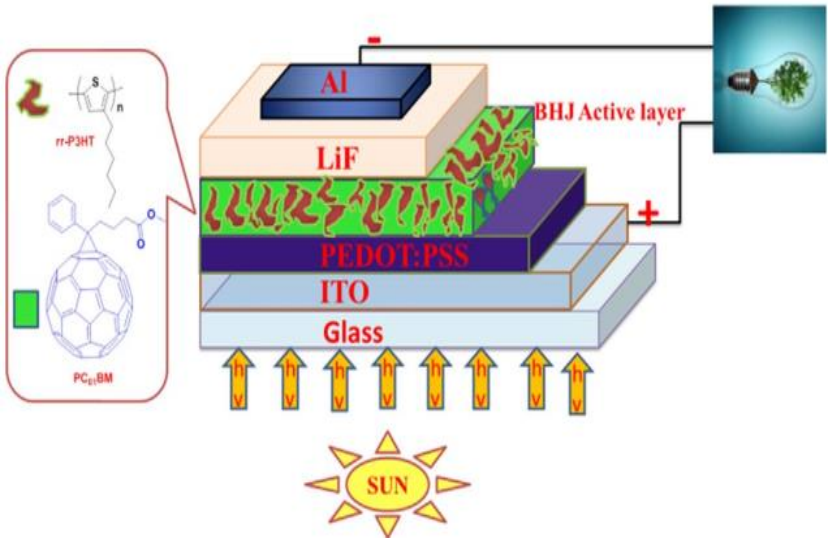

Fig 2.1 *BHJ-PSCs schematic diagram* (Ganesamoorthy et al., 2017).

The BHJ architecture has laid a great milestone in terms of achieving better efficiencies in PSC to realize their commercialization. However, the environmental stability of this PSC remains the biggest challenge to overcome, due to oxygen and moisture intrusion into the electrodes, and the damage caused in the air or oxidation of the electrodes. To overcome this challenge researchers had established inverted device architecture for BHJ PSCs. In an inverted device, the bottom transparent electrode serves as the cathode while the top electrode is an anode, as shown in Fig 2.2 **(b)**. The inverted devices exhibited higher environmental stability, and higher efficiencies in most cases in comparison with the normal architecture (Fig 2.2 **(a)**), of PSCs, which is achieved by using high work function metal or metal oxides as a cathode and the low work function metal as an anode. In the normal architecture the low work function cathode would easily get oxidized in the air by oxygen and moisture, thus using a higher work function cathode minimizes this tendency and improves efficiency and stability. Band diagrams for the normal and inverted devices are depicted in Fig 2.2 **(c)** and **(d)**, respectively.

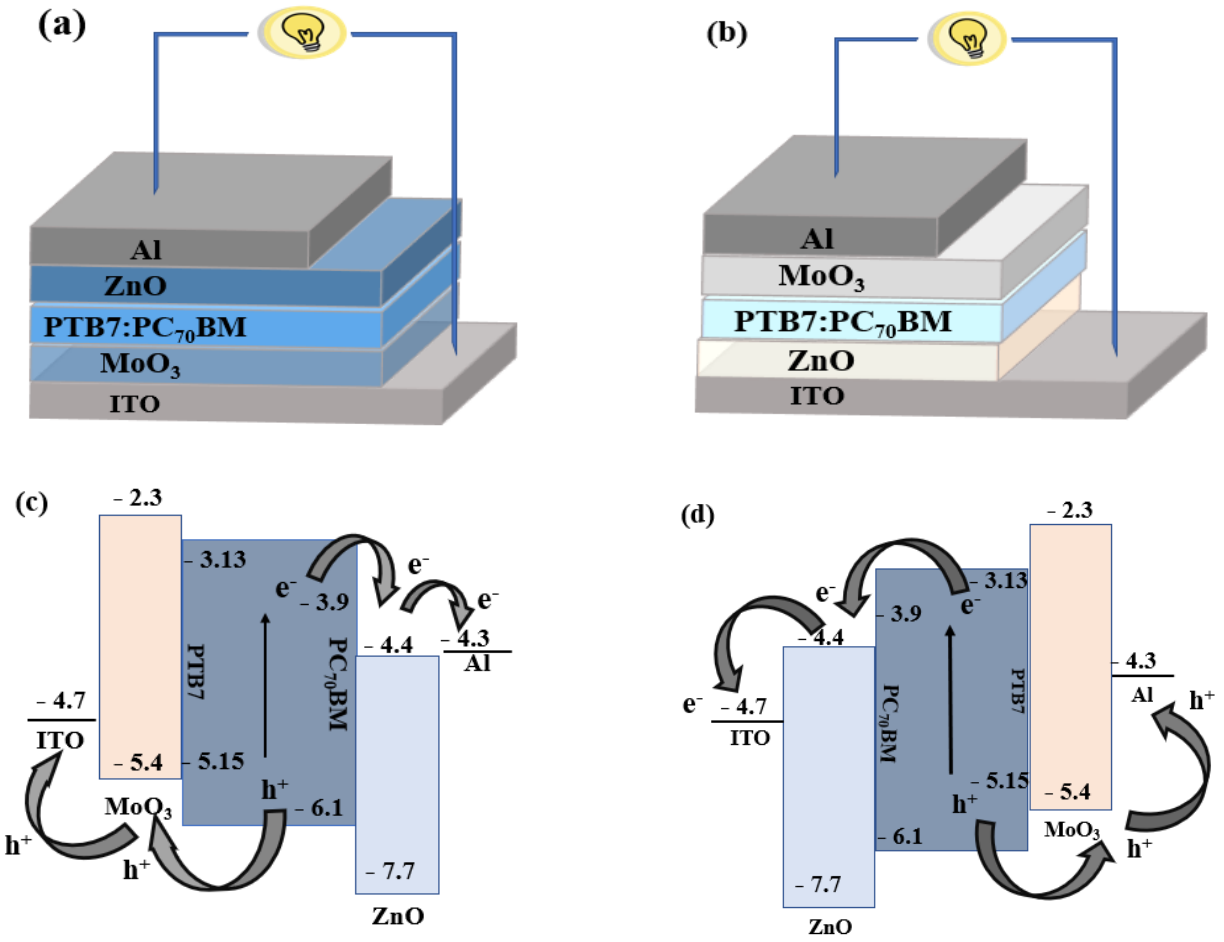

Fig 2.2 *Device architecture of the* ***(a)*** *normal and* ***(b)*** *inverted BHJ PSCs. Band diagram for the* ***(c)*** *normal and* ***(d)*** *inverted BHJ PSCs based on PTB7:$PC_{70}BM$.*

The working principle of the BHJ PSC device involves four fundamental steps namely **(i)** photons absorption and exciton creation, **(ii)** exciton diffusion and splitting at the D-A interface, **(iii)** charge transportation, and, **(iv)** charge collection (Ganesamoorthy et al., 2017). In a BHJ PSC device, the donor material is the one that absorbs the incoming light.

Due to a substantial potential energy drop, the excitons must diffuse to the D-A interface, where they will be split into free charge carriers such as electrons and holes (Y. Zhang et al., 2019). There can be some limitations and losses during the device operation steps discussed above, which include absorption loss due to spectral mismatch, thermalization loss, the energy required for exciton splitting might be inefficient, charge recombination loss, etc. (Siddiki et al., 2010). A schematic representation of the steps in energy production of a typical PSC is shown in Fig 2.3.

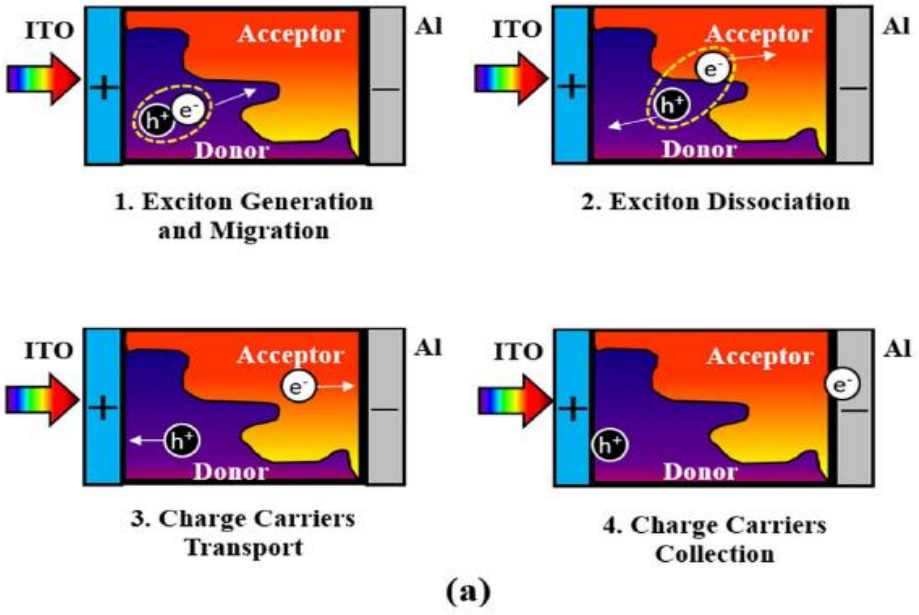

Fig 2.3 *The four key processes converting solar energy into electrical energy using PSC upon illumination* (Rafique et al., 2018).

The most important performance parameters for the BHJ PSCs are J_{SC}, V_{OC}, FF, and PCE.

FF is the ratio between power outputs ($V_{MPP}J_{MPP}$) at the maximum power point to the absolute power (V_{OC} J_{SC}).

$$FF = \frac{P_{max}}{V_{oc}J_{sc}} = \frac{V_{MPP}J_{MPP}}{V_{oc}J_{sc}} \qquad (1)$$

The estimated PCE is the ratio of P_{out} to the P_{in}, where P_{out} and P_{in} are the power output and power input of the incident light, respectively and the J-V curve schematic representation is given in Fig 2.4.

$$PCE = \frac{P_{out}}{P_{in}} = \frac{FF \times V_{oc} \times J_{sc}}{P_{in}} \qquad (2)$$

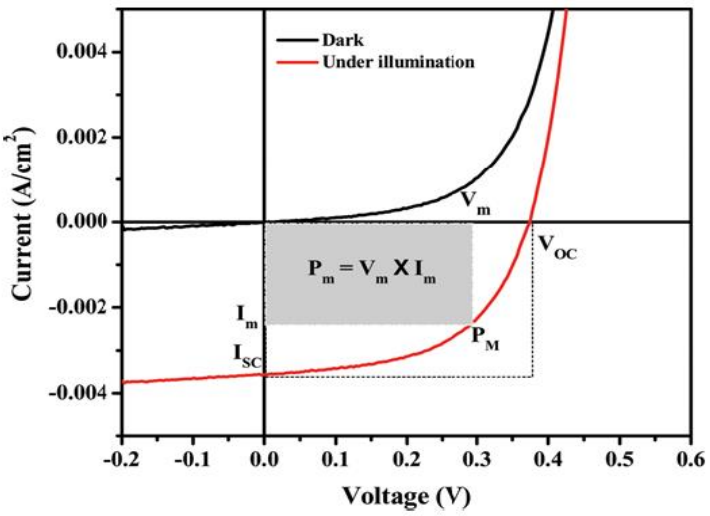

Fig 2.4 *J-V characteristic curve schematic representation of PSC* (Abdulrazzaq et al., 2013).

2.2 Challenges, and Recent Achievements in BHJ PSC

2.2.1 Challenges in BHJ PSC

The PSCs Devices are expected to possess the following characteristics for successful commercialization: high performance, environmentally friendly, simple fabrication process, high stability, and low cost as shown in Fig 2.5. However, efficiency and stability are the major challenges faced by PSC for its successful commercialization (Baran et al., 2017; Cheng & Zhan, 2016; Li et al., 2018).

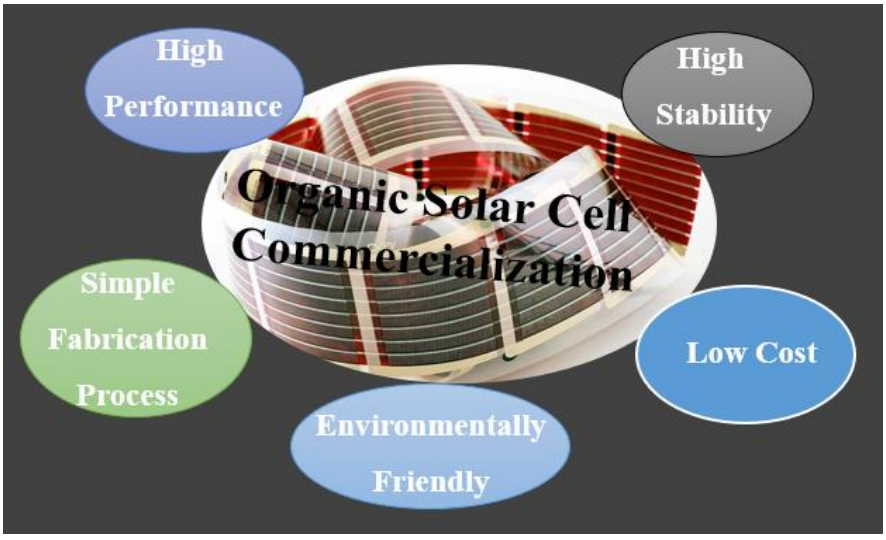

Fig 2.5 *Factors to be considered for successful commercialization of PSCs*

1. Lower Power Conversion Efficiencies

Shorter diffusion lengths of excitons in conjugated polymers are limited to a few nanometers (less than 20 nm), which is shorter than the optical absorption path length (~ 100–200 nm) (Yeboah & Singh, 2017), contributes to lower power conversion efficiencies in PSCs. Another factor that limits device efficiencies is lower charge carrier mobility in the conjugated polymers causing, their recombination before reaching their respective electrodes (A. Sharma et al., 2017). Consequently, the solar cell experiences a significant loss in photogenerated current, and hence poor device performance.

Poor charge carrier collection at the electrodes is also another factor that limits device performance. For efficient charge extraction at the respective electrodes, the WF of the anode should match with the HOMO of the donor, and the WF of the cathode should match with the LUMO of the acceptor (Sun et al., 2019). If there is a match between the WFs and the MO of the active layer, then the contacts are said to be Ohmic contacts. But, if there is a mismatch between the anode and cathode with that of donor HOMO or acceptor LUMO, respectively, then no Ohmic contacts would be established, which ultimately, results in poor performance of the solar cell. In most PSCs, there is a mismatch between the anode and cathode with that of donor HOMO and acceptor LUMO respectively, which poses a great challenge in charge carrier collection in the respective electrodes, and overall device performance.

2. Stability/Degradation Issues

The stability of PSC device is the most important factor that should be given great attention to realize their commercialization, though there have been limited literature on the stability of PSCs compared to the literature on the efficiency of PSCs. A study on the stability of PSCs helps in understanding how a device degrades during its operation (Rafique et al., 2018).

Device instability occurs due to a range of complex phenomena that are in play simultaneously (Cheng & Zhan, 2016). These degradation factors include mechanical stress, irradiation (time & intensity), water, oxygen, heating, etc. (Fig 2.6), and may affect the active layer, the transport layers, the contacts, and the interface of every layer with the adjacent layers.

In general, degradation factors in PSCs can be distinguished to be either **intrinsic,** in which degradation arises from the thermal diffusion of constituent materials at interfaces of PSCs (Ghasemi et al., 2021), or **extrinsic**, where degradation occurs under changing environmental conditions (light, dark, hot, cold, dry, and humid conditions), the factors include, oxygen and water, irradiation, mechanical stress, etc.

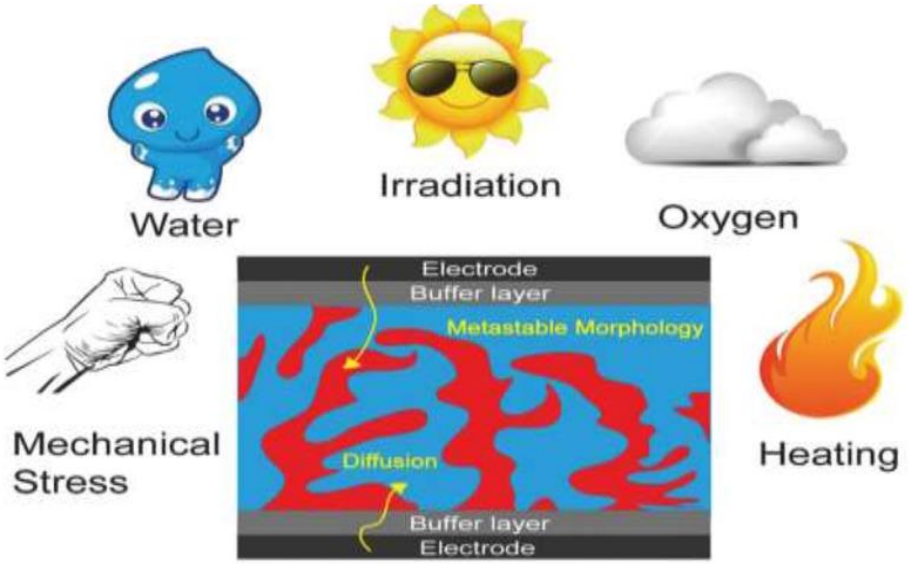

Fig 2.6 *Schematic diagram of the factors limiting the stability of PSCs* (Cheng & Zhan, 2016).

2.2.2 Recent Achievements in Device Performance and Stability

The invention of new donor and acceptor materials with improved PV properties, such as high charge-carrier mobility, complementary absorption bands in the Vis-NIR range, improved D-A interface property for exciton generation, dissociation, and transport, and small energy offset to minimize voltage losses, have been the primary strategy for fabricating PSC with better efficiency and improved device stability.

Among material innovations, Non-Fullerene Acceptors (NFAs) have achieved a great milestone in improving PSCs performance because they show particular advantages in reducing energy loss for a high V_{oc} and extending the absorption range for a high J_{sc}, which are essential requirements for high PCEs (Cheng et al., 2018; Hou et al., 2018; Li et al., 2017; C. Yan et al., 2018; G. Zhang et al., 2018).

The active layer should have suitable phase-separated domains, high domain purity, and a good bi-continuous interpenetrating network that provides not only sufficient interfaces for the effective dissociation of photogenerated excitons but also good percolation pathways for charge carrier transport to the respective electrode (Guo et al., 2021; Wan et al., 2016).

Therefore, finding a suitable method to optimize the morphology of the active layer in BHJ PSCs has very critical importance in achieving the desired photovoltaic performance. Mixed solvent (Nair & Kumar, 2016), thermal annealing (Qiu et al., 2020), solvent vapor annealing (Gurney et al., 2019), solvent additives (Dai et al., 2020; Mola et al., 2017; Oseni & Mola, 2017; Wan et al., 2016), and other methods can be used to improve the morphology of the active layer in BHJ PSCs.

Another strategy for improving device performance is to use different device architectures. A tandem structure that uses polymer stacking with sequential absorption regions to obtain a more important part of the solar spectrum (Chen et al., 2018; Ho et al., 2020; Liu et al., 2019). The main drawback in the manufacture of such solar cells lies in the technical challenge of multi-layered deposition(Xiaopeng Xu et al., 2020). In contrast, ternary BHJ solar cells afford easy fabricating steps that are the active layer can be deposited in a single step (Rao et al., 2018). Constructing Ternary PSCs (TPSCs) is a convenient strategy by utilizing the advantages of three components, either two donors and one acceptor, or one donor and two acceptors.

In a ternary-blend system, two materials having a complementary absorption spectrum are combined with a suitable acceptor. Generally, the ternary strategy helps in absorbing the most region of the solar spectrum than a single polymer system.

The normal device architecture (in which the transparent conducting oxide, typically ITO, acts as the anode) has long been the popular architecture employed for studying the performance of BHJ PSC, but the inverted device architecture (in which ITO acts as the cathode) is gaining widespread popularity for its superior stability over time, and in many cases, improved device performance. The inverted configuration is the better configuration for efficient charge collection at the respective electrodes and reduced bimolecular recombination at the electrodes, as it utilizes ETL (hole blocking layer) at the cathode (bottom) and an HTL (electron-blocking layer) at the anode (top) (Lattante, 2014).

The device must be both extrinsically and intrinsically stable for a PSC to function properly. Mechanical, oxidative, irradiation, thermal, and photochemical instabilities must all be avoided by the PSC modules. The electrodes, interfacial layers, and, most importantly, the photoactive layer and its interfaces should not be affected by degradation. Several solutions have been implemented to address the stability concerns associated with a PSC's operational lifetime. So far, five different types of tactics have been used, including encapsulation(Rafique et al., 2018), Morphology control in the BHJ photoactive layer (Chen et al., 2015; Feng et al., 2019; Zakiya et al., 2017), employing inverted geometry (Yiwen Wang et al., 2017; Wu et al., 2016), optimizing buffer layers (hole/electron transport layers) (Chaturvedi et al., 2016; Rafique et al., 2016; Sánchez et al., 2017; Singh et al., 2017; Tran et al., 2019; Yiwen Wang et al., 2017; Xiang Xu et al., 2020), and using stable electrodes.

The recent achievements in boosting device performance and stability with help of new active layer materials innovation, morphology control, and smart device architecture are summarized in Table 2.1.

Table 2.1 Achievements in device performance and stability using material innovation, morphology control, and smart device architecture

S. N	**Research area**	**Device Structure**	V_{OC} **(V)**	J_{SC} **(mA)**	**FF (%)**	**PCE (%)**	**Ref.**
1.	**Material Innovation**						
1.1	Y-series NFAs, the Y6	ITO/PEDOT:PSS/PM6:Y6/PDINO/Al	0.82	25.2	76.1	15.7	(Yuan et al., 2019)
1.2	Y-series acceptor, Y18	ITO/ZnO/PM6:Y18/MoO3/Ag	0.84	25.71	76.5	16.52	(Zhu et al., 2020)
1.3	chlorinated polymer donor, PM7	ITO/PEDOT:PSS/PM7:Y6 /PNDIT-F3N	0.882	25.60	73.3	16.56	(Ma et al., 2020)

Table 2.1 Continued.

2.	**Morphology Control**						
2.1	**Binary solvent additives**						
	Without additives	ITO/PEDOT:PSS/PTB7-Th:$PC_{71}BM$/C_{60}-N/Al	0.83	17.0	58.1	8.2	(Wan et al., 2016)
	1.5% DIO + 1.5% NMP		0.82	19.1	69.1	10.8	
2.2	**Solvent vapor annealing**						
	None	ITO/PEDOT:PSS/PTB7-Th:ITIC/Ca/Ag	0.80	14.8	60.8	7.1	(Gurney et al., 2019)
	CS_2		0.81	15.5	64.3	7.9	
3	**Device Architectures**						
3.1	**Ternary strategy**	PTB7-Th:FOIC binary	0.74	22.50	70.3	11.7	(Xie et al., 2019)
		PTB7-Th:PBDTm-T1:FOIC Ternary	0.762	24.0	73.5	13.4	
3.2	**Inverted Architecture**						
	Conventional	ITO/MoO_X/PTB7:$PC_{70}BM$/ZnO/Ag	0.75	9.36	50.29	3.52	(Xu et al., 2015)
	Inverted	ITO/ZnO/PTB7:$PC_{70}BM$/MoO_X/Ag	0.78	10.58	52.06	4.38	
3.3	Conventional	ITO/MoO_3/PBDB-T:ITIC/ZnO/Ag	0.90	15.55	67.23	9.68	(Y. Wang et al.,
	After 50 days of Aging		34% ↓	-	35% ↓	58% ↓	
	Inverted	ITO/ZnO/PBDB-T:ITIC/MoO_3/Ag	0.90	16.10	68.20	9.83	

	After 50 days of Aging		no change	-	3% ↓	2.4% ↓	2019)

↓ = Decrease

2.3 Interfacial Engineering

In terms of PCEs, the PSCs research has achieved a big milestone thanks to the development of state-of-the-art donors and non-fullerene acceptors, morphology control using different routes, and smart architectures. But for realizing the commercialization of PSC devices, the cost of these high-performing donor and acceptor materials (non-fullerene and fused ring acceptors), which is associated with their complex processing steps, poses a great challenge.

Moreover, device stability is also another factor that has not been resolved yet for the real-world application of these devices. To mitigate this challenge in the way to PSC commercialization, design strategies utilizing low-cost materials, simple processing steps, and minimizing device stability barriers are very crucial. Interfacial engineering and interface modification has proven to be powerful tool for designing efficient, stable, and low-cost PSC devices.

By lowering energy barriers for charge transport and improving compatibility between the organic active layer and inorganic metal oxides or transparent conducting electrodes, interfacial engineering using metal oxides, organic surface modifiers, and other materials can effectively improve the performance of conventional and inverted organic solar cells. The discovery of novel active layer materials with superior physical characteristics such as extended light absorption, greater charge carrier mobilities, and acceptable self-assembly capabilities when processed from organic solvents has greatly contributed to the increased efficiencies.

Although new active layer materials have helped to push the upper limits of PCEs that can be attained in OPVs even higher, the most efficient PSC devices are nearly always achieved by designing some part of the device structure in addition to the active layer. Interface engineering is a powerful tool to improve the performance of PSCs.

Introducing diverse interfacial materials to tailor device attributes so that the maximum amount of electrical energy may be extracted from a particular device is one of the most effective ways for device optimization. ETLs and HTLs are two of the most extensively used interfacial materials groups based on their function, (Fig 2.7).

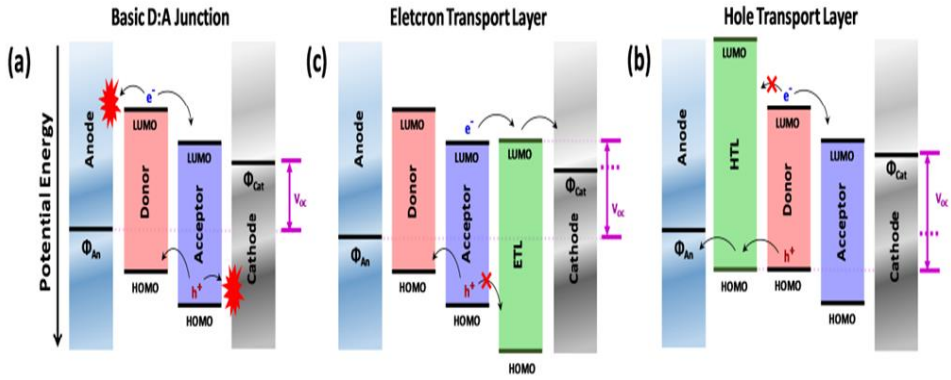

Fig 2.7 *Schematic diagrams of some basic donor, acceptor, electron, and hole transporting layers* (Walker et al., 2017).

In actuality, the design shown in Fig 2.7 (**a)** without the buffer layer suffers from two significant loss mechanisms. Without additional layers, the electric field and V_{OC} in this type of device are likely to be limited by the anode's work function (ΦAn) and cathode's work function (ΦCat); if ΦAn is above the donor's HOMO band and ΦCat is below the acceptor's LUMO band, the V_{OC} will be limited by the potential difference between them. The V_{OC} produced by the cell would be limited to 0.4 V in the case of practical anode and cathode materials such as indium tin oxide (ITO, = -4.7 eV) and aluminum (=-4.3 eV) (Walker et al., 2017).

The back-diffusion of charge carriers is another significant loss in PSC devices without buffer layers. Organic hetero-junctions work because incident light causes photoinduced electron transfer from the donor to the acceptor or photoinduced hole transfer from the acceptor to the donor (a mobile electron-hole pair is generated in either case).

Electrons migrate downwards while holes move higher along with energy bands. To produce usable electrical energy, the electrons and holes must move to the cathode and anode, respectively, after photo-generation. (Walker et al., 2017).

Although the electric field formed by the difference in work functions between the anode and cathode acts as a driving force for electrons and holes to drift to the correct electrodes, there is no additional barrier to prevent them from drifting back to the wrong electrodes. Electrons that diffuse to the anode or holes that diffuse to the cathode will recombine to their ground state and represent wasted energy, as shown in Fig 2.7 (**a)**.

The introduction of ETLs and HTLs into PSC provides a solution to the aforementioned fundamental issues in Fig 2.7 (**b)** and (**c)**. An energy barrier prevents holes from diffusing in the wrong direction by putting an interlayer with a deep HOMO level adjacent to the cathode. If the LUMO of the ETL matches the LUMO of the acceptor, the insertion of ETLs boosts the V_{OC} of PSC devices. Similarly, HTLs with high LUMO energies can prevent electrons from diffusing back to the anode, effectively deepening the anode's work function and increasing the V_{OC}. ETLs and HTLs are the most important forms of interfacial materials in PSCs, and they are also the most studied.

The majority of widely used interfacial materials are prone to deterioration, which reduces device performance dramatically. As a result, numerous options have been investigated in recent years to overcome the stability issues associated with pristine interfacial materials.

Optimization of HTL: PEDOT: PSS is the most commonly employed HTL material, but it favors the device degradation due to its acidic and hygroscopic nature. Ultimately, it corrodes the underneath ITO that further diffuses into the photoactive layer. Therefore, several alternatives materials have been reported to work as HTLs in PSCs. Among them, metal oxides-based HTLs are the most studied alternatives to the acidic PEDOT: PSS. Metal oxides such as NiO (Singh et al., 2017), V_2O_5 (Rafique et al., 2016), WO_3 (Zhan et al., 2021), and MoO_3 (Chaturvedi et al., 2016) have been widely used as HTLs in PSCs. All these materials can be processed from solution, and thus are compatible with roll-to-roll production.

Optimization of ETL: LiF and Ca are the most commonly employed ETLs in conventional and inverted geometry BHJ PSCs, respectively. These materials are unstable in the ambient atmosphere due to their reactivity with oxygen, and water. In addition, vacuum deposition is not compatible with roll-to-roll manufacturing.

As a primary requirement, an ETL should be stable, have good transparency in the visible spectral region, should collect and effectively transport negatively charge carriers (electrons), should provide an ohmic contact with the acceptor, and offer minimum series resistance. In this context, metal oxides such as Cs_2CO_3 (Xu et al., 2014), SnO_2 (Tran et al., 2019), TiO_2 (Sánchez et al., 2017), ZnO (Kim et al., 2013; Pali et al., 2018) and electron extracting polymers have been employed as alternative ETLs (Dong et al., 2017). By thermal evaporation or solution method, these metal oxides are deposited on ITO to modify their work function. Large-area fabrication, such as roll-to-roll printing, is best done with solution-processed metal oxides. Because of its high electron mobility, environmental stability, high transmittance, and ability to create diverse nanostructures via solution methods, ZnO has gained a lot of attention as an ETL among various metal-oxides (Lin et al., 2016; R. Zhang et al., 2018). This makes it ideal for roll-to-roll manufacturing onto flexible substrates.

However, sol-gel processed ZnO ETL has some shortcomings for application in highly efficient inverted PSCs, due to the numerous and unavoidable surface defects formed in the interior and on the surface of the film during sol-gel processing, which act as the electron trap sites, contributing to the severe charge carrier recombination loss in PSCs (Yaling Wang et al., 2018; R. Zhang et al., 2018).

In addition, there is a mismatch between the conduction band energy level of ZnO and the LUMO level of acceptor materials in the active layer (Lin et al., 2016). Furthermore, the incompatibility between the organic materials (active layer) and the inorganic ZnO ETL, results in a poor interfacial contact at the ZnO ETL/BHJ interface, which may lead to large series resistance, weak electronic coupling, and severe back charge recombination (Ling et al., 2019).

Therefore, the development of efficient inverted PSCs not only requires developing diverse PSCs architectures with appropriate BHJ active materials but also understanding how to manipulate charge selectivity through interfacial modifications.

Interfacial engineering using interface modification materials can effectively boost the performance of conventional and inverted PSCs, by lowering the energy barriers for charge transport and improving compatibility between the organic active layer and inorganic metal oxides or transparent conducting electrodes.

In the literature, many interfacial engineering solutions for increased charge transfer, lower recombination losses, and improved device performance have been proposed. To date, interface engineering or interfacial modification on sol-gel ZnO has been studied via doping metals, alkali metal salts, and organic materials into ZnO (Lee et al., 2019; Naz et al., 2018; R. Sharma et al., 2017; M. Wang et al., 2019; Yang et al., 2021) or deposition of a thin layer of metals or organic/inorganic materials as a second interfacial layer on top of ZnO film (Aatif & Tiwari, 2020; Azeez & Narayan, 2020; Fu et al., 2017; K. Wang et al., 2017; Wu et al., 2016; Xiang Xu et al., 2020), or making organic materials/ZnO composite ETL (Borse et al., 2018; Kadam et al., 2021). All of these approaches can prevent surface traps and defects in sol-gel ZnO, improve interfacial contact with the photoactive layer, change the WF of the electrode, increase the conductivity of sol-gel ZnO, and minimize recombination losses, all of which are advantageous to photovoltaic performance.

For instance, Yang group doped ZnO with a diphenylphosphine-oxide-based conjugated organic molecule, ((1,3,5-triazine-2,4,6-triyl)tris(benzene-3,1- diyl))tris(diphenylphosphine oxide) (PO-T2T), to improve the ETL properties in i-PSCs. They discovered that PO-T2T doping played a role in ETL morphological optimization while also undermining trap-assisted recombination by filling ZnO defects. Furthermore, electron mobility has been improved. The efficiency of the PSCs based on the fullerene system PTB7-Th:$PC_{71}BM$ was increased from 9.03% to 9.84% with the optimized functionality (Yang et al., 2021).

In an ambient atmosphere, the Kadam group used P3HT:$PC_{61}BM$ to build flexible PSCs on polyethylene terephthalate substrates to improve the performance of the device (Kadam et al., 2021). They created an efficient ETL using a nanocomposite of zinc oxide (ZnO) and polyethyleneimine ethoxylated (PEIE). PEIE doping reduced the work function of ZnO and passivates the interface, resulting in better solar cell performance. After PEIE doping, the device efficiency was effectively increased from 0.80% to 0.950% by increasing the FF and JSC. Because of PEIE, ZnO has a lower work function, which allows for simple charge transport from the photoactive layer to the cathode, increasing the FF and JSC values. Furthermore, the mechanical properties of the flexible PSCs with the ZnO:PEIE ETL improved more than those of ZnO. After 800 bending cycles, the device with the ZnO:PEIE ETL retained approximately 80% of its original power conversion efficiency (PCE).

Wu, B., et al., demonstrated suppression of ZnO sub-gap states by modifying its surface with an ultrathin Al layer, which significantly improved charge extraction and performance reproducibility, increasing the PCE from 6.9% to 8.0%, which is 15% higher than a structurally identical control cell made with a pristine ZnO interlayer. They proposed that modifying the ZnO surface with an ultrathin Al (1.2 nm) layer benefits inverted PSCs in two ways: (1) it reduces the density of the sub-gap states in the ZnO buffer, increasing charge collection efficiency and thus PCE, and (2) it significantly improves cell performance reproducibility (Wu et al., 2016).

The Fu group proposed an amino-silane as a molecular linker between the ZnO ETL and the fullerene derivative PCBM-based active layer for effective inverted polymer solar cells. The amino-silane molecular linker served two purposes for improved PCE: 1) passivating the ZnO surface and decreasing the surface work function of ZnO for energy level alignment, and 2) connecting onto the fullerene derivative PCBM-based active layer to reduce interface contact resistance. The power conversion efficiency (PCE) of the device based on the PTB7-Th/$PC_{71}BM$ active layer was increased from 8.47% to 9.46% (Fu et al., 2017).

Azeez et al. found that the addition of $PC_{70}BM$ as an interlayer between the ETL and the active layer improves the efficiency of non-fullerene acceptor-based solar cells (Azeez & Narayan, 2020). By lowering the charge transport barrier and recombination, the combination of ZnO and $PC_{70}BM$ layers between a cathode and a bulk heterojunction active layer looks to serve as a superior selective contact. The enhanced J_{SC} is distinguished by a low series resistance ($2\Omega\ cm^2$), increased charge collecting efficiency, and the device's PCE increased from 8.4% to 11.2%, representing a 33% increase in average PCE (Azeez & Narayan, 2020). The improvement in efficiency is primarily due to a significant increase in J_{SC} from 15.7 mA/cm2 to 20.7 mA/cm^2, as well as a moderate improvement in FF and V_{OC} (Azeez & Narayan, 2020). The device's excellent electron extraction using the $PC_{70}BM$ interlayer demonstrates the establishment of improved contact between the active layer and the cathode.

However, there is a little decrease in shunt resistance (Rsh) with the FF remaining essentially the same (Azeez & Narayan, 2020). These data can be understood as the inevitable mixing of the BHJ active layer at the interface of $PC_{70}BM$/BHJ due to the commonality of the solvent employed for the interface and bulk layers, eventually leading to a change in the BHJ surface morphology.

The charge extraction at the anode side is known to be influenced by morphology and non-ohmicity. Progress in thin metallic layer and organic interfacial engineering so far is summarized in Fig 2.8.

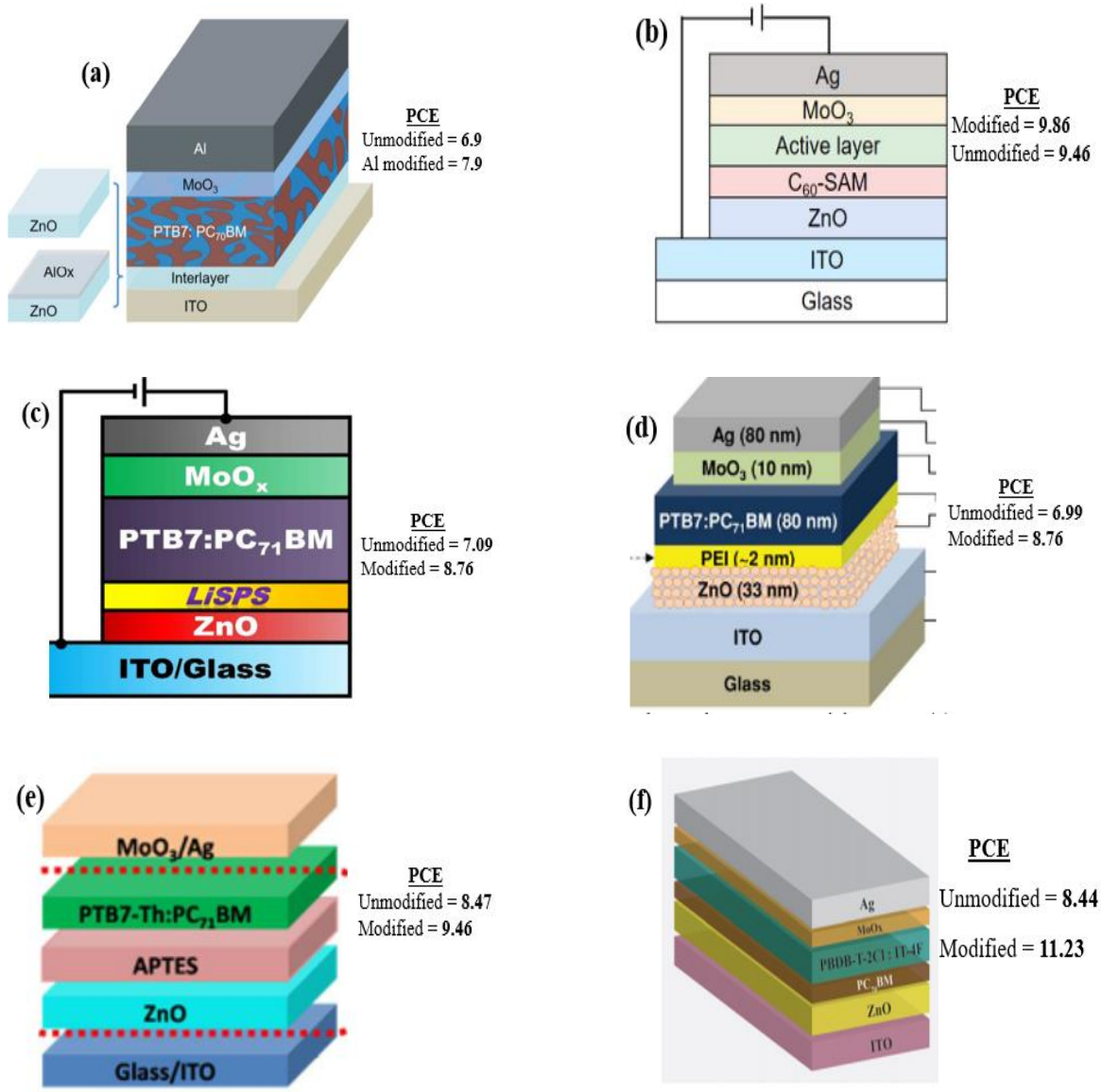

Fig 2.8 *materials used for interfacial modification in PSC* ***(a)*** *Thin layer of aluminum* (Wu et al., 2016) ***(b)*** *Fullerene based self-assembled monolayer (C60-SAM)* (Xiang Xu et al., 2020) ***(c)*** *Lithium Sulfonated Polystyrene* (K. Wang et al., 2017) ***(d)*** *poly(ethyleneimine) (PEI) polymer nanolayer* (Woo et al., 2014) ***(e)*** *Aminosilane as a Molecular Linker between the Electron-Transport Layer and Active Layer* (Fu et al., 2017) ***(f)*** *$PC_{70}BM$ fullerene interlayer* (Azeez & Narayan, 2020)

However, these organic polymer modifiers have insulating properties and are not effectively utilizing the incoming incident light, consequently limiting the device's performance. In addition, the deposition of a thin layer of metal as an interfacial modification layer is not practically feasible.

Therefore, it is necessary to find new types of interface modifiers to replace conventional organic and metal-based modifiers to achieve the desired device performance for i-PSCs. Recently, interfacial modification layers based on CDs have attracted increasing research attention due to their fascinating properties, which include; wavelength-dependent luminescence emission (Gharat et al., 2019), good water-soluble processability (Fan et al., 2017), tunable optical and electronic properties (Abdelsalam et al., 2018; Ren et al., 2019; Yifan Wang et al., 2017), and photochemical stability (Datta et al., 2016), non-toxicity (Dong et al., 2014), environmental friendliness, low-cost and simple preparation using abundant precursors (Zhou et al., 2018), making them an ideal interface modification materials for highly efficient PSC devices.

2.4 Carbon Dots (CDs)

As an emerging member of the carbon material family, carbon dots CDs have received increasing research interest since their accidental discovery in 2004. Numerous studies showed that CDs have great prospective applications in photovoltaic devices, due to their tunable electronic and optical properties (Ren et al., 2019), superior thermal and photochemical stability (Datta et al., 2016), low cost, and hypo-toxicity (Zhou et al., 2018).

2.4.1 Carbon Dots Synthesis Methods

Methods of synthesizing CDs are diverse, and various synthesis approaches have been reported for the preparation of CDs. Structural, physical, and chemical properties of CDs can easily be manipulated, which makes CDs promising materials for different applications including Photovoltaic devices. Synthesis methods of CDs can be categorized as “top-down” and “bottom-up” approaches (Feng et al., 2020; Mintz et al., 2019).

The top-down approach involves breaking down large carbon structures such as graphite, carbon soot, graphene oxide (GO), CNTs, and carbon fibers to obtain CDs by chemical, physical, and electrochemical methods (Joseph & Anappara, 2017; Shi et al., 2022; Xu et al., 2016).

Physical methods including arc discharge, laser ablation, and lithography are direct routes for transforming large carbon structures into CDs, but advanced instruments/equipment and/or distinct optics/nanotechnology often must be adopted, leading to high cost (Feng et al., 2020).

Bottom-up fabrication of CDs is condensation-crosslinking carbonization of small molecule and/or polymer precursors that comprises hydrothermal/solvothermal and microwave-assisted methods, combustion/pyrolysis, and electrochemical treatment. Bottom-up syntheses have some distinct advantages over top-down syntheses, such as higher quantum yields and more easily tunable PL colors for as-fabricated CDs, lower costs, simple and sustainable synthesis procedures, and more readily available raw materials and efficient routes to mass-produce fluorescent CDs (Feng et al., 2020). CDs can be made by dehydrating and carbonizing small compounds and polymers, for example. The chemicals employed almost often contain –OH, –COOH, –C=O, and –NH2 groups, which can dehydrate at high temperatures. Dehydration and carbonization operations can be carried out in a variety of ways, such as hydrothermal (Yingte Wang et al., 2018), microwave (de Medeiros et al., 2019), combustion methods (S. Zhang et al., 2019), pyrolysis in concentrated acid (Song et al., 2015), carbonization in a microreactor (Tang et al., 2018), enhanced hydrothermal (microwave-hydrothermal, (Zheng et al., 2018) and plasma (Park et al., 2017) methods, and so on.

Because of its gentle reaction conditions, environmental protection, and abundant precursor, solution-based hydrothermal synthesis is recognized as one of the easiest ways to customize the band structure, optoelectronic, and electrochemical properties of CDs among bottom-up approaches. For making fluorescent CDs, the hydrothermal pathway offers a simple, low-cost, efficient, and environmentally friendly method (Xu et al., 2016). More crucially, hydrothermal synthesis allows for the use of a wide range of materials for element doping in CDs (Miao et al., 2020).

2.4.2 Morphologies and Chemical Structures of CDs

The term "CDs" refers to a variety of nanoscale carbon materials. CDs, in a broad sense, are any nanosized materials made primarily of carbon (Zhu et al., 2015). As inherent properties, CDs have at least one dimension less than 10 nm in size and fluorescence. CDs are polymeric aggregations of sp^2/sp^3 carbon and oxygen/nitrogen-based groups. The most common CDs are Graphene Quantum dots (GQDs), Carbon Quantum Dots (CQDs), Carbon Nano Dots (CNDs), and Polymer Dots (PDs).

GQDs have one or more graphene layers with connected chemical groups on the edges. They have anisotropic lateral dimensions that are larger than the height. GQDs have crystallinity due to the presence of a carbon core, with an average lattice parameter of 0.24 nm, which corresponds to (100) spacing of single graphene dots on lacey support films (Lin & Zhang, 2012). CNDs are always spherical, and they are classified as carbon nanoparticles with no crystal lattice and CQDs with a visible crystal lattice (Nie et al., 2014).

CQD interlayer distances are typically around 0.34 nm, which corresponds to (002) spacing of crystalline graphite. PDs are cross-linked polymers formed by aggregation/assembly of linear non-conjugated polymers. Furthermore, the carbon core and grafted polymer chains can form PDs. Structural differences arise due mainly to the synthesis process and raw materials. On the surface of all CDs, there are connected or modified chemical groups, such as oxygen-based, amino-based groups, polymer chains, and so on. As a result, these fluorescent CDs are not made of "pure" carbon. The hybridization and coefficient between the carbon core and the surrounding chemical groups are important in the PL behavior of these CDs.

2.4.3 Optical properties of CDs

Despite the diversity of the structures, CDs possess some similar optical properties in terms of their absorption and fluorescence. CDs typically show strong optical absorption in the UV region (230–320 nm), with a tail extending into the visible range.

For the carbon core, a maximum peak at ca. 230 nm is ascribed to the π–π* transition of aromatic C–C bonds, whereas a shoulder at around 300 nm is attributed to the n–π* transition of C=O bonds or other connected groups (Wang et al., 2014). In addition, the connected chemical groups may contribute to the absorption in the UV–visible regions. The observed deviations in absorption spectra data, at least to some extent, indicate differences in the compositions or structures of different hybridization derivatives. The UV-vis absorption spectrum is red-shifted from around 420 nm to the NIR spectral region, which is directly attributed to the addition of graphitic nitrogen centers into the carbon sp2 lattice because the graphitic nitrogen centers can inject excess electrons into the unoccupied π* orbitals, thereby significantly reducing the HOMO-LUMO gap and the energies of the corresponding optical transitions (Sarkar et al., 2016). Meanwhile, functional groups containing O (hydroxyl, carboxyl, and epoxy) on the surface of CDs can narrow the energy levels, resulting in red-shifted absorption (Sudolska et al., 2015).

In terms of investigating the PL mechanism and adapting CDs for novel applications, the PL properties of CDs are the most important issue. CD emission spectra are generally symmetrical on the wavelength scale. CD emission peaks are typically broad, with large Stokes shifts when compared to organic dye emission.

The position of the emission peak is always related to the excitation wavelength, which is referred to as wavelength-dependent behavior. This behavior could be caused by a wide distribution of different sized dots and surface chemistry, different emissive traps (salvation effect), or an unresolved mechanism (Wang et al., 2013). The most common CDs have strong PL from blue to green, and a few CDs emit best in long-wavelength regions.

The literature has discussed external factors dominated emission (including the molecular state and the environment effect), internal factors dominated emission (including the conjugation effect, the surface state, and the synergistic effect), and crosslink-enhanced emission (based on structural differences).

The size effect, also known as the quantum confinement effect, is a well-known PL mechanism in which "size" refers to the sp^2 (graphene) domain—the effective conjugation length—rather than the actual particle size (Ding et al., 2018). As "size" shrinks to the nanoscale, quasi-continuous electronic levels near the Fermi level are transformed into discrete energy levels. A larger "size" in the case of CDs reduces the bandgap while increasing the PL emission wavelength. Increases in the CD's interior graphene domain result in more delocalization and more even energy distribution, reducing the energy gap between the HOMO and LUMO.

Attached states may also affect PL, with "the surface state" accounting for cases where the conjugation effect does not apply. The surface state model, in essence, explains changes in luminous sites as a result of changes in electronic energy levels (Ai et al., 2021). Surface configurations and doping atoms are the two types of surface states considered here. The former can be thought of as a broad surface structural type that includes polymers, functional groups (of varying degrees of oxidation), defects, and edge states. The latter is concerned with the effect of heteroatoms on PL, such as nitrogen, fluorine, sulfur, phosphorus, boron, etc. Many studies have shown that changing the surface state to adjust the energy structures of CDs affects their luminosity.

Surface functionalization endows CDs with new energy levels, resulting in long-wavelength (up to 650 nm) PL with a very narrow spectral width (Kwon et al., 2015). Amino modification, also known as "amino passivation," is a technique for modifying the surface configuration of CDs. According to one study, the degree of surface amination influences the PL excitation dependence of CDs (Li et al., 2014). If all surface states are passivated by amino groups, emissions occur via a single mode of sp2 carbon radiative transition that is independent of the excitation wavelength.

When surface states are not as passivated, functional groups such as C–O, C=O, and O=C–OH produce a wide range of energy levels, with fluorescent emission depending on excitation energy.

2.4.4 Hetero-atom Doping and Its Effect on Opto-electronic Properties of CDs

Even after surface passivation and/or functionalization, undoped CDs have a relatively low emission efficiency when compared to ordinary semiconductor quantum dots. As a result, efficient methods for improving the fluorescence features of CDs are extremely needed to broaden their application potential. Recently, the doping technique has been employed to modify the optoelectronic characteristics and is seen to be the most promising engineering avenue for producing extremely fluorescent CDs (Xu et al., 2016). Metal atoms and heteroatoms (non-metal) are the two broad categories of doping elements (Xu et al., 2016).

The primary disadvantage of metal-atom doping is the related increase in toxicity. As a result, non-metal-based heteroatom doping of CDs, which has received a lot of interest in recent years, will be explored.

Doping is a good way to control the intrinsic features of CDs. It can be classified as single-doped or co-doped depending on the quantity of hetero atoms put into the CDs. CDs' electronic structure can be altered by inserting atomic impurities (e.g., nitrogen, boron, sulfur, phosphorus, etc.) into them, resulting in n-type or p-type carriers. As a result, various types and amounts of doping atoms can be used to control their optical and electrical properties. Furthermore, recent research has revealed that hetero atom doping of CDs can significantly improve their QY. For these reasons, during the last decade, substantial research efforts have been focused on the creation of dopants and doping techniques.

I. Nitrogen Doping

Because of the similarities between N and C, N-doping is the most commonly utilized method for improving the PL properties of CDs. In this case, the nitrogen atom injects electrons onto CDs, altering their internal electrical environment. Bottom-up synthesis routes for N-doped CDs rely on selecting a small molecular precursor containing higher nitrogen contents. Various top-down ways for making extremely fluorescent N-doped CDs have been reported to date. One of the primary techniques focuses on harnessing the abundance and sustainability of natural biomass materials to produce a low-cost and environmentally friendly method of creating CDs.

In a simple and low-cost one-step hydrothermal process, the Wu group synthesized NCQDs with high quantum yield (54–55 % at pH 1–3) and spherical with an average diameter of 3.2 nm using the eco-friendly, widely available, and stable composition carbon source of microcrystalline cellulose and the nitrogen dopant of ethylenediamine, respectively (P. Wu et al., 2017). In comparison to CQDs, the NCQDs produced demonstrated blue fluorescence, improved optical properties, and a higher quantum yield. The presence of ethylenediamine in the reaction system not only generated certain nitrogen-containing functional groups, but it also introduced N atoms into the carbon nuclear lattice via the high-temperature hydrothermal process (P. Wu et al., 2017). The produced NCQD exhibited an absorption band in the UV range due to the absorption of the aromatic system π or the $n–\pi^*$ transition of carbonyl groups.

Peng et al. made four types of luminous N-CDs using a pyrolysis process and a sand bath in 2016. The optical, pH-sensitivity and photovoltaic properties of these CDs were investigated, and it was discovered that the nitrogen source has a significant impact on the attributes of the N-CDs obtained. The N-CDs were utilized as sensitizers in the construction of a nano-crystalline TiO2 solar cell with a photovoltaic conversion efficiency of 0.53% (Peng et al., 2016).

An examination of the review literature reveals that nitrogen-doped CDs have piqued the interest of numerous research groups. Hydrothermal/solvothermal, microwave, and pyrolysis treatments were the most common synthetic techniques, but ultrasonication, electrochemical/chemical oxidation, and arc discharge were also used.

II. Phosphorus doping

Phosphorus can act as an n-type impurity in carbon dots. In contrast to nitrogen, the phosphorus atom is larger than the carbon atom. As a result, it can function as an n-type donor, causing substitutional defects in the carbon cluster and influencing the electrical and optical properties of CDs (Miao et al., 2020). Several groups have succeeded in producing P-doped CDs from various phosphorus-containing precursors in recent years.

Anara et al. created phosphorus-doped CDs using a low-cost, environmentally friendly, and fast hydrothermal method (Molkenova & Atabaev, 2019). The CDs have a spherical shape with an average diameter of 2.8 ± 0.94 nm and exhibit excitation-dependent photoluminescence properties. The CDs also showed PL stability over a wide PH range. The prepared phosphorus-doped CDs were successfully used for the selective detection of ferric ions in water.

III. Phosphorus and Nitrogen Co-doping

Because of the synergistic effect between the doped heteroatoms in CDs, co-doping of several hetero-atoms has begun to garner increasing attention. Due to the combined benefits from each of the doped atoms, doping N and P atoms into CDs is expected to yield co-doped CDs with novel and unanticipated features.

The use of nitrogen as a dopant in the preparation of CDs is well investigated. After doping the N atom, CDs become n-type. Substitution defects will develop during sp3-bonding if phosphorus is present in the form of an n-donor. As a result, the electronic properties of CDs can be altered by doping nitrogen and phosphorus atoms to create more active sites, which will have the greatest impact on the polarizability, quantum yield, and electrochemical properties of CDs.

Xu, Q., et al., used a single-step hydrothermal method to synthesize nitrogen and phosphorous-doped carbon dots (N, P-CDs) with PLQYs of up to 53.8 % and independent emission behavior in their study (Xu et al., 2018). Furthermore, the CDs demonstrated high mono-dispersity, stable excitation-independent luminescence, and stability over a wide pH range.

The characterization of the CDs revealed that P tuned the band gap and led to the formation of a high PLQY of the N, P-CDs. They optimized the reaction conditions to produce CDs with the desired properties, and the optimized experimental conditions to produce N, P-CDs with a maximum QY of 53.8 % were a molar ratio of 19:1 for sodium citrate and diammonium phosphate, a hydrothermal reaction temperature of 170 °C, and a reaction time of 6 hours.

Huang, S., et al., used sucrose as a carbon source and 1,2-ethylenediamine (EDA) and phosphoric acid as dopants to synthesize fluorescent nitrogen and phosphorus dual-doped CDs (N, P-CDs) using a simple and rapid low-temperature heating strategy (Huang et al., 2018). The synthesis temperature is reduced to as close to room temperature as possible, making this method simpler and more convenient. The prepared N, PCDs demonstrated excellent fluorescent stability across a wide pH range (4–11), ultrahigh ion strength (3 M KCl), and longtime UV light irradiation (3 h continuously), making them promising candidates for fluorescent probes. The N and P-CDs also demonstrated excellent biocompatibility, multicolor cellular imaging, and non-cytotoxicity to human hepatocellular carcinoma HepG2 cells after 48 hours of incubation at 500 g/mL levels. These N, P-CDs emitted a strung blue light and were very sensitive to hemoglobin.

2.4.3 Carbon Dots as Interfacial Modifier in PSCs

CDs have recently been reported in the literature for usage as an electron acceptor (Cui et al., 2018), active layer dopant (Kurukavak et al., 2021), ETL (Yang et al., 2017), interfacial modification layer (Juang et al., 2018; Lin et al., 2016; Yaling Wang et al., 2018; R. Zhang et al., 2018; Zhang et al., 2017), Dual interface modifier (J. Wang et al., 2019), and buffer layer dopant (Park et al., 2021) in PSC.

When utilized as an interfacial modification layer in a PSC, CDs perform several functions that improve the device's overall performance (Lin et al., 2016; Yaling Wang et al., 2018). Passivating ZnO surface defects for improved exciton dissociation and charge extraction, improving compatibilities of inorganic ETLs and organic active layers, minimizing band mismatch between ETL and active layer for efficient charge transfer to the electrodes, and downshifting high energy UV-light into less energetic visible light are all roles that CDs play as interface modifiers.

For example, Ma et, al. synthesized Nitrogen and Sulfur co-doped CDs (N, S-CDs) as effective ZnO surface modifiers. They fabricated the i-PSCs using ITO/ZnO (or ZnO: N-CDs or ZnO:N, S-CDs)/PTB7-Th:$PC_{71}BM$/MoO_3/Al (Yaling Wang et al., 2018).

The J-V characteristic of the devices containing ZnO:N, S-CDs is light soaking free and exhibits a superior performance of 9.31%, indicating that the insertion of N, S-CDs can reduce the energy barrier and increase the charge transfer from the active layer to the ETL by eliminating the light-soaking issue and optimizing the stabilized device efficiency.

Furthermore, the slightly improved *Jsc* might be attributed to an improvement in the interfacial contact between ZnO and the photoactive layer, as well as light absorption in the photoactive layer, as a result of the introduction of the N, S-CDs (Yaling Wang et al., 2018). Table 2.2 summarizes recent work and achievements in the use of CDs as interface modifiers.

More research into the use of these intriguing materials derived from locally available bio-sources as interfacial modification materials to improve PSC device performance is critical, based on the facts discussed in these papers thus far.

Table 2.2 Summary of use of CDs as an interfacial modifier for ZnO ETL in PSCs

S. N	The precursor used for CDs Synthesis	Device Structure	V_{OC} (V)	J_{SC} (mA)	FF (%)	PCE (%)	Ref.
1	4,7,10-Trioxa-1,13-tridecane-diamino (TTDDA) and glucose	ITO/Zno/PTB7:$PC_{71}BM$/ MoO_3/Al)	0.73	15.23	67.11	7.41	(Lin et al., 2016)
		ITO/Zno/C-dots/PTB7: $PC_{71}BM/MoO_3$/Al)	0.75	17.59	68.27	9.01	
2	-	ITO/ZnO/PTB7:$PC_{71}BM/MoO_3$/Al	0.73	16.56	63.0	7.59	(R. Zhang et al., 2018)
		ITO/ZnO/ C-QDs /PTB7: $PC_{71}BM/MoO_3$/Al	0.75	19.60	66.4	9.64	
3	ascorbic acid and ammonium persulphate	ITO/ZnO/PTB7Th:$PC_{71}BM$/ MoO_3/Al	0.80	16.88	0.68	9.18	(Yaling Wang et al., 2018)
		ITO/ZnO:N,S-CQDs)/ PTB7-Th:$PC_{71}BM/MoO_3$/Al	0.80	17.20	0.68	9.36	
4	Carbonized Bamboo	ITO/ZnO/PTB7-Th:$PC_{71}BM$ MoO_3/Ag	0.79	15.1	68.3	8.2	(Juang et al., 2018)
		ITO/ZnO/CND/PTB7-Th: $PC_{71}BM$ MoO_3/Ag	0.78	16.6	72.1	9.4	

Chapter three

Methodology

3.1 Materials and Chemicals

A. Materials

For the hydrothermal synthesis of N & P co-doped CDs, a 25ml Teflon-lined stainless steel hydrothermal reactor was used. The centrifuge was used to remove unreacted organic moieties from the reaction product. Filter paper and a 0.1μm syringe filters were used. A hot plate, beakers, and a magnetic stirrer bar were used for synthesis.

B. Chemicals

Enset (Ensete ventricosum, False Banana) was bought from a local market. ortho-phosphoric acid (Merck, 85%) ethylenediamine (Merck Schuchardt OHG, 98.6%), Zinc acetate dihydrate ($Zn(CH_3CO_2)_2 \cdot 2H_2O$, Energy Chemical, 99.5%), 2-methoxy ethanol (CH3OCH2CH2OH, Energy Chemical, 99%), monoethanolamine (CJ Chemicals, 99%), Acetone (Dow Chemical, 99.5%), and Isopropanol (Dow Chemical,) were bought from a local market in Addis. Ammonium heptamolybdate tetrahydrate (Merck, 99.3 %), hydrochloric acid (HCl, E & C Chemicals, 37%), Chloroform, and Nitric acid (The Chemical Co, 69%) were obtained from the Chemistry department at Adama Science and Technology University.

3.2 Research Design

An experimental research design was used in this study. The hydrothermal synthesis method was used to make N & P co-doped CDs. The synthesis was carried out in an open atmosphere. The effect of each dopant and the doping level on the band tuning was studied by varying the doping levels of each dopant for each set of experiments, as given in Table 3.1. The material synthesis was carried out entirely at Adama Science and Technology University in the material science and engineering laboratory. The solar cell device was fabricated in an atmospheric setting and the J-V characteristics were evaluated for different device structures. The Materials Physics and Polymer laboratories of Addis Ababa University's Science Faculty were used for some of the material characterization, device fabrication, testing, and optimization activities.

Table 3.1 Research design: Variation of dopant precursor concentration

Effect of doping and doping level of each dopant on device performance (Doping concentration in molarity (M))	
Nitrogen (N)	**Phosphorus (P)**
0	0
0	0.3
0	0.6
0.06	0
0.06	0.3
0.06	0.6
0.12	0
0.12	0.3
0.12	0.6

3.3 Experimental Procedure

3.3.1 Synthesis of N & P Co-doped CDs

The enset precursor (from Pseudostem part) was washed with di-ionized water several times, and the washed precursor was dried in an oven for 12 h. The dried enset was then ground using ceramic mortar, and the ground enset was sieved with 45-micron sieve mesh to get fine powder (Fig 3.1). To make CDs, enset (false banana) powder was hydrothermally processed. A 3g of enset powder, 0.12 M of ethylenediamine, and 0.6 M of ortho-phosphoric acid were dissolved in 60ml of di-ionized water with vigorous stirring in a stirrer plate (Zheng et al., 2020).

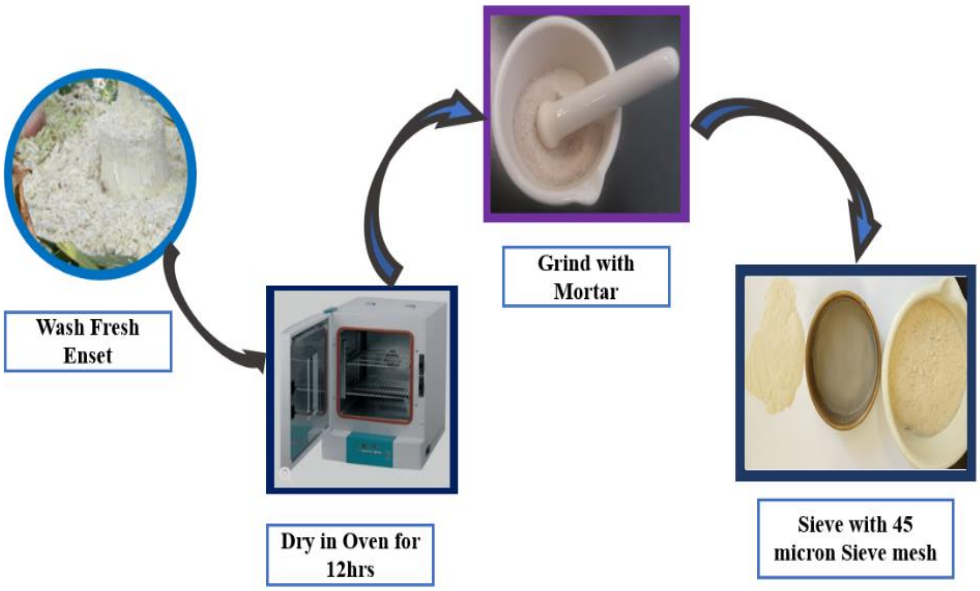

Fig 3.1 *Procedure for preparation of enset powder*

Then, the solution was transferred to a Teflon-lined stainless steel hydrothermal reactor and heated at 180°C for 6hrs (Papaioannou et al., 2019; Zhang et al., 2016). The amount of ortho-phosphoric acid and ethylenediamine was varied as given in Table 3.1, to systematically study the effect of variation of each functional group on band tuning and device performance. The undoped CDs, N-CDs, P-CDs, and N- & P-CDs with different precursor concentrations were hence synthesized. After the reaction, the autoclave was naturally cooled to room temperature. The reaction product was then centrifuged for several minutes to remove the black precipitates (unreacted organic moieties), and the resulting supernatant was subsequently filtered using 0.45-micron filter paper and 0.1-micron PTFE syringe filters to remove large-sized carbon nanoparticles. The solution was concentrated and stored in a tightly closed sample holder for further use. The procedures involved in CDs synthesis from the sieved enset powder are depicted in Fig 3.2.

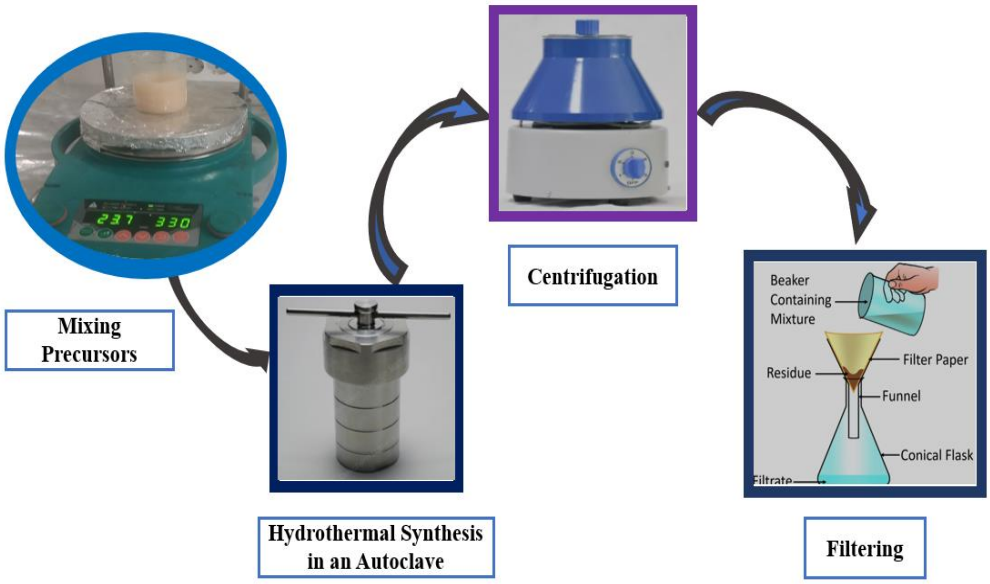

Fig 3.2 *Schematics for the synthesis of N & P co-doped CDs from enset powder*

3.3.2 ZnO ETL precursor solution preparation

A sol-gel synthesis method was used to prepare precursor solutions for ZnO ETL. The ZnO precursor solution was prepared by dissolving 5 M of zinc acetate dihydrate, and 5M monoethanolamine in 3ml of 2-methoxy ethanol. The solution was stirred overnight for the hydrolysis reaction in the air (R. Zhang et al., 2018). The solution was then stored for 6h before use for the aging purpose.

3.3.3 MoO_3 HTL precursor solution preparation

The aqueous MoO_3 solution was prepared by hydration method, where ammonium molybdate ($(NH4)_6Mo_7O_{24}$) was dissolved in water to form a specific 0.01 mol/L solution, marked as solution A. A 0.1 mol/L hydrochloric acid (HCl) water solution was marked as solution B. Solution B was dropped into solution A until the pH value of the mixed solution is adjusted between 1 and 1.5. This mixed solution, marked as solution C, is an aqueous MoO_3 solution. It is reported that this transparent solution could contain ammonium molybdate species through the following chemical reaction sequence

$$MoO_3 + 2NH_3 + H_2O \longrightarrow (NH_4)_2MoO_4$$

The as-prepared solution was stored in a clean and firmly closed flask and left for a whole night without disturbance.

3.3.4 Device Fabrication

Detailed experimental steps to prepare the inverted BHJ PSC device

1. The first stage is cleaning the ITO coated glass substrate in an ultrasonic bath with soap, DI water, acetone, and isopropyl alcohol for 15 min each. The cleaned substrates should be dried in a furnace at 120 °C for 30 min. To further clean the substrates and improve the wettability, the pre-cleaned glass substrates were subsequently treated with UV-ozone for 30 min.
2. The ZnO precursor solution was spin-coated at 2500 rpm for 30s on the UV ozone-treated ITO substrates and then thermally annealed at 250 °C for 30 min in air.
3. After cooling, the undoped-CDs, N-CDs, P-CDs, and N- & P-CDs were spin-coated on the surface of the ZnO layer at 4000 rpm for 30 s (ca. 10 nm), followed by thermal annealing at 140 °C for 10 min.
4. Then, a solution with a ratio of PTB7 to $PC_{70}BM$ (1:1.5) in chlorobenzene and with a total concentration of 25 mg/mL is prepared. The solution was stirred at 70 °C for 3hrs. The blend layer was spin-coated on top of ZnO, ZnO/undoped-CDs, ZnO/N-CDs, ZnO/P-CDs, or ZnO/N- & P-CDs ETL, with a rotation speed of 1500 rpm and rotation time of 60 s. The resulting active coated substrates are then annealed in an oven at 120 °C for 15 min.

5. The aqueous MoO_3 solution is then spin-coated onto the active layer at 3500 rpm, for 60 s. Subsequently, the spin-coated MoO_3 film is annealed at 200 ºC for 30 min in air, during which $(NH_4)_2MoO_4$ on the surface of the substrate was expected to decompose to form MoO_3 along with volatile components such as NH_3 and H_2O and the resulting MoO_3 semi-transparent film.
6. Finally, Al is deposited on the MoO_3 HTL through a shadow mask by thermal evaporation in a vacuum of 1×10^{-6} Torr, which forms a top anode. The steps involved in the device fabrication process are shown in Fig 3.3.

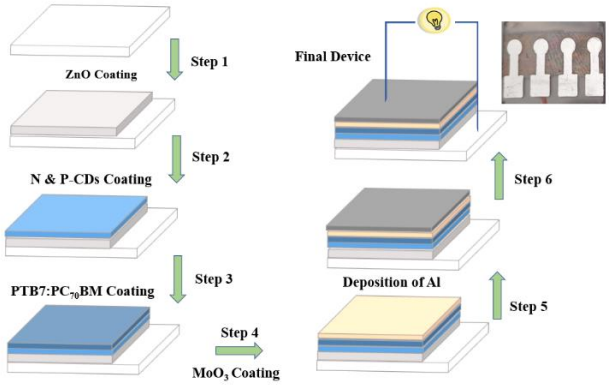

Fig 3.3 *Schematic of steps involved in the fabrication of the PSC devices*

3.3.5 Characterization

The purified carbon dots solution with fixed concentration was spin coated on a glass substrate and annealed at 140°C for 10 min, and the film samples were used for the subsequent characterizations. The morphology and crystal structure of the as-prepared CDs are characterized by Scanning Electron Microscopy (SEM, JCM-6000Plus) and X-ray Diffraction (XRD, Rigaku D/max-2500). The functional groups present in the CDs are characterized using Fourier Transform Infrared Spectroscopy (FT-IR, BRUKER TENSOR 27). The optical properties of the CDs are recorded by Ultraviolet-Visible Absorption (UV–Vis, HITACHI U3900) and Cary Eclipse Fluorescence Spectrometer. Cyclic voltammetry (CV) was used to assess the HOMO and LUMO energy levels of the CDs. The J–V features of i-PSCs measurement were carried out under solar light operating at AM1.5 and integrated power intensity of 100 mW/cm^2 with computer interfaced Keithley HP2400 source-meter and a solar simulator (model SS50AAA). The charge transfer behavior of the devices was tested using Electrochemical Impedance Spectroscopy (EIS) measurements under open-circuit voltage conditions with a frequency from 100 Hz to 100 mHz using an electrochemical analyzer (Autolab PGSTAT302N).

Chapter Four

Results and Discussions

4.1 Morphology, Composition, and Structure of the as-prepared CDs

4.1.1 XRD Analysis

The XRD results of Enset powder, bare & unfiltered CDs, nitrogen-doped CDs, phosphorus-doped CDs, and nitrogen and phosphorus co-doped CDs are shown in Fig 4.1. The XRD patterns of enset powder, undoped & unfiltered CDs, undoped CDs, N-CDs, P-CDs, and N- & P-CDs all showed broad diffraction peaks at angles of 2θ =17.08º, 20.2º, 19.07º, 20.08º, 24º, and 22.8º, respectively. The XRD patterns displayed seem broad and with a prominent peak between 17° and 25° due to the small nanoparticle size and strain in the crystalline structure. The observed diffraction peaks correspond to (002) planes of graphitic carbon and suggest the presence of a graphite-like core and amorphous carbon on the surface (Lin et al., 2016; Yaling Wang et al., 2018; Yang et al., 2019; Zhao et al., 2015).

There are additional peaks for enset powder and unfiltered CDs at angles of 2 θ = 43º, 64.5º, and 78º in Fig 4.1, which could be due to organic moieties present in the enset precursor, some of which remained unreacted during the hydrothermal synthesis and were present in the reaction product before purification, demonstrating the importance of the subsequent purification steps in the CDs production. For the purified CDs (Fig 4.1), the peaks for the unreacted organic moieties have vanished, and the XRD peak shows only a single peak due to the graphitic carbon framework.

Because the ionic radius of nitrogen and carbon atoms is nearly identical, and since the peak is broad, the peak position does not change significantly after nitrogen doping (Fig 4.1). However, due to ionic size differences between carbon and phosphorus atoms, the peak positions were shifted to higher theta values after phosphorus doping (Fig 4.1).

According to theory, adding more atoms to a structure should result in peak shifts as well as changes in intensity. Atom size differences cause repeat lengths in the crystal structure to expand or contract depending on whether the doped atom is larger or smaller than the host atom, causing peak shifts. As the electron density of the doped atom differs from that of the surrounding atoms, some peaks grow more intense, while others become less intense.

The amount of these adjustments, however, is determined by the concentration of the doping atom; if the concentration is low enough, such as at the ppm level or lower, no changes in the diffraction pattern may be observed. For a better understanding of the effect of each dopant and their concentration on the XRD peak shift (see Appendix A). From the appendix A, we can understand that as the nitrogen concentration increases the peak shift does not change that much for fixed concentration of phosphorus, however, as the concentration of phosphorus increases the peak shift also shows significant increase for fixed concentration of nitrogen.

In many materials, it is found that doping with atoms of varying sizes causes the lattice parameters to shift. If the ion is larger, it is expected that the lattice to grow and the peaks in the diffraction pattern (in 2 thetas) to shift to smaller angles (Chai et al., 2017).

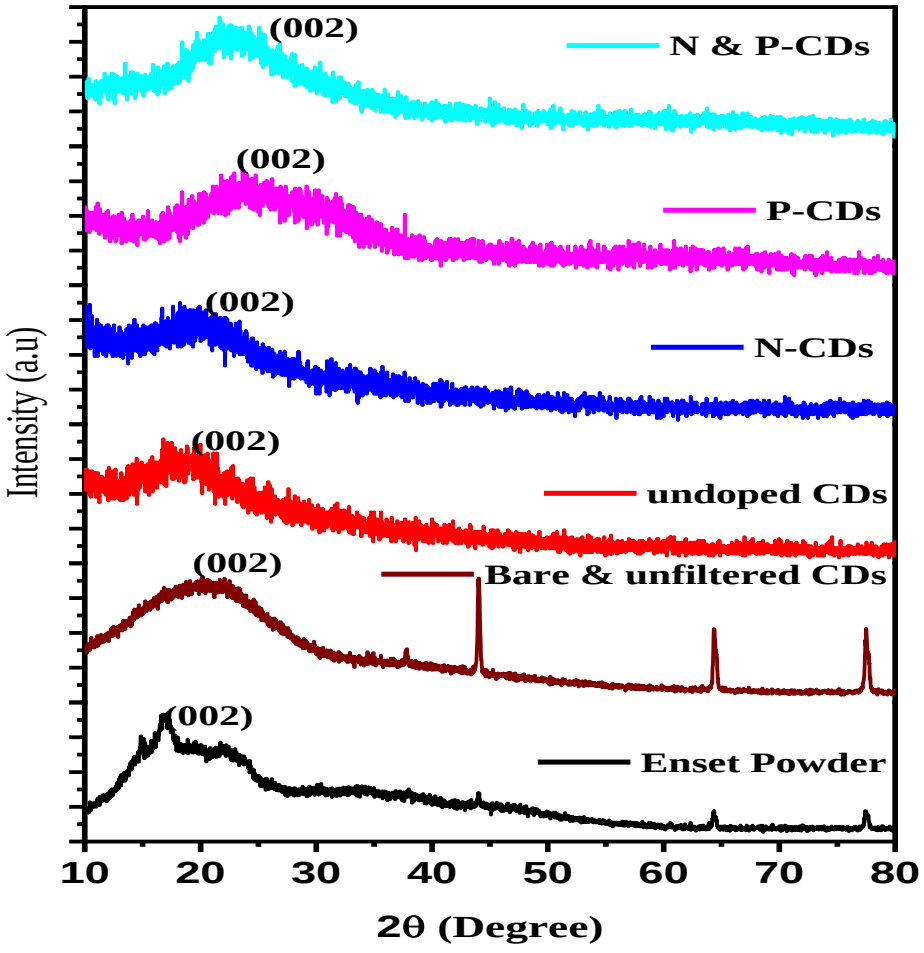

Fig 4.1 *The XRD spectrum of enset powder, CDs without filtering, CDs after filtering, nitrogen doped CDs, phosphorus doped CDs, and nitrogen and phosphorus co-doped CDs.*

However, some studies have discovered that for larger ionic radius dopants, the peaks in the diffraction pattern shift slightly towards higher 2 theta values (Hassan et al., 2014). Monitoring the peak positions of CDs diffractions allows us to investigate the possible incorporation of P and N into the CDs lattice as well as the effect of P and N doping on the crystal structure.

The interlayer spacings for the as-prepared CDs are larger than that of graphite, 0.34 nm, implying that N- & P-CDs had a larger interlayer spacing than graphite. This result could be attributed to phosphorus and nitrogen-containing groups introduced during the hydrothermal process, which increased interlayer distance. A summary of the Crystallographic parameters of the as-prepared CDs obtained from XRD data is given in table 4.1. The data in the table show that doping with nitrogen and phosphorus increased crystallite size and thus reduced peak broadening.

Table 4.1 Summary of the Crystallographic parameters of the as-prepared CDs obtained from XRD data

No	**Material**	**Doping Conc. (M)**		**2θ values**	**Peak Height (Cts)**	**FWHM**	**Crystallite Size (nm)**	**d-spacing (nm)**
		N	P					
1	Enset Powder			16.9° (M.P)	607.94	3.779	2.1	0.525
2	Unfiltered undoped CDs			20.9° (M.P)	519.6	6.298	1.3	0.426
3	Undoped CDs	0	0	19.1°	35.29	6.912	1.2	0.464
4	N-CDs	0.12	0	19.5°	28.6	3.967	2.0	0.455
		0.06	0	18.7°	20.76	4.849	1.7	0.426
5	P-CDs	0	0.6	23.4°	43.81	5.951	1.4	0.380
		0	0.3	22.8°	137.2	3.840	2.1	0.369
6	N- & P-CDs	0.12	0.6	22.4°	99.43	5.951	1.4	0.397
		0.12	0.3	22.0°	22.41	3.464	2.3	0.405
		0.06	0.6	23.1°	25.65	5.542	1.5	0.386
		0.06	0.3	23.8°	115.6	4.156	2.0	0.374

Note: M.P = Major Peak Cts = Counts

The as-prepared CDs with 0:0, 0.12:0, 0:0.6, and 0.12:0.6 doping concentrations (in M) of nitrogen and phosphorus, respectively were used for further analysis and device fabrication owing to their band positions and due to financial constraints to further investigate the all the CDs prepared.

4.1.2 FTIR Analysis

The FTIR spectrum was also used to investigate the surface functional groups on the CDs as they were prepared (Fig 4.2). As shown in Fig 4.2 **(a)**, for enset powder, peaks associated with hydroxyl (–OH) and carboxylic (COO–) group stretching vibrations are recorded at 3537.77 and 2938.02 cm^{-1}, respectively. The broad absorption centered at 2155.06 and 2043.21 cm^{-1} reveals the C-C bond's weak stretching. The C=C vibrations of aromatic compounds cause the peak at 1646.91 cm^{-1}. However, other groups, such as C=O of amide groups, did contribute to absorption in this region (called imide bands). The presence of a N–H bond is also indicated by the peak at 1347.03 cm^{-1}. C–H stretching vibrations and out-of-plane bending modes of the sp2 and sp3 –CH groups could explain the peaks at 912.17 and 993.6 cm^{-1}.

For the undoped CDs, Fig 4.2 **(b)**, the O-H stretching vibration causes the peak at 3422.06 cm^{-1}. The peak at 1630.52 cm^{-1} was caused by the conjugated structure's C = O and C = C stretching (Huang et al., 2019). C-H bond stretching vibrations were associated with the peak 1367.28 cm^{-1}. At 1030.77 cm^{-1}, the C-O-C bond's characteristic stretching band was observed.

The O-H stretching vibrations create a peak in the spectra of N-CDs at 3634.20 cm^{-1} (Fig 4.2 **(c)**). The stretching vibration of the conjugated structure C = O is assigned to the absorption peak at 1488.77cm^{-1}. The peak at 1635.34 cm^{-1}could be assigned to the stretching vibrations of C-O and the bending vibrations of N–H (Yang et al., 2012). The C–H bond stretching vibration was linked to the peak at 1366.32 cm^{-1}. The stretching vibration of the C–N bond causes the absorption peak at 1076 cm^{-1}.

The O-H stretching vibration causes the peak at 3422.06 cm^{-1} in the spectra of P–CDs (Fig 4.2 **(d)**). The stretching vibration of the N–H bond is responsible for the broad absorption peak at 3392.17cm^{-1} and the bending vibration of the N–H bond is responsible for the absorption peak at 1393.31 cm^{-1} (Shao et al., 2013; Yang et al., 2014). The conjugated structures show C = O stretching vibration and aromatic C = C vibration caused the peak at 1631.48 cm^{-1} (Huang et al., 2019). The stretching vibration of the C–N bond causes the sharp absorption peak at 1180.22 cm^{-1}. The stretching vibration of the C–O bond causes the sharp absorption peak at 1008.59 cm^{-1}. The absorption peak at 671.11 cm^{-1} was caused by the stretching vibration of PO_4^{-3} (Gong et al., 2016).

The broad absorption peak at 3476.06 cm^{-1} in N- & P-CDs is caused by the stretching vibration of the O–H bond (Fig 4.2 (e)). The sharp absorption peak at 1643.05 cm^{-1} was caused by the conjugated structure's C = O stretching vibration and aromatic C = C vibration (Huang et al., 2019).

The absorption peak at 1356.68 cm^{-1} is caused by the bending vibration of the N–H bond. The sharp absorption peak at 1082.83 cm^{-1} is caused by the stretching vibration of the C–N bond. The absorption peak at 975.80 cm^{-1} is caused by the stretching vibration of the C–O bond. The stretching vibration of PO_4^{-3} caused the absorption peak at 668.21 cm^{-1} (Shi et al., 2016).

The FTIR data provided some basic information on the sorts of functional groups present in each sample, as well as their peak positions. Certain peaks emerge as a result of hydrothermal processing and doping, whereas others fade away. Furthermore, the peak position of stretching and bending vibrations in various functional groups moves to the left or right.

For instance, the significant peak for stretching vibration of the O–H bond has been identified at 3537.77, 3422.06, 3634.20, 3422.06, and 3476.06 cm^{-1} for enset powder, undoped CDs, N-CDs, P-CDs, and N & P-CDs, respectively.

The peak wavenumber shifts for the stretching vibration of O–H bond could be ascribed to the change in bond length of the bond as a result of the changing chemical environment of the O–H bond during the hydrothermal synthesis. If the bond length decreases due to a change in the chemical environment, the peak wavenumber shifts to higher values and vice versa. Bond length changes can occur as a result of the electronegativity of the neighboring atom changing. This is similar to hydrogen bonding. What's more, the broad absorption centered at 2155.06 and 2043.21 cm^{-1} in the FTIR spectra of the enset precursor for the weak stretching of the C-C bond has vanished in the FTIR spectra of the as-prepared CDs obtained after the hydrothermal synthesis. The disappearance of these peaks could be attributed to the breaking of the weak C-C bond during the high-temperature hydrothermal synthesis, which may result in the breaking of some bonds and the formation of new bonds during the process. The FTIR spectra have also shown the appearance of stretching vibrations for functional group PO_4^{-3} at wave number around 670 cm–1 after phosphorus doping both for P-CDs and N- & P-CDs, which confirms the successful doping of phosphorus in CDs.

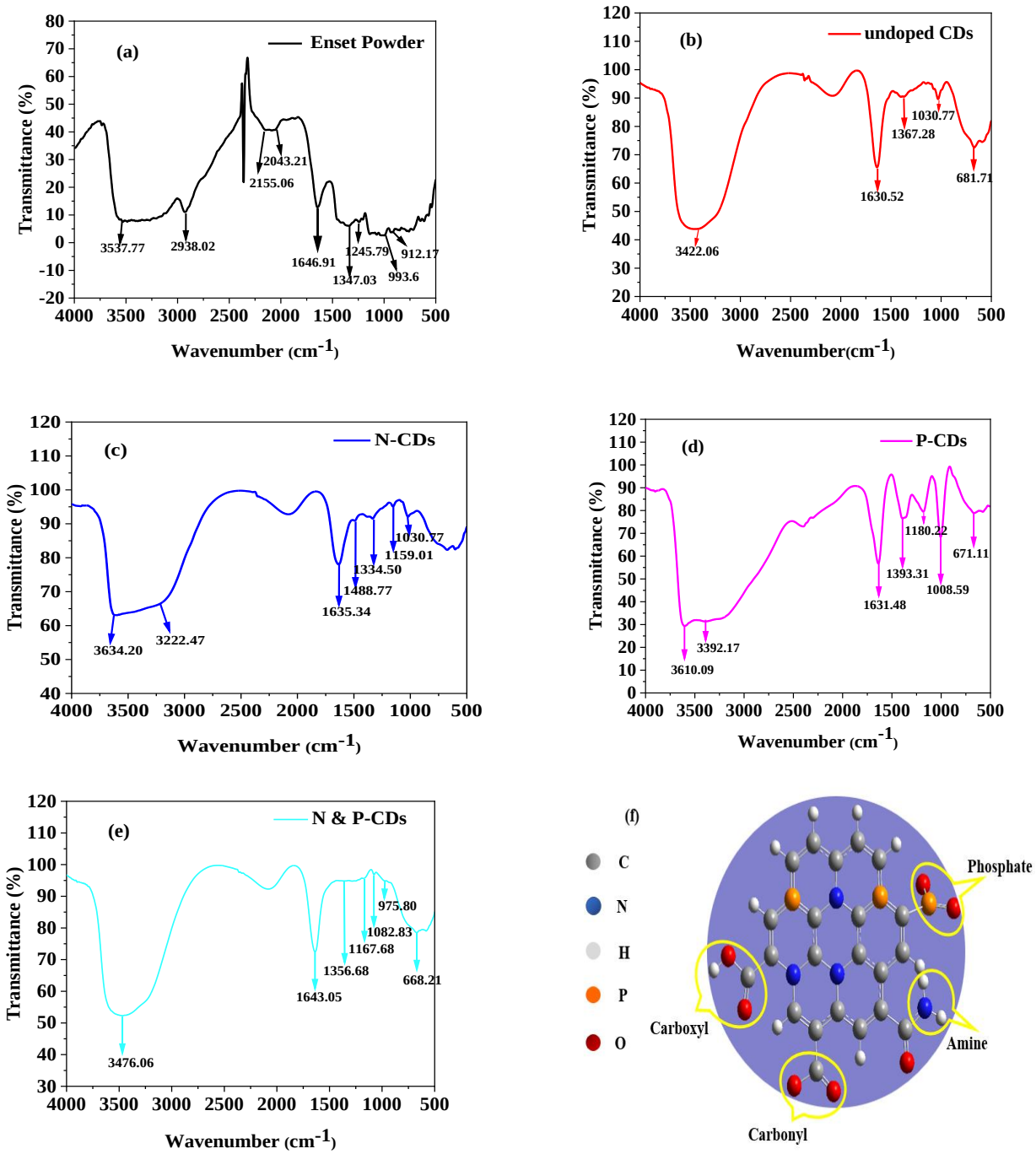

Fig 4.2 *The FTIR spectra of* ***(a)*** *enset powder,* ***(b)*** *Undoped CDs,* ***(c)*** *nitrogen doped CDs,* ***(d)*** *phosphorus doped CDs,* ***(e)*** *nitrogen and phosphorus co-doped CDs, and* ***(f)*** *Proposed generalized structure of the as-prepared N- & P-CDs.*

The FTIR results confirmed the abundance of oxygen-containing groups on the surface of the as-prepared N- & P-CDs, resulting in N- & P-CDs that were well-dispersed in an aqueous medium. As a result, the FTIR results showed that the surfaces of carbon dots were completely hydrophilic, with hydroxyl, carboxyl, amine, and phosphate groups. The hydrophilic surface is most likely responsible for the good dispersibility in water. We can confirm the possible incorporation of nitrogen and phosphorus atoms into the carbon framework, as well as the surface functionalization of the CDs with amine and phosphate functional groups, based on the XRD and FTIR analysis results. Based on the foregoing assumptions, a generalized structure of the as-prepared N- & P-CDs is proposed and depicted in Fig 4.2 (f).

4.1.3 SEM Analysis of the CDs

The topographical view of the as-prepared CDs and the ETL films used in this study is examined using SEM analysis as shown in Fig 4.3. The SEM image of the undoped CDs shows the presence of pores on the film surface, due to poor film formation as shown in Fig 4.3 **(a)**. The surface pores vary in shape and size, and they exhibit poor film morphology, which could lead to poor interfacial contact. Again, poor interfacial contact reduces charge extraction efficiency.

The N-CDs SEM image shows a more uniform film morphology than the undoped one Fig 4.3 **(b)**. Nonetheless, there are some minor surface flaws (black spots) in some sections of the film. These unevenly scattered surface irregularities could be caused by an uneven distribution of the viscous precursor solution.

The SEM image of the P-CDs revealed that the surface of the film is more or less rough, with varying degrees of roughness covering the entire surface Fig 4.3 **(c)**. The degree of surface roughness is more pronounced in some of the film's edge areas. However, due to its lower extent, this surface roughness is thought to have less impact on the interfacial contact between the ETL and the active layer, and thus on charge extraction.

The smoother surface of the CDs investigated is visible in the SEM image of the N and P-CDs as shown in Fig 4.3 **(d)**. However, the surface of N & P-CDs film has some cracks and pits. Cracks may form during the annealing process, causing uneven heating of the surfaces. Despite the presence of these surface flaws, the N- & P-CDs film surface is expected to result in better interfacial contact and thus enhanced charge extraction efficiency due to its relatively uniform surface morphology.

The SEM image of the ZnO film clearly shows the presence of large pores on the prepared film's surface as shown in Fig 4.3 **(e)**. The surface defects are larger and cover the majority of the ZnO film surface examined. These surface defects are inherent in ZnO prepared using the sol-gel method, which severely limits device efficiency via trap-assisted charge carrier recombination.

The surface of the bilayer ZnO/N- & P-CDs ETL is much smoother than the pristine ZnO, indicating that the interface passivation of ZnO by N- & P-CDs was successful as shown in Fig 4.3 **(f)**. The SEM image of the bilayer shows some minor surface aggregation. Based on the smoother surface morphology, the bilayer ETL is expected to have improved charge extraction efficiency and thus better device performance.

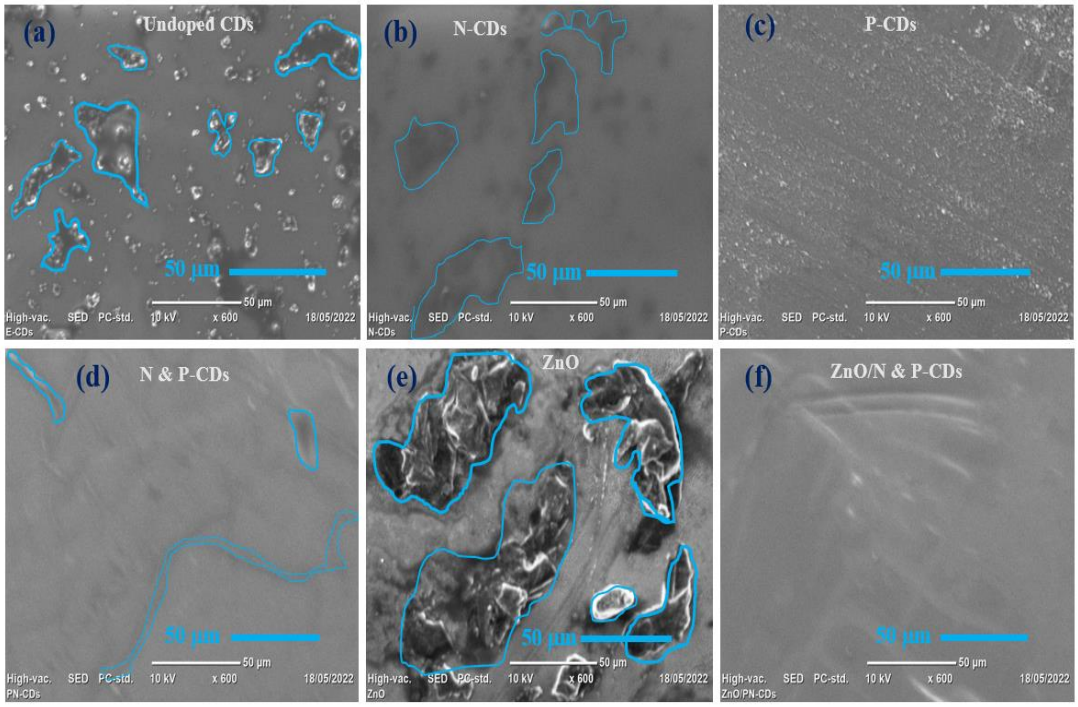

Fig 4.3 *SEM Images of* ***(a)*** *undoped CDs,* ***(b)*** *nitrogen doped CDs,* ***(c)*** *phosphorus doped CDs,* ***(d)*** *nitrogen and phosphorus co-doped CDs,* ***(e)*** *Pristine ZnO, and* ***(f)*** *ZnO/N- & P-CDs bilayer ETL films.*

4.2 Optical Properties of the CDs

UV-Vis absorption, photoluminescence (PL), and transmission spectra were collected to investigate the optical properties of the as-prepared CDs.

4.2.1 UV-Vis absorption

The CDs' UV-Vis absorption spectra are shown in Fig 4.4. Undoped-CDs have a single absorption shoulder at 285 nm Fig 4.4 **(a)**. The π–π* transition of conjugated skeletons could be assigned to this absorption shoulder. Because of its large bandgap of 3.78 eV, the undoped CDs absorb in the far UV region.

N-CDs have a sharp absorption peak at around 283nm, which could be attributed to the π–π* transition of conjugated skeletons, and another sharp peak at around 363 nm as shown in Fig 4.4 (b), which could be attributed to the n- π * transition of lone pair electrons from nitrogen (Z. L. Wu et al., 2017). Because of the introduction of graphitic nitrogen mid-gap state in the carbon framework, the bandgap of N-CDs, which is 3.11 eV, is much lower than that of undoped CDs. The graphitic-N produces a mid-gap energy state between the HOMO and LUMO of undoped carbon dots, resulting in a narrowing of the bandgap (Hola et al., 2017).

The P-CDs also showed two absorption peaks at around 273 and 333 nm, which were caused by the π–π* transition of conjugated electrons and the n- π* transition of lone pair electrons from phosphorus, respectively, which are characteristics of hetero-atom doped CDs absorption Fig 4.4 **(c)**. Because of the incorporation of phosphate states in the mid-gap, the bandgap of P-CDs is estimated to be around 3.28 eV.

The absorption peak for N- & P-CDs shows two prominent absorption peaks at around 283 and 343 nm, which can be attributed to the π–π* transition of conjugated electrons and the n- π* transition of lone pair electrons from nitrogen and/or phosphorus, as discussed previously for heteroatom doped CDs Fig 4.4 **(d)**. In general, doped N and P both donate extra electrons to carbon dots, thereby favoring the n- π * transition. To get a thorough understanding of the effect of these dopants and their concentration on the absorption behavior and bandgap tuning of the as-prepared CDs (see Appendix B). From the appendix it is clearly evident that the nitrogen doping results in greater band gap decrease compared to phosphorus doping. Furthermore, the results show that both nitrogen and phosphorus reduce the band gap of carbon dots by introducing mid-gap states between the LUMO and HOMO of the carbon dots.

The UV-Vis absorption spectra of the donor PTB7 alone and PTB7 with different ETLs were also recorded to investigate the changes in device absorption behavior as a result of the different ETLs involved in the fabrication of the i-PSC devices Fig 4.4 **(e)**.

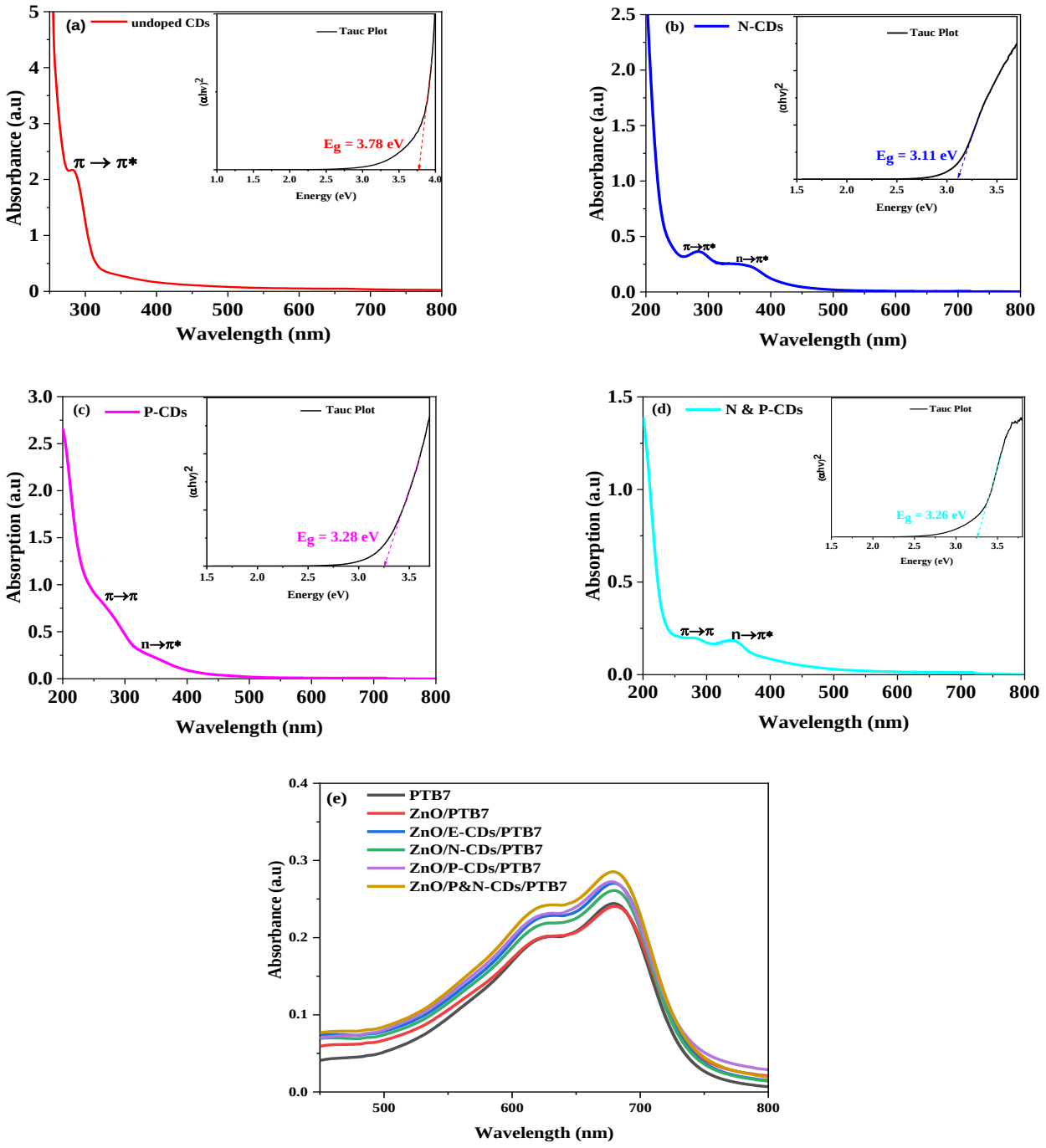

Fig 4.4 *UV-Vis Absorption spectra of* ***(a)*** *undoped CDs,* ***(b)*** *nitrogen-doped CDs,* ***(c)*** *phosphorus-doped CDs,* ***(d)*** *nitrogen and phosphorus co-doped CDs, along with their respective Tauc, and* ***(e)*** *UV-Vis Absorption spectra of the donor PTB7 without ETL and with different ETL combinations.*

The absorption spectra results depicted in Fig 4.4 **(e)** show that the insertion of the as-prepared CDs as an interfacial layer between the ZnO ETL and the active layer improves the active layer's absorption slightly. The increase in active layer absorbance may be attributed to the down-shifting behavior of the CDs (Lin et al., 2016; Riaz et al., 2019). As-prepared CDs convert high energy UV light that would not be absorbed by the active layer into lower-energy visible light that can be absorbed by the active layer (as clearly shown in the CDs' PL spectra), increasing active layer absorbance in its absorption region and thus it is expected to contribute to an increase in J_{SC} of the devices with bilayer ETL.

4.2.2 Photoluminescence

The as-prepared CDs have excellent dispersibility and emit bright blue light under 365 nm UV light as shown in Fig 4.5 **(e)**. The as-prepared CDs exhibit an excitation-dependent Photoluminescence character, similar to previous reports on fluorescent carbon dots Fig 4.5 (Yaling Wang et al., 2018).

For undoped CDs, N-CDs, P-CDs, and N & P-CDs, the maximum PL peak shifts from 455 to 565 nm, 453 to 567 nm, 478 to 560 nm, and 465 to 570 nm, respectively, as the excitation wavelength gradually increases from 360 to 520 nm in 20 nm increments. The results from the PL spectra indicate that the CDs can down-shift the higher energy UV light to lower-energy visible light (Yaling Wang et al., 2018).

After nitrogen and phosphorus co-doping, the intensity of the PL is shown to be increased. An electron-rich system with phosphorus doping and nitrogen dopant may improve the PL intensity. The defect state emission from the hetero-atom-containing groups can be attributed to a plausible PL mechanism of the as-prepared CDs. What's more, surface modification groups with varying energy levels influence the excitation-dependent PL behavior (Zhu et al., 2015).

The prepared CDs have numerous functional groups on their surface, as shown by FT-IR, which may result in a variety of emissive traps. Nitrogen doping raises the Fermi level, which increases the number of electrons in the conduction band, resulting in a very high quantum yield. Nitrogen introduces a disruption in the orientation of the carbon hexagonal matrix, resulting in an emission energy trap state that favors electron-hole pair radiative recombination.

The incorporation of nitrogen atoms into carbon dots changes the internal electronic environment of the CDs and improves photoluminescence. Doped nitrogen, has a significant influence on photoluminescence enhancement. Phosphorus, in addition to nitrogen, is used in the synthesis of n-type doped CDs. Phosphorus incorporation into the N-doped carbon dots system enhances the effect of nitrogen through a cooperative effect. The addition of a phosphorus atom eliminates the O-related states while increasing the N-related states.

It is discovered that n-type doping (phosphorus and nitrogen co-doping) improves the quantum yield for undoped CDs, as evidenced by an increase in emission intensity of the CDs when an excess free electron is introduced into the system. Previous research has shown that graphitic-N has an electron-doping effect that reduces the electronic energy gap, but other types of doped nitrogen, such as pyridinic, pyrrolic, or amino-N, have no effect on tuning the electronic energy gap (Hola et al., 2017).

We can see a change in the bandgap of the as-prepared CDs with nitrogen doping from the UV-vis results, revealing the presence of graphitic nitrogen, which is responsible for band tuning. The graphitic-N generates a mid-gap energy state in between the HOMO and LUMO of undoped carbon dots which causes the reduction of band gap followed by redshifting photoluminescence. The nitrogen atom generates a new surface state energy level, causing the emission wavelength to shift to the red. Nitrogen-doped surface states can promote radiative recombination while suppressing non-radiative recombination.

The HOMO-LUMO gap is narrowed by these newly created intermediate states, making electron transitions easier at low excitation energies or in longer wavelength regimes. A Tauc plot was used to calculate the variation in excitation energy. For undoped-CDs, N-CDs, P-CDs, and N & P-CDs, the HOMO-LUMO gap determined by the x-intercept was 3.78, 3.11, 3.28, and 3.26 eV, respectively. The probable electron transitions of the CDs are presented in Fig 4.5 (f) based on the UV-Vis absorbance and Tauc plots. As a result, the surface states reduced the CDs' bandgap, resulting in longer wavelengths or strong Stokes shift emission. When the energy difference between surface states created by functional groups and the LUMO level of the CDs is small, the stokes shift is small, and the band gap shrinks slightly; however, when the surface states are far from the LUMO levels, electrons lose much of their energy through non-radiative electron transitions to the surface states (relaxation), and the stokes shift increases.

The stokes shifts vary with excitation wavelenght for each types of CDs, and are summarized in table 4.2. The electron-donating amino groups on the CDs surface can increase the conjugation degree of conjugated systems, increasing the electron transition from the ground state to the lowest excited singlet state, and thus indirectly contribute to the CDs' higher QY.

The mechanism of CD PL emission can be explained as follows: under the action of optical pumping, first photons can be absorbed via electronic transitions from lower and occupied carbon electronic states to higher and empty states. Then, using non-radiative electronic transition events, photoexcited electrons can be relaxed into edge states or surface states, created by surface functional groups. Finally, photon emission can be achieved through electronic transitions from edge states to lower carbon electronic states. As a result, the edge electronic states behave similarly to semiconductor radiative impurity states, and electrons can be combined with holes to produce luminescence.

Excitation dependence is an important issue in the photoluminescence of carbon dots. Electrons are pumped into higher energy states in the conduction band under relatively shorter wavelength excitation, further away from radiative electronic states induced by surface modulation (Tang et al., 2019). As a result, shorter wavelength excitation reduces the possibility of photon emission from CDs. In a shorter wavelength regime, the intensity of the PL emission increases with excitation wavelength. Longer wavelength excitation implies that fewer electrons can be pumped into the conduction band in CDs in a relatively long wavelength regime. As a result, in a long excitation wavelength regime, the intensity of the PL emission decreases with increasing excitation wavelength. Generally, with increasing excitation wavelength, the intensity of the PL emission first increases, then falls. Almost all nanostructured materials exhibit this effect. According to ref (Singh et al., 2018), heterogeneous surface states, as well as the sizes and electronic characteristics of the heteroatoms, cause the intensity of the PL emission to be dependent on excitation for CDs.

The presence of surface states in CDs with surface group modulation can change the bandgap and radiative energy states of the CDs. It is also widely assumed that the photoluminescence of carbon dots is caused by surface states. Lower concentrations of amine functional groups on the surface are reported to cause excitation-dependent emission (Barman & Patra, 2018).

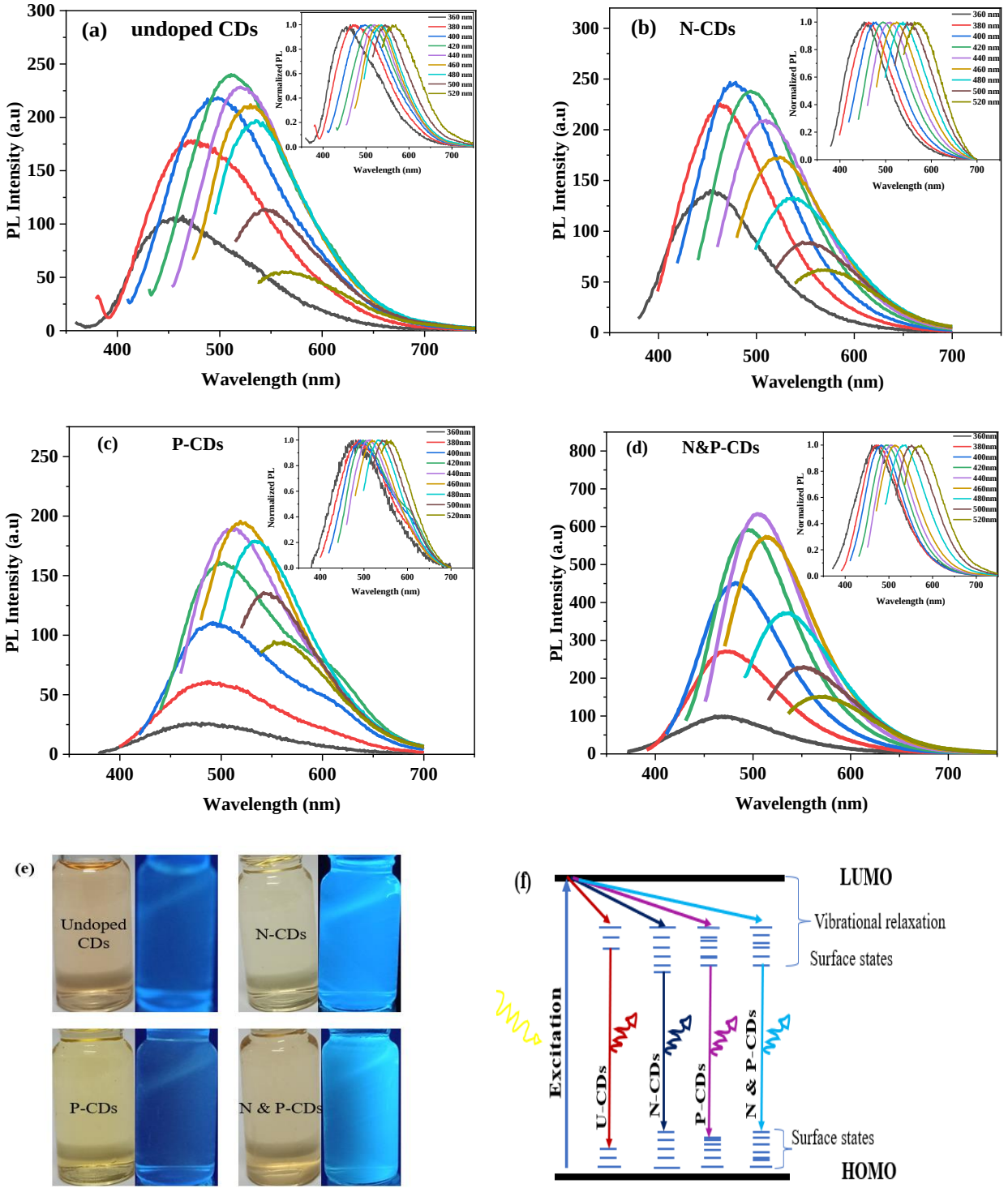

Fig 4.5 *Photoluminscence spectra of* ***(a)*** *Undoped CDs,* ***(b)*** *nitrogen doped CDs,* ***(c)*** *phosphorus doped CDs,* ***(d)*** *nitrogen and phosphorus co-doped CDs,* ***(e)*** *photograph of CDs solution in water under visible light (****left****), and under 365 nm UV light (****right****), and* ***(f)*** *The probable electron transitions of the CDs.*

Table 4.2 Excitation wavelength and associated emission wavelength and stoke shift values for each CDs

	Undoped CDs		**N-CDs**		**P-CDs**		**N & P-CDs**	
Excitation (nm)	Emission (nm)	Stoke's Shift	Emission (nm)	Stoke's Shift	Emission (nm)	Stoke's Shift	Emission (nm)	Stoke's Shift
360	455	95	453	93	478	118	465	105
380	475	95	463	83	487	107	473	93
400	500	100	478	78	492	92	482	82
420	510	90	494	74	498	78	495	75
440	520	80	510	70	510	70	506	66
460	530	70	525	65	520	60	516	56
480	537	57	537	57	535	55	536	56
500	545	45	552	52	542	42	551	51
520	565	45	567	47	560	40	570	50

To achieve high performance in PSCs, photo-generated excitons must be effectively quenched at the donor/acceptor interface in BHJ (Anger et al., 2006). We measured steady-state photoluminescence to investigate the exciton quenching effect of the as-prepared CDs (PL). The PL quenching experiment used pure donor material film rather than BHJ blend film due to the efficient exciton quenching in the BHJ (R. Zhang et al., 2018). Fig 4.6 depicts the photoexcited PL spectra of samples with the structure ITO/ETL/PTB7 excited at 532 nm. The samples with a bilayer ZnO/CDs ETL show much lower PL intensity than a pristine ZnO ETL, indicating higher exciton quenching at the bilayer ETL/active layer contact, which may lead to the improvement of Jsc. As can be seen, the radiative decay of excitons to the ground state corresponds to a PL maximum of the pristine PTB7 at around 790 nm when excited at 532 nm (Lu et al., 2013). On the other hand, PTB7 with different ETLs showed a significant decrease in peak intensity. This PL quenching, which is associated with effective exciton dissociation and extraction, is caused by efficient charge transfer due to the insertion of interface modification layers (Lu et al., 2013).

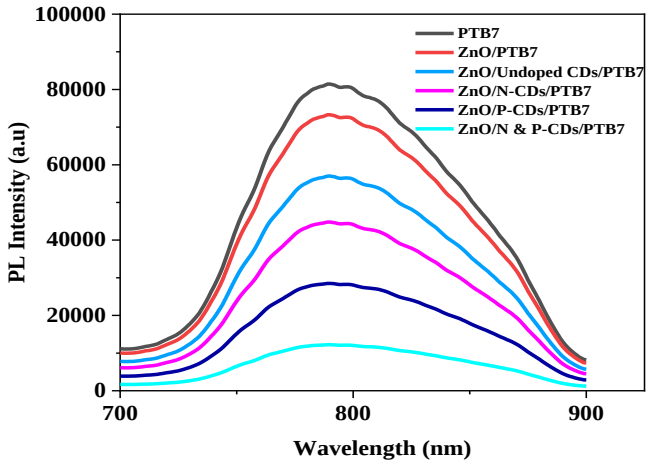

Fig 4.6 *PL spectra of PTB7 with different ETL combinations*

4.2.3 Optical Transmission

The optical transmission characteristics of the as-prepared CDs and the different ETLs were measured to further investigate the optical transmittance of the different ETLs, (Fig 4.7). Using bare glass as a reference, it was discovered that all thin films exhibit good light transmittance (above 90%), implying that the CDs have a good optical transmittance to be used as an interface modification layer for ZnO ETL in an i-PSC.

What's more, the hybrid ETL thin films incorporating ZnO and the as-prepared CDs ETL buffer layers have also demonstrated excellent optical transmission characteristics (the optical transmittance of the bilayer not enhanced but not affected significantly), which shows that they are qualified to be an ETL for i-PSCs. As a result, visible light can pass through the ITO/ETL into the polymer active layer without incurring significant absorption losses.

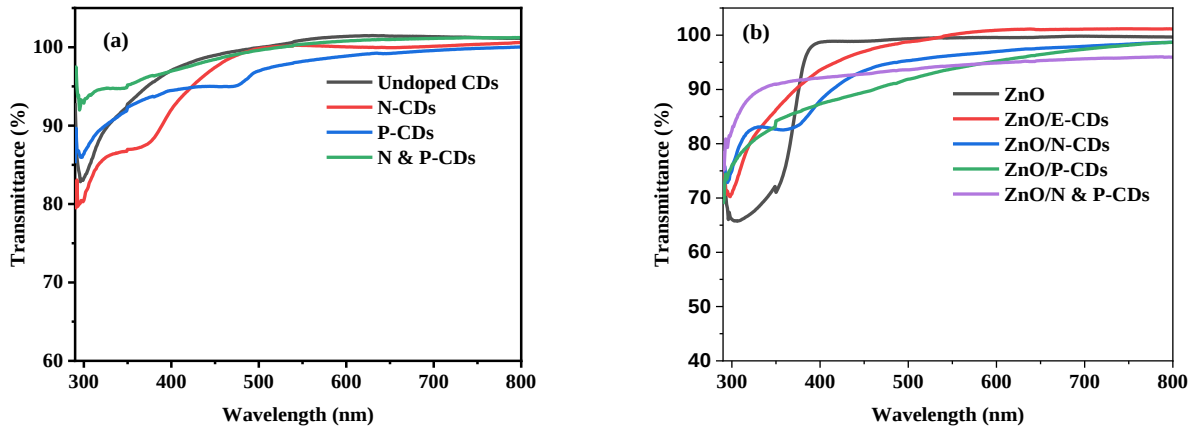

Fig 4.7 *Transmission spectra of* ***(a)*** *the as-prepared CDs and* ***(b)*** *ZnO/CDs bilayer ETL*

4.3 Electrical and Electrochemical Properties of N & P-CDs

4.3.1 Cyclic Voltammetry Analysis

Using a standard three-electrodes, ITO coated glass as the working electrode, a Pt-wire counter electrode, and an Ag/AgCl reference electrode, Cyclic Voltammetry (CV) was used to assess the HOMO and LUMO energy levels of the CDs.

The ECL signals of the CDs were recorded using cyclic voltammetry in NaCl electrolyte, with the potential sweeping between -1.0 and 1.0 V at a scan rate of 0.1 V s^{-1}. The reduction potential of the CDs is depicted in Fig 4.8. The equations below are used to calculate the HOMO and LUMO energy levels of CDs (Bayat & Saievar-Iranizad, 2017, 2018).

$$E_{LUMO} = -e(E_{Red,vs.NHE} + 4.75) \quad (1)$$

$$E_{HOMO} = -e(E_{Ox,vs.NHE} + 4.75) \quad (2)$$

$$E_{NHE} = E_{Ag/_{AgCl}} + 0.197 \quad (3)$$

$$E_{HOMO} = E_{LUMO} - E_g \quad (4)$$

where E_{Ox} and E_{Red} are the initial values of the CDs' oxidation and reduction potentials, respectively. As a result, the corresponding LUMO levels were calculated using Equations (1) and (3). The experimental constant reported for Ag/AgCl redox is -4.75 eV. The resulting LUMO levels of undoped CDs, N-CDs, P-CDs, and N- & P-CDs are given in Table 4.2.

Because of the irreversible nature of the oxidation behavior, the HOMO energy could not be obtained directly from CV results. We combine E_{LUMO} with the optical energy bandgap (E_{g}, resulting from the absorption edge in the absorption spectrum) to determine the HOMO levels of the CDs. The HOMO of undoped CDs, N-CDs, P-CDs, and N- & P-CDs are provided in Table 4.2. The findings of the CV and UV-Vis absorption measurements have clearly shown the bandgap tuning of the as-prepared CDs with the help of hetero-atom doping.

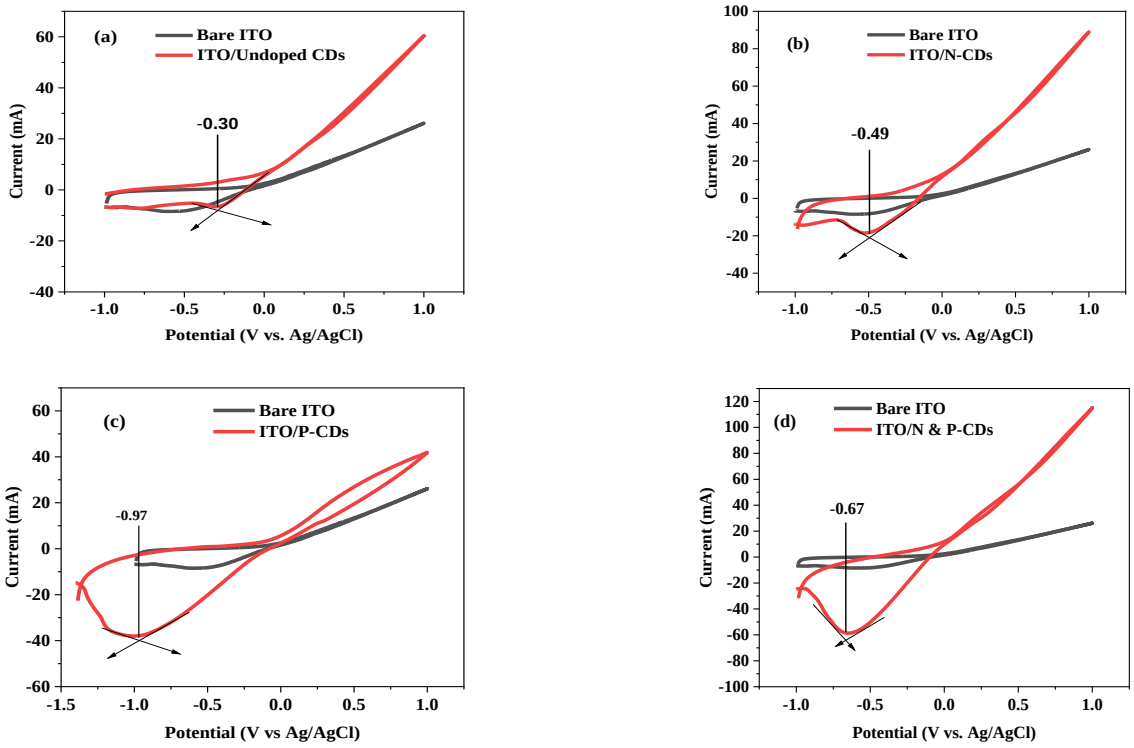

Fig 4.8 *Cyclic voltammetry measurements of the CDs/ITO and bare ITO electrodes*

Table 4.3 Summary of the Cyclic voltammetry results and the band gaps of the CDs

No	Material	Onset of Reduction Potential (E_{red} (V))	LUMO (eV)	HOMO (eV)	Band Gap
1	Undoped CDs	-0.30	-4.65	-8.43	3.78
2	N-CDs	-0.49	-4.45	-7.57	3.11
3	P-CDs	-0.97	-3.98	-7.26	3.28
4	N- & P-CDs	-0.67	-4.28	-7.54	3.26

According to the results obtained from CV and UV-Vis absorption, electron-donating groups such as $–NH_2$ and PO_4^{-3} introduced through nitrogen and phosphorus doping raise the HOMO and LUMO energy of the as-prepared CDs, which is similar to prior observations on the effect of functional groups on the tuning of HOMO-LUMO levels of CDs (Mandal et al., 2012). The energy levels of the as-prepared CDs are shown in Fig 4.9, to provide a detailed understanding of the shifting of HOMO and LUMO positions as different functional groups are introduced into the carbon dots framework upon doping with different dopants.

According to the Fig 4.9, electron-donating groups shift both the HOMO and LUMO energies to higher energy in comparison to –H passivated CDs, and the greater the electron-donating ability of the group, the greater the energy shifting, so PO_4^{-3} as a result of phosphorus doping has the highest electron donating ability, and thus shows the greatest shift of the HOMO-LUMO levels of the as-prepared CDs. The introduction of these functional groups via hetero-atom doping allowed us to systematically tune the HOMO-LUMO position as well as the bandgap of the as-prepared CDs, allowing them to be effectively used in the i-PSC to minimize the band mismatch between ZnO ETL and the active layer.

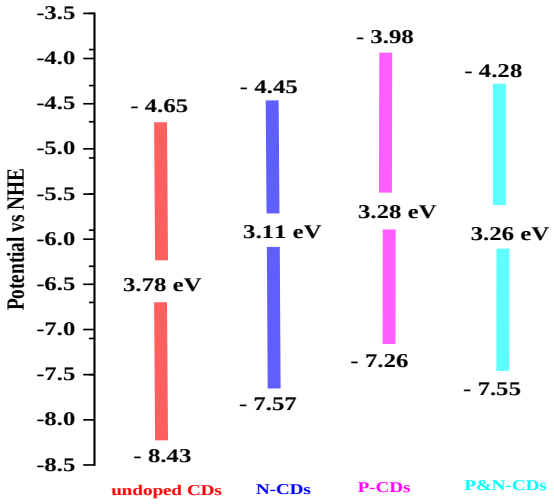

Fig 4.9 *Calculated bandgap of CDs from UV-Vis absorption data.*

4.3.2 Flat band potential determination

ETL materials and ETL modification materials used in BHJ PSCs are expected to have n-type conductivity as one of the primary requirements. The conductivity types for the representative CDs, i.e., undoped and N- & P-CDs, are determined using the Mott-Schottky analysis (Fig 4.10). The Mott-Schottky equation can be used to fit linear regions of $1/C^2$ (C is capacitance) versus applied potential. Negative linearity indicates the presence of p-type conductivity, whereas positive linearity indicates the presence of n-type conductivity (Y. Yan et al., 2018).

Despite the presence of weak electron-donating –OH groups, the as-prepared CDs exhibit n-type conductivity due to the strong electron-withdrawing oxygenated groups (e.g., -COOH and -CHO). The horizontal intercepts of the positive linear extrapolations of $1/C^2$ determine the Fermi levels of n-type conductivity (EFn).

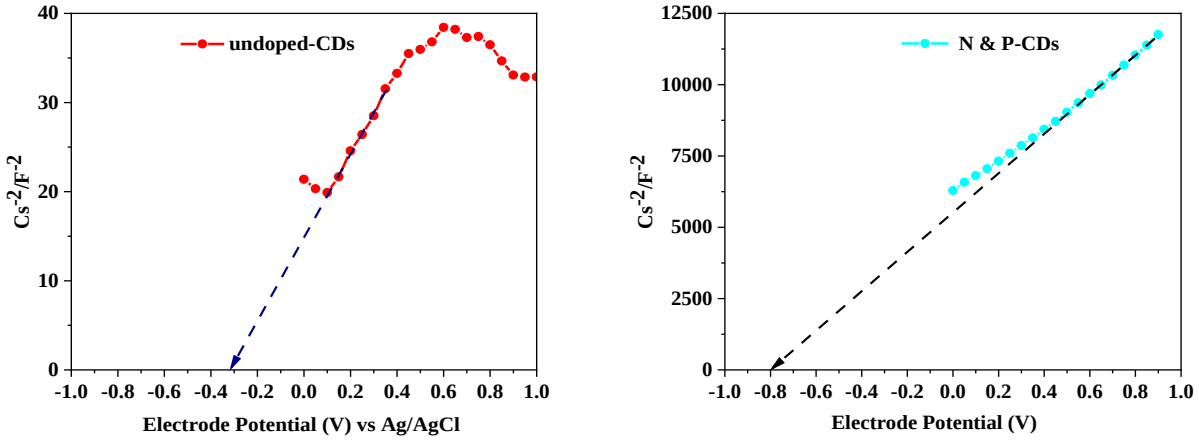

Fig 4.10 *Mott−Schottky plots of the as-prepared CDs under dark conditions with a three-electrode system in a 0.5 M NaCl solution (pH 6.5).*

The Fermi levels of n-type conductivity (EFn) and p-type conductivity (EFp) are determined by the horizontal intercepts of the positive or negative linear extrapolations of 1/C2 respectively.

4.3.3 Electrochemical Impedance Spectra (EIS)Analysis

EIS analysis was also conducted to investigate the charge transport characteristics of the devices, as well as to correlate charge transfer dynamics with improvements in ETL morphology with the insertion of the CDs. The Nyquist plots of a complete device excluding HTL with various ETL, namely ZnO alone, ZnO: undoped CDs, ZnO: N-CDs, ZnO: P-CDs, and ZnO: N- & P-CDs is depicted in Fig 4.10. The EIS experiment was conducted in the dark and Nyquist plots are fitted by a Garcia–Belmonte equivalent circuit. The series resistance, ETL/BHJ interface resistance, and internal resistance of the active layer are represented by R_1, R_2, and R_3, respectively. Furthermore, the Constant Phase Element (CPE), which in our circuit is represented by Q_1 and Q_2, is a universal defective capacitance involving surface roughness and heterogeneity (Conings et al., 2011).

The chi-square (χ^2) or goodness of fit obtained for the fitting of the device using the Garcia–Belmonte equivalent circuit are 11.74, 2.059, 1.656, 0.4581, and 0.6858, for ZnO, ZnO/undoped CDs, ZnO/N-CDs, ZnO/P-CDs, ZnO/ N- & P-CDs ETL devices, respectively.

In this study, when compared to the ZnO alone device, the ETL/BHJ interface resistance (R_2) of ZnO: undoped CDs, ZnO: N-CDs, ZnO: P-CDs, and ZnO: N- & P-CDs decreases dramatically from 103.4 Ohm to 84.04, 78.16, 37.88, and 28.9, respectively, indicating that interfacial modification of ZnO ETL using N- & P-CDs may bring about the reduction of the ETL/BHJ interface resistance and consequently facilitate electron transport between ETL and the active layer. The EIS results are consistent with the previously discussed SEM, steady-state PL spectra, and cyclic voltammetry analysis.

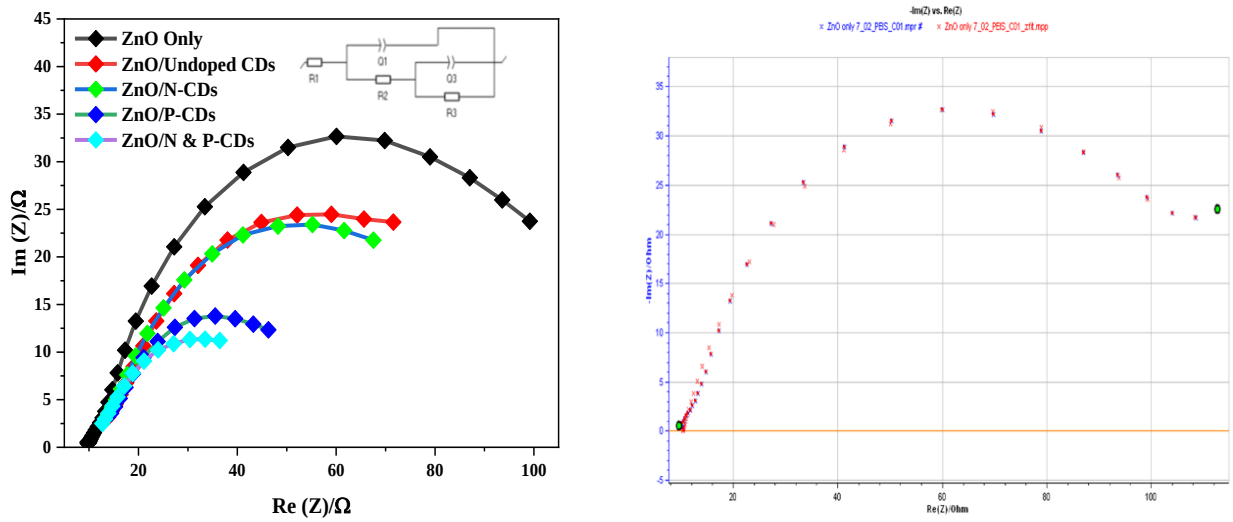

Fig 4.11 (a) *Nyquist plot of the ZnO and ZnO: CDs bilayer ETL based devices (Inset: equivalent circuit model), and* ***(b)*** *Fitted curve using the equivalent circuit.*

The internal resistance of the device is known as series resistance, and it has several components that affect its value, including the interfacial connection, active layer resistance, electrode resistances, and connect and interconnect resistances. The distance between the ITO electrode and the active blend, known as the ITO-bridge, was discovered to increase the device's series resistance. The device area is another factor that influences series resistance (Zidan et al., 2021). The above-mentioned factors could explain the change in the series resistance of the device under investigation. There was also a change in the active layer's internal resistance, which could be attributed to variations in active layer thickness and uneven film morphology. Table 4.4 summarizes the device parameters extracted from EIS data using the equivalent circuit.

Table 4.4 EIS curve fitting parameters for ETL only devices with different ETL combinations.

ETL	**R_1 (Ω)**	**R_2 (Ω)**	**R_3 (Ω)**	**Q_1**	**Q_2**
ZnO	10.33	103.4	65.74	1.497e-3	0.083
ZnO/Undoped CDs	12.61	84.04	43.74	4.488e-3	0.108
ZnO/N-CDs	12.29	78.16	32.92	3.716e-3	0.105
ZnO/P-CDs	11.25	37.88	61.54	5.287e-3	0.084
ZnO/N & P-CDs	9.617	28.9	28.34	5.925e-3	0.099

4.4 Application of the CDs as Interface Modifier for ETL in i-PSC

Given the abundance of polar groups for N- and P-CDs, such as amino, carbonyl, and phosphate groups, which can coordinate with the metal cation and thus passivate the oxygen vacancy defects of metal oxide nanoparticles. As a result, the question of whether N- and P-CDs can be used as surface modifiers for ZnO in inverted PSCs is discussed. Inverted PSCs with an ITO/ZnO (or ZnO:undoped CDs, ZnO: N-CDs, ZnO:P-CDs, or ZnO: N- & P-CDs)/ PTB7:PC_{70}BM/MoO3/Al device combination were created (Fig 4.12). Fig 4.12 (c) shows the J-V characteristic curves of the PTB7:PC_{70}BM solar cells using pristine ZnO, ZnO: undoped CDs, ZnO: N-CDs, ZnO: P-CDs, or ZnO: N- & P- CDs as ETL. Table 4.3 summarizes the important photovoltaic properties, V_{OC}, J_{SC}, FF, and PCE, of all devices. The reference device for PTB7:PC_{70}BM-based PSCs had a V_{OC} of 0.297V, a J_{SC} of 7.236 mA cm^{-2}, FF of 27.639 %, and a PCE of 0.594 %. The results show that device with the N- & P-CDs modification layer achieved the best device performance, with a V_{OC} of 0.336V, a J_{SC} of 8.986 mA cm^{-2}, FF of 28.614 %, and a PCE of 0.864 %. The J_{SC} obtained for the optimal PSC with a bilayer ZnO/N- & P-CDs ETL, is 19.5% higher than the reference cell, resulting in a 31.25 % increase in PCE compared to a reference cell.

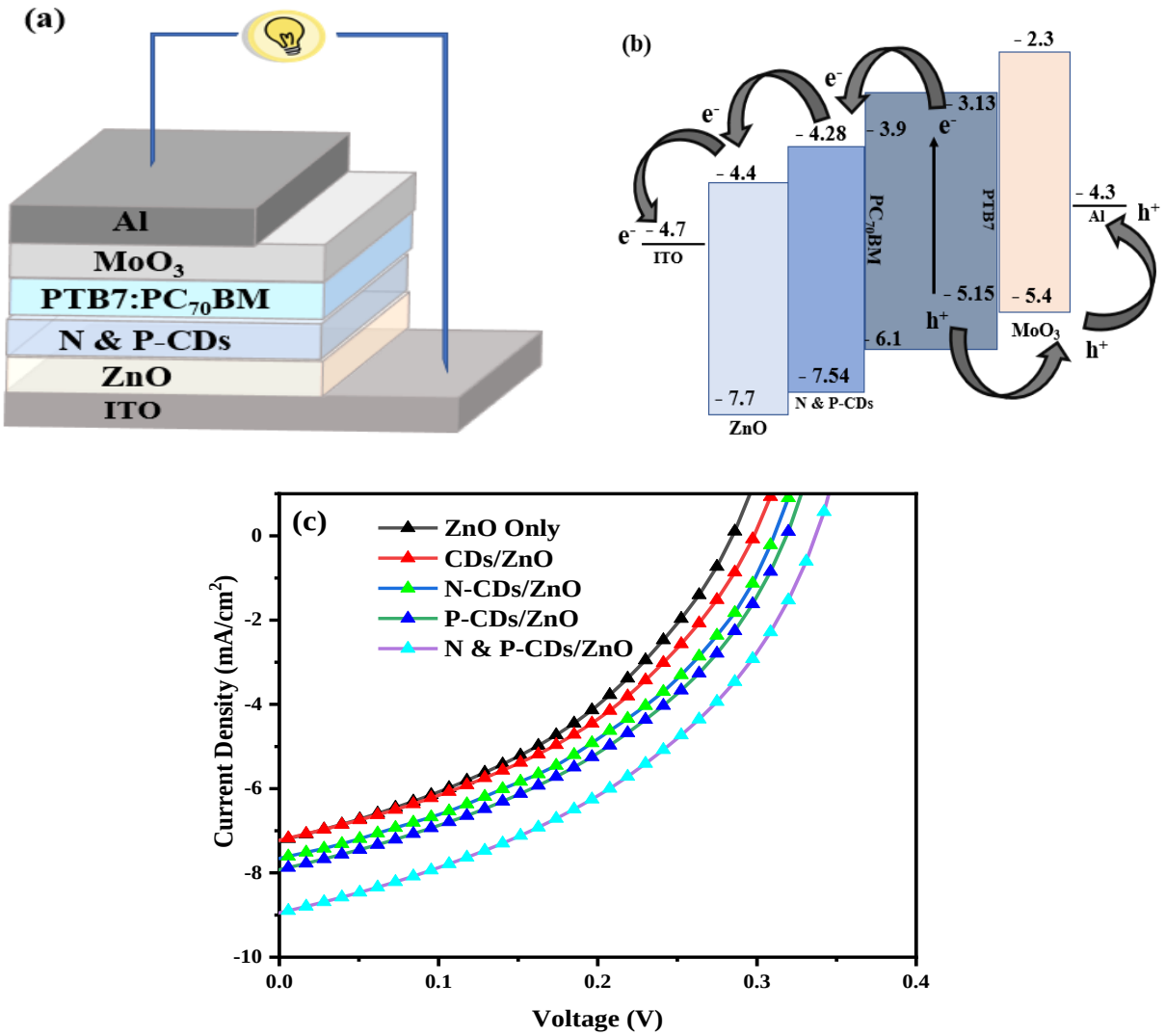

Fig 4.12 (a) *Device configuration of the inverted PSCs with the ZnO/N- & P-CDs bilayer ETL, and* ***(b)*** *the energy band diagram of the device* ***(c)*** *J-V characteristic curve of the fabricated devices with different ETLs.*

The increase in J_{SC} for ZnO/CDs bilayer ETL device originates from the improved photon absorption of the active layer as a result of the insertion of the CDs between ZnO and the active layer. The improved performance of PTB7:PC70BM-based solar cells demonstrates the superiority of solution-processable bilayer ZnO/N- & P-CDs ETL for use in inverted BHJ PSCs. A systematic investigation of morphology and charge transfer behavior measurements discussed previously demonstrates that the surface morphology of ETL in PSCs is critical in determining device performance.

Our prediction for improved device performance, stated in previous sections, has been confirmed by correlating the SEM image analysis, steady-state PL spectra, and cyclic voltammetry results with the achieved improvement in device performance. Overlayered CDs can passivate structural defects on the surface of ZnO ETL, resulting in improved contact quality at the ETL/BHJ interface and facilitating charge transport and extraction properties in PSCs. As a result, improvements in ETL surface morphology, band mismatch minimization, and improved compatibility between ZnO ETL and the active layer are responsible for improved i-PSCs performance.

Table 4.5 Photovoltaic parameters of the ZnO, ZnO:as-prepared CDs based PTB7:$PC_{70}BM$ solar cell devices.

ETL	V_{OC} **(V)**	J_{SC} **(mA/cm^2)**	**FF (%)**	**Efficiency (%)**	R_S **(Ω.cm)**	R_{SH} **(Ω.cm)**
ZnO	0.297	7.236	27.639	0.594	1210.774	620.125
ZnO/Undoped CDs	0.310	7.212	27.414	0.614	999.847	1143.969
ZnO/N-CDs	0.323	7.641	28.281	0.697	863.909	1141.138
ZnO/P-CDs	0.327	7.916	28.011	0.725	821.896	877.814
ZnO/ N- & P-CDs	0.336	8.986	28.614	0.864	330.603	1090.187

Each device's performance reproducibility was also determined. Each solar cell device has four diodes, and the efficiencies obtained from the four diodes were recorded, demonstrating that all of the devices have good performance reproducibility, with devices with P-CDs and N & P-CDs showing the best performance reproducibility among the devices studied. Fig 4.14 shows the reproducibility of each device's performance.

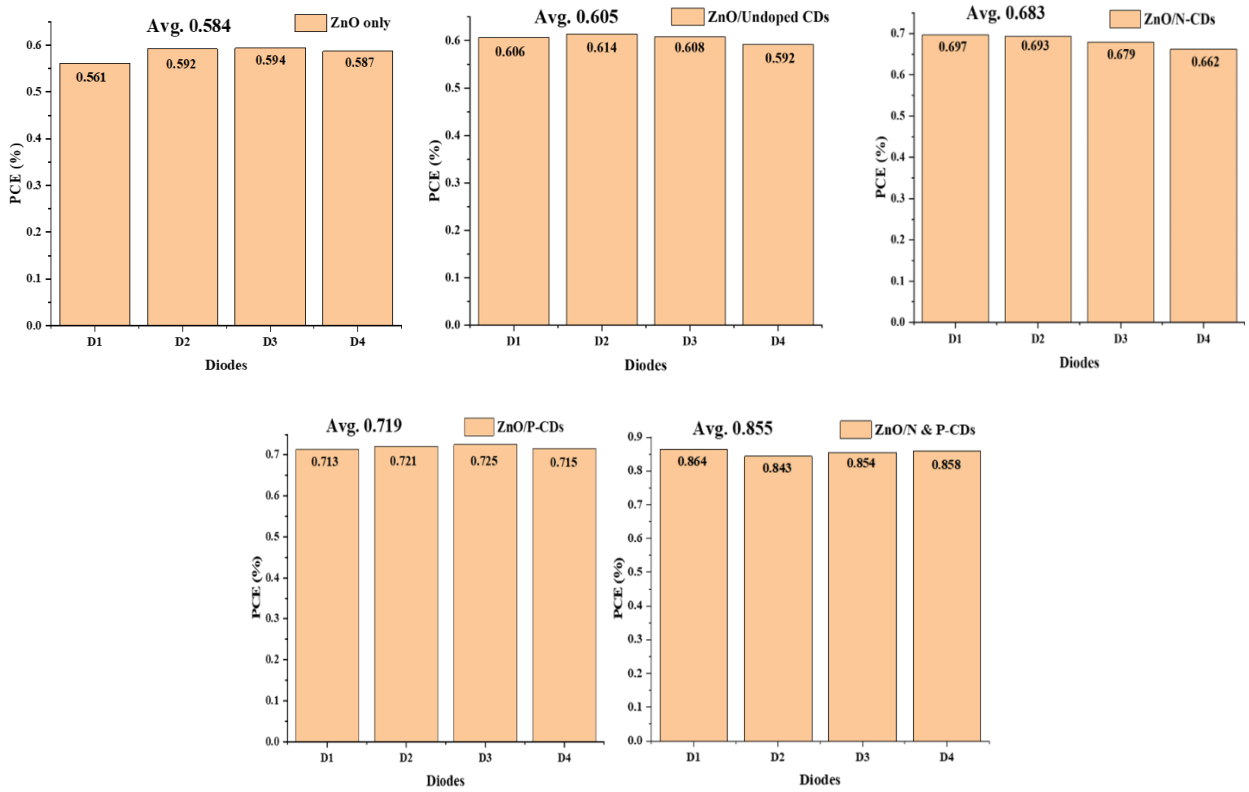

Fig 4.14 *Performance reproducibility of devices with different interface modification layer*

5. Conclusions

Water-soluble N- & P-CDs were successfully developed. The benefits of solution-processable bilayer ZnO/N & P co-doped CDs ETL were investigated in PTB7:$PC_{70}BM$ based i-PSCs. The N- & P- CDs interfacial modification layer aids in the passivation of surface defects of sol-gel processed ZnO ETL and improves contact quality between ZnO ETL and $PC_{70}BM$ acceptor for efficient transport of electron at the BHJ/ETL interface. The results show that using a bilayer ZnO/N- & P-CDs ETL, can suppress exciton quenching and reduce charge carrier recombination in PSCs. The N- & P-CDs interface modification not only minimizes the band mismatch between ZnO ETL and $PC_{70}BM$ acceptor and roughness of the ZnO ETL but also improves photo-generated charge carrier collection which contributes to performance improvement of the solar cell. In comparison to a reference cell with only ZnO ETL, PTB7:$PC_{70}BM$-based PSCs with a bilayer ZnO/N- & P-CDs ETL achieved more than 31 % performance improvement. Overall, the N and P co-doped one is showing better performance compared to only ZnO. If we can improve the device fabrication by controlling the thickness and uniformity of other layers, can improve the efficiency further. The results indicate that the water-soluble N- & P-CDs developed in this study have the potential to be used in solution-processable large-area PSCs and encourage the use of low-cost carbon-based materials for high-performance photovoltaic devices.

6. Recommendations

The scope of this work is somewhat constrained by time, work environment, and economic considerations. Some recommendations for future work can be made based on the findings. The as-prepared CDs demonstrated the potential to improve PSC performance. However, a thorough investigation into the potential use of these fascinating materials as interface modifiers in PSCs is required, so we recommend that the investigation be conducted in a conducive environment with adequate facilities. Based on the properties of the as-prepared CDs, we also recommend further research into the potential use of these materials as ETL, active layer acceptor, and active layer dopant to improve device performance.

Reference

Aatif, M., & Tiwari, J. (2020). Futuristic electron transport layer based on multifunctional interactions of ZnO/TCNE for stable inverted organic solar cells. *RSC advances*, *10*(69), 42305-42317.

Abdelsalam, H., Elhaes, H., & Ibrahim, M. A. (2018). Tuning electronic properties in graphene quantum dots by chemical functionalization: Density functional theory calculations. *Chemical Physics Letters*, *695*, 138-148.

Abdulrazzaq, O. A., Saini, V., Bourdo, S., Dervishi, E., & Biris, A. S. (2013). Organic solar cells: a review of materials, limitations, and possibilities for improvement. *Particulate science and technology*, *31*(5), 427-442.

Ai, L., Yang, Y., Wang, B., Chang, J., Tang, Z., Yang, B., & Lu, S. (2021). Insights into photoluminescence mechanisms of carbon dots: advances and perspectives. *Science Bulletin*, *66*(8), 839-856.

Anger, P., Bharadwaj, P., & Novotny, L. (2006). Enhancement and quenching of single-molecule fluorescence. *Physical review letters*, *96*(11), 113002.

Arias, L. A., Rivas, E., Santamaria, F., & Hernandez, V. (2018). A review and analysis of trends related to demand response. *Energies*, *11*(7), 1617.

Azeez, A., & Narayan, K. (2020). Enhanced device performance via interfacial engineering in non-fullerene acceptor based organic solar cells. *Applied Physics Letters*, *117*(4), 043302.

Baran, D., Ashraf, R. S., Hanifi, D. A., Abdelsamie, M., Gasparini, N., Röhr, J. A., Holliday, S., Wadsworth, A., Lockett, S., & Neophytou, M. (2017). Reducing the efficiency–stability–cost gap of organic photovoltaics with highly efficient and stable small molecule acceptor ternary solar cells. *Nature materials*, *16*(3), 363-369.

Barman, M. K., & Patra, A. (2018). Current status and prospects on chemical structure driven photoluminescence behaviour of carbon dots. *Journal of Photochemistry and Photobiology C: Photochemistry Reviews*, *37*, 1-22.

Bayat, A., & Saievar-Iranizad, E. (2017). Synthesis of green-photoluminescent single layer graphene quantum dots: determination of HOMO and LUMO energy states. *Journal of Luminescence*, *192*, 180-183.

Bayat, A., & Saievar-Iranizad, E. (2018). Vertically aligned rutile TiO2 nanorods sensitized with sulfur and nitrogen co-doped graphene quantum dots for water splitting: an energy level study. *Journal of Alloys and Compounds*, *755*, 192-198.

Borse, K., Sharma, R., Gupta, D., & Yella, A. (2018). Interface engineering through electron transport layer modification for high efficiency organic solar cells. *RSC advances*, *8*(11), 5984-5991.

Chai, B., Yan, J., Wang, C., Ren, Z., & Zhu, Y. (2017). Enhanced visible light photocatalytic degradation of Rhodamine B over phosphorus doped graphitic carbon nitride. *Applied Surface Science*, *391*, 376-383.

Chaturvedi, N., Swami, S. K., & Dutta, V. (2016). Electric field assisted spray deposited MoO3 thin films as a hole transport layer for organic solar cells. *Solar Energy*, *137*, 379-384.

Chen, C. P., Huang, C. Y., & Chuang, S. C. (2015). Highly thermal stable and efficient organic photovoltaic cells with crosslinked networks appending open-cage fullerenes as additives. *Advanced Functional Materials*, *25*(2), 207-213.

Chen, S., Yao, H., Hu, B., Zhang, G., Arunagiri, L., Ma, L. K., Huang, J., Zhang, J., Zhu, Z., & Bai, F. (2018). A nonfullerene semitransparent tandem organic solar cell with 10.5% power conversion efficiency. *Advanced Energy Materials*, *8*(31), 1800529.

Cheng, P., Li, G., Zhan, X., & Yang, Y. (2018). Next-generation organic photovoltaics based on non-fullerene acceptors. *Nature Photonics*, *12*(3), 131-142.

Cheng, P., & Zhan, X. (2016). Stability of organic solar cells: challenges and strategies. *Chemical Society Reviews*, *45*(9), 2544-2582.

Conings, B., Baeten, L., Boyen, H.-G., Spoltore, D., D'Haen, J., Grieten, L., Wagner, P., Van Bael, M. K., & Manca, J. V. (2011). Influence of interface morphology onto the photovoltaic properties of nanopatterned ZnO/Poly (3-hexylthiophene) hybrid solar cells. an impedance spectroscopy study. *The Journal of Physical Chemistry C*, *115*(33), 16695-16700.

Cui, B., Yan, L., Gu, H., Yang, Y., Liu, X., Ma, C.-Q., Chen, Y., & Jia, H. (2018). Fluorescent carbon quantum dots synthesized by chemical vapor deposition: An alternative candidate for electron acceptor in polymer solar cells. *Optical Materials*, *75*, 166-173.

Czolk, J., Landerer, D., Koppitz, M., Nass, D., & Colsmann, A. (2016). Highly Efficient, Mechanically Flexible, Semi-Transparent Organic Solar Cells Doctor Bladed from Non-Halogenated Solvents. *Advanced Materials Technologies*, *1*(9), 1600184.

Dai, T., Li, X., Zhang, Y., Xu, D., Geng, A., Zhao, J., & Chen, X. (2020). Performance improvement of polymer solar cells with binary additives induced morphology optimization and interface modification simultaneously. *Solar Energy*, *201*, 330-338.

Datta, K. K. R., Qi, G., Zboril, R., & Giannelis, E. P. (2016). Yellow emitting carbon dots with superior colloidal, thermal, and photochemical stabilities. *Journal of Materials Chemistry C*, *4*(41), 9798-9803.

de Medeiros, T. V., Manioudakis, J., Noun, F., Macairan, J.-R., Victoria, F., & Naccache, R. (2019). Microwave-assisted synthesis of carbon dots and their applications. *Journal of Materials Chemistry C*, *7*(24), 7175-7195.

Demirbas, A. (2017). Future hydrogen economy and policy. *Energy Sources, Part B: Economics, Planning, and Policy*, *12*(2), 172-181.

Ding, H., Wei, J. S., Zhang, P., Zhou, Z. Y., Gao, Q. Y., & Xiong, H. M. (2018). Solvent-controlled synthesis of highly luminescent carbon dots with a wide color gamut and narrowed emission peak widths. *Small*, *14*(22), 1800612.

Dong, S., Hu, Z., Zhang, K., Yin, Q., Jiang, X., Huang, F., & Cao, Y. (2017). Cross-Linkable and Dual Functional Hybrid Polymeric Electron Transporting Layer for High-Performance Inverted Polymer Solar Cells. *ADVANCED MATERIALS*, *29*(34), 1701507.

Dong, Y., Lin, J., Chen, Y., Fu, F., Chi, Y., & Chen, G. (2014). Graphene quantum dots, graphene oxide, carbon quantum dots and graphite nanocrystals in coals. *Nanoscale*, *6*(13), 7410-7415.

Fan, Y. Z., Zhang, Y., Li, N., Liu, S. G., Liu, T., Li, N. B., & Luo, H. Q. (2017). A facile synthesis of water-soluble carbon dots as a label-free fluorescent probe for rapid, selective and sensitive detection of picric acid. *Sensors and Actuators B: Chemical*, *240*, 949-955.

Feng, T., Tao, S., Yue, D., Zeng, Q., Chen, W., & Yang, B. (2020). Recent advances in energy conversion applications of carbon dots: from optoelectronic devices to electrocatalysis. *Small*, *16*(31), 2001295.

Feng, W., Lin, Z., Cui, J., Lv, W., Wang, W., & Ling, Q. (2019). Photoactive layer crosslinking in all-polymer solar cells: Stabilized morphology and enhanced thermal-stability. *Solar Energy Materials and Solar Cells*, *200*, 109982.

Fu, P., Guo, X., Wang, S., Ye, Y., & Li, C. (2017). Aminosilane as a molecular linker between the electron-transport layer and active layer for efficient inverted polymer solar cells. *ACS Applied Materials & Interfaces*, *9*(15), 13390-13395.

Ganesamoorthy, R., Sathiyan, G., & Sakthivel, P. (2017). Fullerene based acceptors for efficient bulk heterojunction organic solar cell applications. *Solar Energy Materials and Solar Cells*, *161*, 102-148.

Getie, E. M. (2020). Poverty of Energy and its Impact on Living Standards in Ethiopia. *Journal of Electrical and Computer Engineering*, *2020*.

Gharat, P. M., Chethodil, J. M., Srivastava, A. P., Praseetha, P., Pal, H., & Choudhury, S. D. (2019). An insight into the molecular and surface state photoluminescence of carbon dots revealed through solvent-induced modulations in their excitation wavelength dependent emission properties. *Photochemical & Photobiological Sciences*, *18*(1), 110-119.

Ghasemi, M., Balar, N., Peng, Z., Hu, H., Qin, Y., Kim, T., Rech, J. J., Bidwell, M., Mask, W., & McCulloch, I. (2021). A molecular interaction–diffusion framework for predicting organic solar cell stability. *Nature materials*, *20*(4), 525-532.

Gong, X., Zhang, Q., Gao, Y., Shuang, S., Choi, M. M., & Dong, C. (2016). Phosphorus and nitrogen dual-doped hollow carbon dot as a nanocarrier for doxorubicin delivery and biological imaging. *ACS Applied Materials & Interfaces*, *8*(18), 11288-11297.

Guo, X., Fan, Q., Wu, J., Li, G., Peng, Z., Su, W., Lin, J., Hou, L., Qin, Y., & Ade, H. (2021). Optimized active layer morphologies via ternary copolymerization of polymer donors for 17.6% efficiency organic solar cells with enhanced fill factor. *Angewandte Chemie International Edition*, *60*(5), 2322-2329.

Gurney, R. S., Li, W., Yan, Y., Liu, D., Pearson, A. J., & Wang, T. (2019). Morphology and efficiency enhancements of PTB7-Th: ITIC nonfullerene organic solar cells processed via solvent vapor annealing. *Journal of Energy Chemistry*, *37*, 148-156.

Hassan, M. M., Khan, W., Azam, A., & Naqvi, A. (2014). Effect of size reduction on structural and optical properties of ZnO matrix due to successive doping of Fe ions. *Journal of Luminescence*, *145*, 160-166.

Ho, C. H. Y., Kim, T., Xiong, Y., Firdaus, Y., Yi, X., Dong, Q., Rech, J. J., Gadisa, A., Booth, R., & O'Connor, B. T. (2020). High-Performance Tandem Organic Solar Cells Using HSolar as the Interconnecting Layer. *Advanced Energy Materials*, *10*(25), 2000823.

Hola, K., Sudolska, M., Kalytchuk, S., Nachtigallova, D., Rogach, A. L., Otyepka, M., & Zboril, R. (2017). Graphitic nitrogen triggers red fluorescence in carbon dots. *ACS nano*, *11*(12), 12402-12410.

Hou, J., Inganäs, O., Friend, R. H., & Gao, F. (2018). Organic solar cells based on non-fullerene acceptors. *Nature materials*, *17*(2), 119-128.

Hsieh, Y.-T., Chen, J.-Y., Shih, C.-C., Chueh, C.-C., & Chen, W.-C. (2018). Mechanically robust, stretchable organic solar cells via buckle-on-elastomer strategy. *Organic Electronics*, *53*, 339-345.

Hu, Z., Wang, J., Ma, X., Gao, J., Xu, C., Yang, K., Wang, Z., Zhang, J., & Zhang, F. (2020). A critical review on semitransparent organic solar cells. *Nano Energy*, 105376.

Huang, P., Xu, S., Zhang, M., Zhong, W., Xiao, Z., & Luo, Y. (2019). Modulation doping of absorbent cotton derived carbon dots for quantum dot-sensitized solar cells. *Physical chemistry chemical physics*, *21*(47), 26133-26145.

Huang, S., Yang, E., Liu, Y., Yao, J., Su, W., & Xiao, Q. (2018). Low-temperature rapid synthesis of nitrogen and phosphorus dual-doped carbon dots for multicolor cellular imaging and hemoglobin probing in human blood. *Sensors and Actuators B: Chemical*, *265*, 326-334.

Joseph, J., & Anappara, A. A. (2017). White-light-emitting carbon dots prepared by the electrochemical exfoliation of graphite. *ChemPhysChem*, *18*(3), 292-298.

Juang, T. Y., Kao, J. C., Wang, J. C., Hsu, S. Y., & Chen, C. P. (2018). Carbonized Bamboo-Derived Carbon Nanodots as Efficient Cathode Interfacial Layers in High-Performance Organic Photovoltaics. *Advanced Materials Interfaces*, *5*(10), 1800031.

Kadam, K. D., Kim, H., Rehman, S., Patil, H., Aziz, J., Dongale, T. D., Khan, M. F., & Kim, D.-k. (2021). Optimization of ZnO: PEIE as an Electron Transport Layer for Flexible Organic Solar Cells. *Energy & Fuels*, *35*(15), 12416-12424.

Kim, S., Kim, C.-H., Lee, S. K., Jeong, J.-H., Lee, J., Jin, S.-H., Shin, W. S., Song, C. E., Choi, J.-H., & Jeong, J.-R. (2013). Highly efficient uniform ZnO nanostructures for an electron transport layer of inverted organic solar cells. *Chemical Communications*, *49*(54), 6033-6035.

Kurukavak, Ç. K., Yılmaz, T., Çetin, Ş., Alqadasi, M. M., Al-Khawlany, K. M., & Kuş, M. (2021). Synthesis of boron-doped CQDs and its use as an additive in P3HT: PCBM layer for efficiency improvement of organic solar cell. *Microelectronic Engineering*, *235*, 111465.

Kwon, W., Do, S., Kim, J.-H., Seok Jeong, M., & Rhee, S.-W. (2015). Control of photoluminescence of carbon nanodots via surface functionalization using para-substituted anilines. *Scientific reports*, *5*(1), 1-10.

Lattante, S. (2014). Electron and hole transport layers: their use in inverted bulk heterojunction polymer solar cells. *Electronics*, *3*(1), 132-164.

Lee, S. J., Kim, S., Lim, D. C., Kim, D. H., Nahm, S., & Han, S. H. (2019). Inverted bulk-heterojunction polymer solar cells using a sputter-deposited Al-doped ZnO electron transport layer. *Journal of Alloys and Compounds*, *777*, 717-722.

Li, N., McCulloch, I., & Brabec, C. J. (2018). Analyzing the efficiency, stability and cost potential for fullerene-free organic photovoltaics in one figure of merit. *Energy & Environmental Science*, *11*(6), 1355-1361.

Li, S., Liu, W., Li, C. Z., Shi, M., & Chen, H. (2017). Efficient organic solar cells with non-fullerene acceptors. *Small*, *13*(37), 1701120.

Li, X., Pan, F., Sun, C., Zhang, M., Wang, Z., Du, J., Wang, J., Xiao, M., Xue, L., & Zhang, Z.-G. (2019). Simplified synthetic routes for low cost and high photovoltaic performance n-type organic semiconductor acceptors. *Nature communications*, *10*(1), 1-11.

Li, X., Zhang, S., Kulinich, S. A., Liu, Y., & Zeng, H. (2014). Engineering surface states of carbon dots to achieve controllable luminescence for solid-luminescent composites and sensitive Be2+ detection. *Scientific reports*, *4*(1), 1-8.

Lim, F. J., Krishnamoorthy, A., & Ho, G. W. (2016). All-in-one solar cell: stable, light-soaking free, solution processed and efficient diketopyrrolopyrrole based small molecule inverted organic solar cells. *Solar Energy Materials and Solar Cells*, *150*, 19-31.

Lin, L., & Zhang, S. (2012). Creating high yield water soluble luminescent graphene quantum dots via exfoliating and disintegrating carbon nanotubes and graphite flakes. *Chemical Communications*, *48*(82), 10177-10179.

Lin, X., Yang, Y., Nian, L., Su, H., Ou, J., Yuan, Z., Xie, F., Hong, W., Yu, D., & Zhang, M. (2016). Interfacial modification layers based on carbon dots for efficient inverted polymer solar cells exceeding 10% power conversion efficiency. *Nano Energy*, *26*, 216-223.

Lin, Y., Wang, J., Zhang, Z. G., Bai, H., Li, Y., Zhu, D., & Zhan, X. (2015). An electron acceptor challenging fullerenes for efficient polymer solar cells. *ADVANCED MATERIALS*, *27*(7), 1170-1174.

Ling, Z., Zhao, Y., Wang, S., Pan, S., Lian, H., Peng, C., Yang, X., Liao, Y., Lan, W., & Wei, B. (2019). High-performance light-soaking-free polymer solar cells based on a LiF modified ZnO electron extraction layer. *Journal of Materials Chemistry C*, *7*(30), 9354-9361.

Liu, C., Zhang, L., Xiao, L., Peng, X., & Cao, Y. (2016). Doping ZnO with water/alcohol-soluble small molecules as electron transport layers for inverted polymer solar cells. *ACS Applied Materials & Interfaces*, *8*(41), 28225-28230.

Liu, G., Jia, J., Zhang, K., Jia, X. e., Yin, Q., Zhong, W., Li, L., Huang, F., & Cao, Y. (2019). 15% efficiency tandem organic solar cell based on a novel highly efficient wide-bandgap nonfullerene acceptor with low energy loss. *Advanced Energy Materials*, *9*(11), 1803657.

Lu, L., Xu, T., Chen, W., Lee, J. M., Luo, Z., Jung, I. H., Park, H. I., Kim, S. O., & Yu, L. (2013). The role of N-doped multiwall carbon nanotubes in achieving highly efficient polymer bulk heterojunction solar cells. *Nano letters*, *13*(6), 2365-2369.

Ma, R., Liu, T., Luo, Z., Guo, Q., Xiao, Y., Chen, Y., Li, X., Luo, S., Lu, X., & Zhang, M. (2020). Improving open-circuit voltage by a chlorinated polymer donor endows binary organic solar cells efficiencies over 17%. *Sci. China: Chem*, *63*(3), 325-330.

Mandal, B., Sarkar, S., & Sarkar, P. (2012). Exploring the electronic structure of graphene quantum dots. *Journal of Nanoparticle Research*, *14*(12), 1-8.

Manju, S., & Sagar, N. (2017). Renewable energy integrated desalination: A sustainable solution to overcome future fresh-water scarcity in India. *Renewable and Sustainable Energy Reviews*, *73*, 594-609.

Miao, S., Liang, K., Zhu, J., Yang, B., Zhao, D., & Kong, B. (2020). Hetero-atom-doped carbon dots: Doping strategies, properties and applications. *Nano Today*, *33*, 100879.

Mintz, K. J., Zhou, Y., & Leblanc, R. M. (2019). Recent development of carbon quantum dots regarding their optical properties, photoluminescence mechanism, and core structure. *Nanoscale*, *11*(11), 4634-4652.

Mola, G. T., Oseni, S. O., Kaviyarasu, K., & Maaza, M. (2017). Co-solvent additives influence on the performance of PTB7: PCBM based Thin film organic solar cell. *Materials Today: Proceedings*, *4*(14), 12558-12564.

Molkenova, A., & Atabaev, T. S. (2019). Phosphorus-doped carbon dots (P-CDs) from dextrose for low-concentration ferric ions sensing in water. *Optik*, *187*, 70-73.

Nair, S. S., & Kumar, D. (2016). Morphology control in the bulk heterojunction blend of inverted organic solar cell via co-solvent addition. *ADVANCED MATERIALS*, *7*(10), 806-812.

Naz, H., Ali, R. N., Liu, Q., Yang, S., & Xiang, B. (2018). Niobium doped zinc oxide nanorods as an electron transport layer for high-performance inverted polymer solar cells. *Journal of Colloid and Interface Science*, *512*, 548-554.

Nie, H., Li, M., Li, Q., Liang, S., Tan, Y., Sheng, L., Shi, W., & Zhang, S. X.-A. (2014). Carbon dots with continuously tunable full-color emission and their application in ratiometric pH sensing. *Chemistry of Materials*, *26*(10), 3104-3112.

Oseni, S. O., & Mola, G. T. (2017). The effect of uni-and binary solvent additives in PTB7: PC61BM based solar cells. *Solar Energy*, *150*, 66-72.

Pali, L. S., Gupta, S. K., & Garg, A. (2018). Organic solar cells on Al electroded opaque substrates: Assessing the need of ZnO as electron transport layer. *Solar Energy*, *160*, 396-403.

Papaioannou, N., Titirici, M.-M., & Sapelkin, A. (2019). Investigating the effect of reaction time on carbon dot formation, structure, and optical properties. *ACS omega*, *4*(26), 21658-21665.

Park, S., Lee, H., Park, S. W., Kim, T. E., Park, S. H., Jung, Y. K., & Cho, S. (2021). Improved exciton dissociation efficiency by a carbon-quantum-dot doped workfunction modifying layer in polymer solar cells. *Current Applied Physics*, *21*, 140-146.

Park, S. Y., Lee, C. Y., An, H.-R., Kim, H., Lee, Y.-C., Park, E. C., Chun, H.-S., Yang, H. Y., Choi, S.-H., & Kim, H. S. (2017). Advanced carbon dots via plasma-induced surface functionalization for fluorescent and bio-medical applications. *Nanoscale*, *9*(26), 9210-9217.

Peng, H., Li, Y., Jiang, C., Luo, C., Qi, R., Huang, R., Duan, C.-G., & Travas-Sejdic, J. (2016). Tuning the properties of luminescent nitrogen-doped carbon dots by reaction precursors. *Carbon*, *100*, 386-394.

Qin, F., Wang, W., Sun, L., Jiang, X., Hu, L., Xiong, S., Liu, T., Dong, X., Li, J., & Jiang, Y. (2020). Robust metal ion-chelated polymer interfacial layer for ultraflexible non-fullerene organic solar cells. *Nature communications*, *11*(1), 1-8.

Qiu, B., Chen, S., Li, H., Luo, Z., Yao, J., Sun, C., Li, X., Xue, L., Zhang, Z.-G., & Yang, C. (2019). A simple approach to prepare chlorinated polymer donors with low-lying HOMO level for high performance polymer solar cells. *Chemistry of Materials*, *31*(17), 6558-6567.

Qiu, B., Chen, Z., Qin, S., Yao, J., Huang, W., Meng, L., Zhu, H., Yang, Y., Zhang, Z. G., & Li, Y. (2020). Highly Efficient All-Small-Molecule Organic Solar Cells with Appropriate Active Layer Morphology by Side Chain Engineering of Donor Molecules and Thermal Annealing. *ADVANCED MATERIALS*, *32*(21), 1908373.

Rafique, S., Abdullah, S. M., Mahmoud, W. E., Al-Ghamdi, A. A., & Sulaiman, K. (2016). Stability enhancement in organic solar cells by incorporating V 2 O 5 nanoparticles in the hole transport layer. *RSC advances*, *6*(55), 50043-50052.

Rafique, S., Abdullah, S. M., Sulaiman, K., & Iwamoto, M. (2018). Fundamentals of bulk heterojunction organic solar cells: An overview of stability/degradation issues and strategies for improvement. *Renewable and Sustainable Energy Reviews*, *84*, 43-53.

Rao, A. D., Murali, M., Kesavan, A. V., & Ramamurthy, P. C. (2018). Experimental investigation of charge transfer, charge extraction, and charge carrier concentration in P3HT: PBD-DT-DPP: PC70BM ternary blend photovoltaics. *Solar Energy*, *174*, 1078-1084.

Ren, J., Weber, F., Weigert, F., Wang, Y., Choudhury, S., Xiao, J., Lauermann, I., Resch-Genger, U., Bande, A., & Petit, T. (2019). Influence of surface chemistry on optical, chemical and electronic properties of blue luminescent carbon dots. *Nanoscale*, *11*(4), 2056-2064.

Riaz, R., Ali, M., Maiyalagan, T., Anjum, A. S., Lee, S., Ko, M. J., & Jeong, S. H. (2019). Dye-sensitized solar cell (DSSC) coated with energy down shift layer of nitrogen-doped carbon quantum dots (N-CQDs) for enhanced current density and stability. *Applied Surface Science*, *483*, 425-431.

Sánchez, J., Balderrama, V., Estrada, M., Osorio, E., Ferré-Borrull, J., Marsal, L., & Pallarès, J. (2017). Stability study of high efficiency polymer solar cells using TiOx as electron transport layer. *Solar Energy*, *150*, 147-155.

Sarkar, S., Sudolska, M., Dubecky, M., Reckmeier, C. J., Rogach, A. L., Zboril, R., & Otyepka, M. (2016). Graphitic nitrogen doping in carbon dots causes red-shifted absorption. *The Journal of Physical Chemistry C*, *120*(2), 1303-1308.

Shao, X., Gu, H., Wang, Z., Chai, X., Tian, Y., & Shi, G. (2013). Highly selective electrochemical strategy for monitoring of cerebral Cu2+ based on a carbon dot-TPEA hybridized surface. *Analytical chemistry*, *85*(1), 418-425.

Sharma, A., Chauhan, M., Bharti, V., Kumar, M., Chand, S., Tripathi, B., & Tiwari, J. (2017). Revealing the correlation between charge carrier recombination and extraction in an organic solar cell under varying illumination intensity. *Physical chemistry chemical physics*, *19*(38), 26169-26178.

Sharma, R., Lee, H., Borse, K., Gupta, V., Joshi, A. G., Yoo, S., & Gupta, D. (2017). Ga-doped ZnO as an electron transport layer for PffBT4T-2OD: PC70BM organic solar cells. *Organic Electronics*, *43*, 207-213.

Shi, B., Su, Y., Zhang, L., Huang, M., Liu, R., & Zhao, S. (2016). Nitrogen and phosphorus co-doped carbon nanodots as a novel fluorescent probe for highly sensitive detection of Fe3+ in human serum and living cells. *ACS Applied Materials & Interfaces*, *8*(17), 10717-10725.

Shi, W., Han, Q., Wu, J., Ji, C., Zhou, Y., Li, S., Gao, L., Leblanc, R. M., & Peng, Z. (2022). Synthesis Mechanisms, Structural Models, and Photothermal Therapy Applications of Top-Down Carbon Dots from Carbon Powder, Graphite, Graphene, and Carbon Nanotubes. *International Journal of Molecular Sciences*, *23*(3), 1456.

Siddiki, M. K., Li, J., Galipeau, D., & Qiao, Q. (2010). A review of polymer multijunction solar cells. *Energy & Environmental Science*, *3*(7), 867-883.

Singh, A., Gupta, S. K., & Garg, A. (2017). Inkjet printing of NiO films and integration as hole transporting layers in polymer solar cells. *Scientific reports*, *7*(1), 1-12.

Singh, V. K., Singh, V., Yadav, P. K., Chandra, S., Bano, D., Kumar, V., Koch, B., Talat, M., & Hasan, S. H. (2018). Bright-blue-emission nitrogen and phosphorus-doped carbon quantum dots as a promising nanoprobe for detection of Cr (VI) and ascorbic acid in pure aqueous solution and in living cells. *New Journal of Chemistry*, *42*(15), 12990-12997.

Song, S., Lee, K. T., Koh, C. W., Shin, H., Gao, M., Woo, H. Y., Vak, D., & Kim, J. Y. (2018). Hot slot die coating for additive-free fabrication of high performance roll-to-roll processed polymer solar cells. *Energy & Environmental Science*, *11*(11), 3248-3255.

Song, W., Yu, K., Zhou, E., Xie, L., Hong, L., Ge, J., Zhang, J., Zhang, X., Peng, R., & Ge, Z. (2021). Crumple Durable Ultraflexible Organic Solar Cells with an Excellent Power-per-Weight Performance. *Advanced Functional Materials*, 2102694.

Song, Y., Zhu, S., Zhang, S., Fu, Y., Wang, L., Zhao, X., & Yang, B. (2015). Investigation from chemical structure to photoluminescent mechanism: a type of carbon dots from the pyrolysis of citric acid and an amine. *Journal of Materials Chemistry C*, *3*(23), 5976-5984.

Sudolska, M., Dubecky, M., Sarkar, S., Reckmeier, C. J., Zboril, R., Rogach, A. L., & Otyepka, M. (2015). Nature of absorption bands in oxygen-functionalized graphitic carbon dots. *The Journal of Physical Chemistry C*, *119*(23), 13369-13373.

Sun, C., Pan, F., Bin, H., Zhang, J., Xue, L., Qiu, B., Wei, Z., Zhang, Z.-G., & Li, Y. (2018). A low cost and high performance polymer donor material for polymer solar cells. *Nature communications*, *9*(1), 1-10.

Sun, Y., Lu, S., Xu, R., Liu, K., Zhou, Z., Yue, S., Azam, M., Ren, K., Wei, Z., & Wang, Z. (2019). Collection optimization of photo-generated charge carriers for efficient organic solar cells. *Journal of Power Sources*, *412*, 465-471.

Tang, J., Zhang, J., Zhang, Y., Xiao, Y., Shi, Y., Chen, Y., Ding, L., & Xu, W. (2019). Influence of group modification at the edges of carbon quantum dots on fluorescent emission. *Nanoscale Research Letters*, *14*(1), 1-10.

Tang, Y., Rao, L., Li, Z., Lu, H., Yan, C., Yu, S., Ding, X., & Yu, B. (2018). Rapid synthesis of highly photoluminescent nitrogen-doped carbon quantum dots via a microreactor with foamy copper for the detection of Hg2+ ions. *Sensors and Actuators B: Chemical*, *258*, 637-647.

Tran, V.-H., Eom, S. H., Yoon, S. C., Kim, S.-K., & Lee, S.-H. (2019). Enhancing device performance of inverted organic solar cells with SnO2/Cs2CO3 as dual electron transport layers. *Organic Electronics*, *68*, 85-95.

Traverse, C. J., Pandey, R., Barr, M. C., & Lunt, R. R. (2017). Emergence of highly transparent photovoltaics for distributed applications. *Nature Energy*, *2*(11), 849-860.

Walker, B., Choi, H., & Kim, J. Y. (2017). Interfacial engineering for highly efficient organic solar cells. *Current Applied Physics*, *17*(3), 370-391.

Wan, Q., Guo, X., Wang, Z., Li, W., Guo, B., Ma, W., Zhang, M., & Li, Y. (2016). 10.8% efficiency polymer solar cells based on PTB7-Th and PC71BM via binary solvent additives treatment. *Advanced Functional Materials*, *26*(36), 6635-6640.

Wang, J., Li, H., Lei, Q., Chang, F., Fan, W., Zhang, H., & Cai, L. (2019). Dual-interface modification effect of Carbon Quantum Dots on the performance of Polymer Solar Cells. *Journal of Materials Science: Materials in Electronics*, *30*(12), 11063-11069.

Wang, K., Zhang, Z., Liu, C., Fu, Q., Xu, W., Huang, C., Weiss, R., & Gong, X. (2017). Efficient polymer solar cells by lithium sulfonated polystyrene as a charge transport interfacial layer. *ACS Applied Materials & Interfaces*, *9*(6), 5348-5357.

Wang, M., Sun, Y., Guo, J., Li, Z., Liu, C., & Guo, W. (2019). Alkali metal salts doped ZnO interfacial layers facilitate charge transport for organic solar cells. *Organic Electronics*, *74*, 258-264.

Wang, Y., Chang, X., Jing, N., & Zhang, Y. (2018). Hydrothermal synthesis of carbon quantum dots as fluorescent probes for the sensitive and rapid detection of picric acid. *Analytical Methods*, *10*(23), 2775-2784.

Wang, Y., Kalytchuk, S., Zhang, Y., Shi, H., Kershaw, S. V., & Rogach, A. L. (2014). Thickness-dependent full-color emission tunability in a flexible carbon dot ionogel. *The journal of physical chemistry letters*, *5*(8), 1412-1420.

Wang, Y., Lan, W., Li, N., Lan, Z., Li, Z., Jia, J., & Zhu, F. (2019). Stability of Nonfullerene Organic Solar Cells: From Built-in Potential and Interfacial Passivation Perspectives. *Advanced Energy Materials*, *9*(19), 1900157.

Wang, Y., Li, Y., Yan, Y., Xu, J., Guan, B., Wang, Q., Li, J., & Yu, J. (2013). Luminescent carbon dots in a new magnesium aluminophosphate zeolite. *Chemical Communications*, *49*(79), 9006-9008.

Wang, Y., Wu, B., Wu, Z., Lan, Z., Li, Y., Zhang, M., & Zhu, F. (2017). Origin of efficient inverted nonfullerene organic solar cells: enhancement of charge extraction and suppression of bimolecular recombination enabled by augmented internal electric field. *The journal of physical chemistry letters*, *8*(21), 5264-5271.

Wang, Y., Yan, L., Ji, G., Wang, C., Gu, H., Luo, Q., Chen, Q., Chen, L., Yang, Y., & Ma, C.-Q. (2018). Synthesis of N, S-doped carbon quantum dots for use in organic solar cells as the ZnO modifier to eliminate the light-soaking effect. *ACS Applied Materials & Interfaces*, *11*(2), 2243-2253.

Wang, Y., Zhu, Y., Yu, S., & Jiang, C. (2017). Fluorescent carbon dots: rational synthesis, tunable optical properties and analytical applications. *RSC advances*, *7*(65), 40973-40989.

Woo, S., Hyun Kim, W., Kim, H., Yi, Y., Lyu, H. K., & Kim, Y. (2014). 8.9% single-stack inverted polymer solar cells with electron-rich polymer nanolayer-modified inorganic electron-collecting buffer layers. *Advanced Energy Materials*, *4*(7), 1301692.

Wu, B., Wu, Z., Yang, Q., Zhu, F., Ng, T.-W., Lee, C.-S., Cheung, S.-H., & So, S.-K. (2016). Improvement of charge collection and performance reproducibility in inverted organic solar cells by suppression of ZnO subgap states. *ACS Applied Materials & Interfaces*, *8*(23), 14717-14724.

Wu, P., Li, W., Wu, Q., Liu, Y., & Liu, S. (2017). Hydrothermal synthesis of nitrogen-doped carbon quantum dots from microcrystalline cellulose for the detection of Fe 3+ ions in an acidic environment. *RSC advances*, *7*(70), 44144-44153.

Wu, Z. L., Liu, Z. X., & Yuan, Y. H. (2017). Carbon dots: materials, synthesis, properties and approaches to long-wavelength and multicolor emission. *Journal of Materials Chemistry B*, *5*(21), 3794-3809.

Xia, T., Cai, Y., Fu, H., & Sun, Y. (2019). Optimal bulk-heterojunction morphology enabled by fibril network strategy for high-performance organic solar cells. *Science China Chemistry*, *62*(6), 662-668.

Xie, Y., Li, T., Guo, J., Bi, P., Xue, X., Ryu, H. S., Cai, Y., Min, J., Huo, L., & Hao, X. (2019). Ternary organic solar cells with small nonradiative recombination loss. *ACS Energy Letters*, *4*(5), 1196-1203.

Xu, M.-F., Liao, Y.-J., Zu, F.-S., Liang, J., Yuan, D.-X., Wang, Z.-K., & Liao, L.-S. (2014). Work-function tuneable and aqueous solution-processed Cs 2 CO 3 for high-performance polymer solar cells. *Journal of Materials Chemistry A*, *2*(24), 9400-9404.

Xu, Q., Kuang, T., Liu, Y., Cai, L., Peng, X., Sreeprasad, T. S., Zhao, P., Yu, Z., & Li, N. (2016). Heteroatom-doped carbon dots: synthesis, characterization, properties, photoluminescence mechanism and biological applications. *Journal of Materials Chemistry B*, *4*(45), 7204-7219.

Xu, Q., Li, B., Ye, Y., Cai, W., Li, W., Yang, C., Chen, Y., Xu, M., Li, N., & Zheng, X. (2018). Synthesis, mechanical investigation, and application of nitrogen and phosphorus co-doped carbon dots with a high photoluminescent quantum yield. *Nano Research*, *11*(7), 3691-3701.

Xu, W.-L., Wu, B., Zheng, F., Wang, H.-B., Wang, Y.-Z., Bian, F.-G., Hao, X.-T., & Zhu, F. (2015). Homogeneous phase separation in polymer: fullerene bulk heterojunction organic solar cells. *Organic Electronics*, *25*, 266-274.

Xu, X., Li, Y., & Peng, Q. (2020). Recent Advances Toward Highly Efficient Tandem Organic Solar Cells. *Small Structures*, *1*(1), 2000016.

Xu, X., Xiao, J., Zhang, G., Wei, L., Jiao, X., Yip, H.-L., & Cao, Y. (2020). Interface-enhanced organic solar cells with extrapolated T80 lifetimes of over 20 years. *Science Bulletin*, *65*(3), 208-216.

Yan, C., Barlow, S., Wang, Z., Yan, H., Jen, A. K.-Y., Marder, S. R., & Zhan, X. (2018). Non-fullerene acceptors for organic solar cells. *Nature Reviews Materials*, *3*(3), 1-19.

Yan, Y., Chen, J., Li, N., Tian, J., Li, K., Jiang, J., Liu, J., Tian, Q., & Chen, P. (2018). Systematic bandgap engineering of graphene quantum dots and applications for photocatalytic water splitting and CO2 reduction. *ACS nano*, *12*(4), 3523-3532.

Yang, H., Liu, Y., Guo, Z., Lei, B., Zhuang, J., Zhang, X., Liu, Z., & Hu, C. (2019). Hydrophobic carbon dots with blue dispersed emission and red aggregation-induced emission. *Nature communications*, *10*(1), 1-11.

Yang, L., Wang, J., Lu, X., Lin, H., Du, X., Chen, Z., & Tao, S. (2021). Morphology optimization of organic solar cells enabled by interface engineering of zinc oxide layer with a conjugated organic material. *Organic Electronics*, *91*, 106065.

Yang, Y., Cui, J., Zheng, M., Hu, C., Tan, S., Xiao, Y., Yang, Q., & Liu, Y. (2012). One-step synthesis of amino-functionalized fluorescent carbon nanoparticles by hydrothermal carbonization of chitosan. *Chemical Communications*, *48*(3), 380-382.

Yang, Y., Lin, X., Li, W., Ou, J., Yuan, Z., Xie, F., Hong, W., Yu, D., Ma, Y., & Chi, Z. (2017). One-pot large-scale synthesis of carbon quantum dots: efficient cathode interlayers for polymer solar cells. *ACS Applied Materials & Interfaces*, *9*(17), 14953-14959.

Yang, Z., Xu, M., Liu, Y., He, F., Gao, F., Su, Y., Wei, H., & Zhang, Y. (2014). Nitrogen-doped, carbon-rich, highly photoluminescent carbon dots from ammonium citrate. *Nanoscale*, *6*(3), 1890-1895.

Yeboah, D., & Singh, J. (2017). Dependence of exciton diffusion length and diffusion coefficient on photophysical parameters in bulk heterojunction organic solar cells. *Journal of Electronic Materials*, *46*(11), 6451-6460.

Yin, Z., Wei, J., Chen, S.-C., Cai, D., Ma, Y., Wang, M., & Zheng, Q. (2017). Long lifetime stable and efficient semitransparent organic solar cells using a ZnMgO-modified cathode combined with a thin MoO 3/Ag anode. *Journal of Materials Chemistry A*, *5*(8), 3888-3899.

Yu, G., Gao, J., Hummelen, J. C., Wudl, F., & Heeger, A. J. (1995). Polymer photovoltaic cells: enhanced efficiencies via a network of internal donor-acceptor heterojunctions. *Science*, *270*(5243), 1789-1791.

Yuan, J., Zhang, Y., Zhou, L., Zhang, G., Yip, H.-L., Lau, T.-K., Lu, X., Zhu, C., Peng, H., & Johnson, P. A. (2019). Single-junction organic solar cell with over 15% efficiency using fused-ring acceptor with electron-deficient core. *Joule*, *3*(4), 1140-1151.

Zafar, M., Kim, B., & Kim, D.-H. (2020). Improvement in performance of inverted organic solar cell by rare earth element lanthanum doped ZnO electron buffer layer. *Materials Chemistry and Physics*, *240*, 122076.

Zakiya, A.-B., Pearson, C., Groves, C., & Petty, M. C. (2017). Enhanced lifetime of organic photovoltaic diodes utilizing a ternary blend including an insulating polymer. *Solar Energy Materials and Solar Cells*, *160*, 101-106.

Zhan, T., Ren, P., Huang, X., Zhang, X., Chen, G., Xiong, J., Xue, X., Cai, P., Zhang, J., & Chen, J. (2021). A solution-processed, ultraviolet-irradiation-derived WO3 film as anode interface layer for high-performance non-fullerene organic solar cells. *Solar Energy*, *216*, 211-216.

Zhang, G., Zhao, J., Chow, P. C., Jiang, K., Zhang, J., Zhu, Z., Zhang, J., Huang, F., & Yan, H. (2018). Nonfullerene acceptor molecules for bulk heterojunction organic solar cells. *Chemical reviews*, *118*(7), 3447-3507.

Zhang, R., Zhao, M., Wang, Z., Wang, Z., Zhao, B., Miao, Y., Zhou, Y., Wang, H., Hao, Y., & Chen, G. (2018). Solution-processable ZnO/carbon quantum dots electron extraction layer for highly efficient polymer solar cells. *ACS Applied Materials & Interfaces*, *10*(5), 4895-4903.

Zhang, S., Zhang, L., Huang, L., Zheng, G., Zhang, P., Jin, Y., Jiao, Z., & Sun, X. (2019). Study on the fluorescence properties of carbon dots prepared via combustion process. *Journal of Luminescence*, *206*, 608-612.

Zhang, X., Liu, C., Li, Z., Guo, J., Shen, L., Guo, W., Zhang, L., Ruan, S., & Long, Y. (2017). An easily prepared carbon quantum dots and employment for inverted organic photovoltaic devices. *Chemical Engineering Journal*, *315*, 621-629.

Zhang, Y., Sajjad, M. T., Blaszczyk, O., Ruseckas, A., Serrano, L. A., Cooke, G., & Samuel, I. D. (2019). Enhanced exciton harvesting in a planar heterojunction organic photovoltaic device by solvent vapor annealing. *Organic Electronics*, *70*, 162-166.

Zhang, Y., Wang, Y., Feng, X., Zhang, F., Yang, Y., & Liu, X. (2016). Effect of reaction temperature on structure and fluorescence properties of nitrogen-doped carbon dots. *Applied Surface Science*, *387*, 1236-1246.

Zhao, S., Lan, M., Zhu, X., Xue, H., Ng, T.-W., Meng, X., Lee, C.-S., Wang, P., & Zhang, W. (2015). Green synthesis of bifunctional fluorescent carbon dots from garlic for cellular imaging and free radical scavenging. *ACS Applied Materials & Interfaces*, *7*(31), 17054-17060.

Zheng, J., Xie, Y., Wei, Y., Yang, Y., Liu, X., Chen, Y., & Xu, B. (2020). An efficient synthesis and photoelectric properties of green carbon quantum dots with high fluorescent quantum yield. *Nanomaterials*, *10*(1), 82.

Zheng, K., Guan, L., Ma, H., Zhao, S., Zhao, J., Wang, Z., Dong, G., Wei, Z., & Li, X. (2018). Excitation-dependent carbon dots powders based on dehydration condensation by microwave–hydrothermal method. *Journal of Materials Science*, *53*(23), 15907-15914.

Zheng, Z., Zhang, S., Wang, J., Zhang, J., Zhang, D., Zhang, Y., Wei, Z., Tang, Z., Hou, J., & Zhou, H. (2019). Exquisite modulation of ZnO nanoparticle electron transporting layer for high-performance fullerene-free organic solar cell with inverted structure. *Journal of Materials Chemistry A*, *7*(8), 3570-3576.

Zhou, Y., Benetti, D., Tong, X., Jin, L., Wang, Z. M., Ma, D., Zhao, H., & Rosei, F. (2018). Colloidal carbon dots based highly stable luminescent solar concentrators. *Nano Energy*, *44*, 378-387.

Zhu, C., Yuan, J., Cai, F., Meng, L., Zhang, H., Chen, H., Li, J., Qiu, B., Peng, H., & Chen, S. (2020). Tuning the electron-deficient core of a non-fullerene acceptor to achieve over 17% efficiency in a single-junction organic solar cell. *Energy & Environmental Science*, *13*(8), 2459-2466.

Zhu, S., Song, Y., Zhao, X., Shao, J., Zhang, J., & Yang, B. (2015). The photoluminescence mechanism in carbon dots (graphene quantum dots, carbon nanodots, and polymer dots): current state and future perspective. *Nano Research*, *8*(2), 355-381.

Zidan, M. N., Everitt, N., Ismail, T., & Fahim, I. S. (2021). Organic Solar Cells Parameters Extraction and Characterization Techniques. *Polymers*, *13*(19), 3224.

Appendix A

XRD Results for Precursor Variations

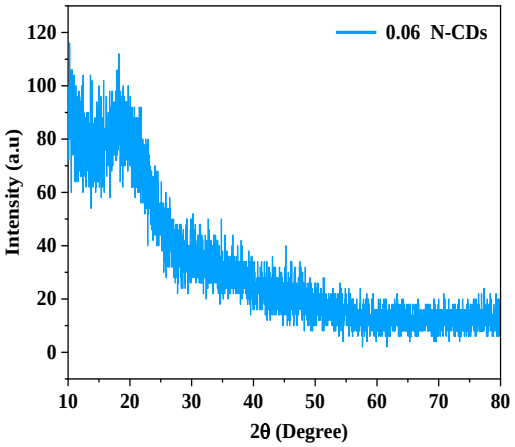

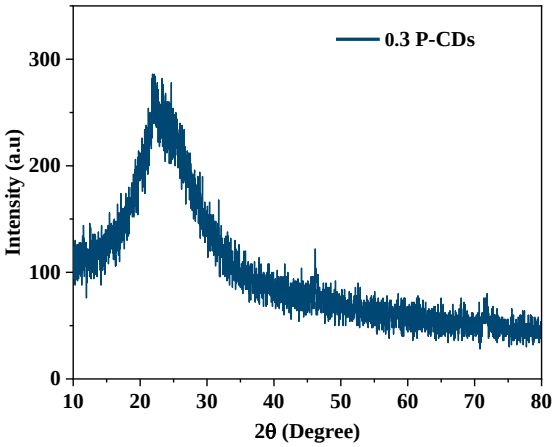

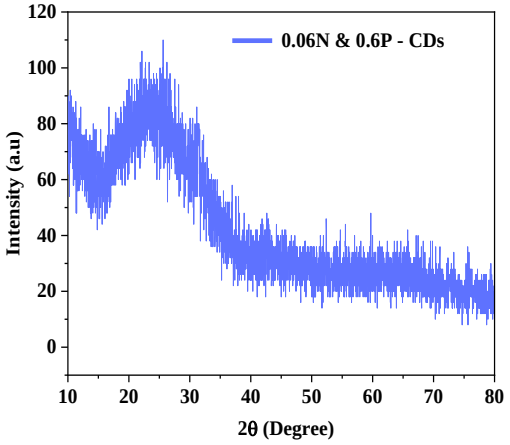

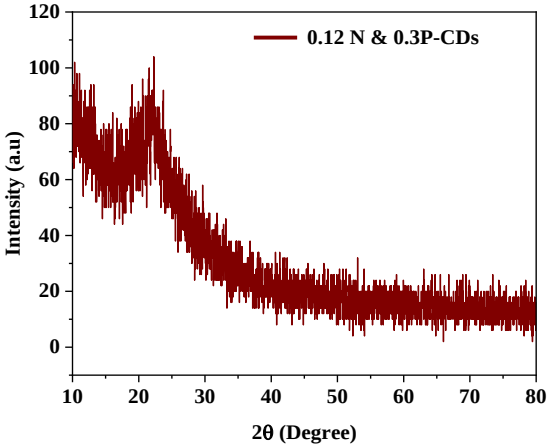

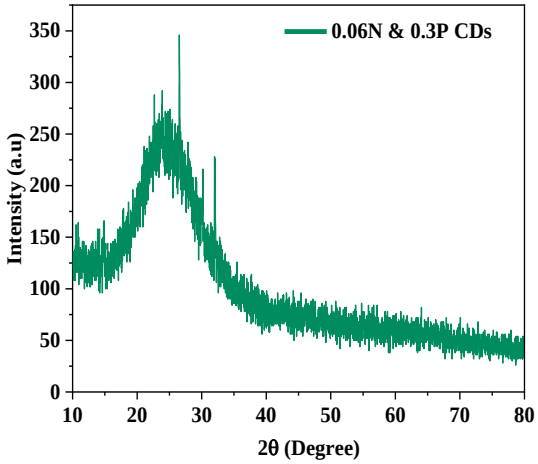

Appendix B

UV-Vis Absorption Results for Precursor Variations